University of Alberta

Internal Wave Generation by Intrusions, Topography, and Turbulence

by

James Ross Munroe

A thesis submitted to the Faculty of Graduate Studies and Research in partial fulfillment of the requirements for the degree of

Doctor of Philosophy

Department of Physics

Fall 2009
Edmonton, Alberta

Examining Committee

Bruce Sutherland, Physics and Earth & Atmospheric Sciences

Moritz Heimpel, Physics

John Wilson, Earth & Atmospheric Sciences

Vadim Kravchinsky, Physics

Paul Myers, Earth & Atmospheric Sciences

Thomas Peacock, Mechanical Engineering, Massachusetts Institute of Technology

Abstract

Internal gravity waves transport energy and momentum in both the atmosphere and the ocean. This physical process occurs at such small length scales that it is not captured by coarse resolution numerical models of weather and climate. A series of experiments is presented that model the generation of non-hydrostatic internal gravity waves by intrusions and by the forcing of wind driven turbulent eddies in the surface mixed layer of the ocean. In a first set of experiments, gravity currents intrude into a uniformly stratified ambient fluid and the internal waves that are launched are examined with a finite-volume, full-depth, lock-release setup. In a second set of experiments, isolated rough topography is towed through stratified fluid and the interaction between the turbulent wake and internal waves is investigated. In a third set of experiments, a turbulent shear layer is forced by a conveyor belt affixed with flat plates near the surface of a stratified fluid and downward propagating internal waves are generated. The turbulence in the shear layer is characterized using particle image velocimetry to measure the kinetic energy as well as length and time scales. The internal waves are measured using synthetic schlieren to determine the amplitudes, frequencies, and the energy of the generated waves. Finally, numerical simulations are used to validate and extend the results of laboratory experiments. The thesis will address the question of what fraction of the turbulent kinetic energy of a shear turbulent mixed layer is radiated away by internal waves. Implications for internal waves propagating into the ocean are discussed.

Acknowledgements

To my wife Amy and daughter Allison, thank you for your support, patience and encouragement. This research was performed under the direction of my supervisor, Dr. Bruce Sutherland, in the Environmental and Industrial Fluid Dynamics Laboratory at the University of Alberta. Thank you Bruce for your mentorship and advice. Thanks also to our laboratory technician, Caspar Williams, both for his technical assistance and for many productive conversations. I appreciate my fellow graduate students Joseph, Josh, Geoff, Heather, Kate, Hayley, Amber and Justine for helpful critiques, suggestions, and support. Thanks is also due to Camille Chalifoux, a WISEST student, for the assistance in the initial implementation the particle image velocimetry system. I want to acknowledge the hard work and skill of Dr. Tom Bewley, Dr. John Taylor, and the other developers of Diablo on which the numerical section of thesis critically depends. Thanks to the staff of both the Department of Mathematical and Statistical Sciences and the Department of Physics for administrative support. To my supervisory committee members Dr. Moritz Heimpel, Dr. John Wilson, and thesis committee members Dr. Paul Myers, Dr. Vadim Kravchinsky, and external examiner Dr. Tom Peacock, thank you for useful feedback and evaluation. Finally, I am grateful for the financial support of National Science and Engineering Council, the Province of Alberta, and the University of Alberta for providing scholarships and funding opportunities that made the research contained in this thesis possible.

Table of Contents

List of Tables

List of Figures

Chapter 1

Introduction

1.1 Motivation

1.1.1 Internal gravity waves

Internal gravity waves are a common phenomenon in density stratified fluids such as the oceans and the atmosphere (Garrett and Munk (1979), Staquet and Sommeria (2002)). An internal gravity wave, or more simply an internal wave, is an oscillation of fluid due to the combined influence of the inertia of the fluid and a restoring buoyancy force. They occur within the body of the fluid either at an interface between two layers with different densities, such as fresh water overlying salt water, or within density gradients, such as the continuous change of density due to salinity or temperature. They are distinguished from surface waves on an air-water interface in that the density differences are relatively small.

The theoretical properties of internal waves are discussed in many fluid dynamics textbooks (e.g. Gill (1982); Kundu (1990)). Internal waves are theoretically interesting in part because the phase velocity, $\vec{c_p}$, is perpendicular to the group velocity, $\vec{c_g}$. That is, the direction that the crests and troughs are observed to move is at right angles to the direction that the energy of the wave propagates. Contrast this with the more everyday experience of surface water waves where the crests move in the same direction as the wave energy. Internal waves are also dispersive, which means the speed of propagation is a function of the wave number vector, $\vec{k} = (k_x, k_z)$. This is different from what is commonly learnt in undergraduate studies of the physics of mechanical waves where the wave speed is a function only of

properties of the undisturbed fluid. Furthermore, if not constrained to an interface, internal waves can propagate vertically as well as horizontally. The dispersion relation for internal waves forces the angle to the vertical, θ, at which these waves propagate to be a function of their frequency, ω. In two dimensions, the dispersion relation is

$$\omega = \frac{Nk_x}{\sqrt{k_x^2 + k_z^2}} = N\cos\theta \tag{1.1}$$

where $N = -\frac{g}{\rho_0}\frac{d\rho}{dz}$ is the buoyancy frequency.

Internal waves are important because they provide a mechanism for transporting energy and momentum in a fluid. Researchers who study internal waves are typically interested in the generation, the propagation and evolution, and the eventual breaking of waves (Thorpe (1975)). Each one of these three aspects is important for understanding and predicting the role internal waves play in distributing energy in a system. Wave generation is concerned with the mechanisms that create the waves, the quantity of energy that is extracted from the background flow or from a localized source and the characteristics such as the frequency and wave number spectrum of waves produced. Propagation problems involve the transport of energy and how the waves evolve depending on changes in the background properties of the fluid and by interacting with other waves. Wave energy is deposited when waves overturn and break leading to localized mixing or acceleration of the background flow. The research presented in this thesis focuses only on wave generation problems.

Internal waves can be generated whenever there is a vertical disturbance of a stratified fluid. For example, consider the phenomena of 'dead-water' where boats enter a body of water and, even with the engines at full power, are unable to maintain their previous speed (Ekman (1904)). This is due to fresh water run-off that floats above the sea water. A boat's propeller disturbs this interface and generates internal waves. Because energy is going into the internal waves, it is not going into accelerating the boat forward. In the atmosphere, internal waves can be launched by the flow of air over mountain ranges which lifts dense air upwards and launches upward propagating internal waves. These waves eventually break depositing momentum and act as a drag force on the atmosphere. In the ocean, currents and tides can push stratified fluid over sills, continental shelves, and sea-mounts to generate

internal waves.

Internal waves can also be generated in the laboratory. The classic experiment is the oscillation of a cylinder that forces fluid up and down (Mowbray and Rarity (1967a)). If the frequency of oscillation is sufficiently low, beams of internal waves are observed to radiate away at an angle related to this frequency. But internal waves can be generated whenever stably stratified fluid is displaced. In this thesis, we examine the generation of internal waves by intrusive gravity currents, by flow over isolated rough topography, and by a turbulent shear layer.

1.1.2 Waves and ocean mixing

One of the tools used in climate change science is the numerical general circulation model (GCM) that simulates the atmosphere and oceans in order to understand how our climate works and create scenarios of future climate. These models are typically set up to simulate averages of the environmental state over time scales of many decades or longer and therefore have relatively coarse resolutions. Even state-of-the-art ocean GCMs have grid length scales on the order of tens of kilometres, which is larger than the wavelengths of non-hydrostatic internal waves generated by turbulent processes. To include these sub-grid scale physical processes into GCMs, they must be parametrized. This means taking the large scale model variables, and, through physical modelling and empirical studies, providing the appropriate adjustment to the large scale model variables which averages the net effect of the various small scale processes.

An important area of current research is understanding the role internal waves play in controlling the meridional overturning circulation (MOC) of the ocean (Wunsch and Ferrari (2004)). The MOC is associated with sinking of dense near-surface waters at high latitudes and upwelling elsewhere (Vallis (2006)). Although not wholly resolved, the downwelling is caused by a combination of surface cooling which leads to convection (Marshall and Schott (1999)) and wind forcing with a circumpolar channel (Vallis (2006)). The physics behind the upwelling is more poorly understood. Upwelling requires the mixing down of heat from the surface into the interior of the ocean. Without this mixing and the associated heat transport,

the deep ocean would eventually fill with dense, stagnant water and there would be no deep circulation.

On average, there needs to be an amount of mixing in the world's oceans characterized by a diffusivity of $\kappa = 10^{-4}$ m^2 s^{-1} (Munk and Wunsch (1998)) based a on one dimensional advective-diffusion balance by matching observed stratification profiles of the ocean and using a global mean vertical upwelling of $w = 10^{-7}$ms^{-1}. Up to recently, GCMs have used a constant diffusivity as a parametrization of the sub-grid scale mixing that must be occurring. However, various studies have found that 10^{-5} m^2 s^{-1} is a fairly typical value in the abyssal ocean. More vigorous mixing has been observed at various hot spots having higher diffusivity associated with tidal flow over topography (Ledwell et al. (2000); Polzin et al. (1997)). This intensified mixing has been linked to internal wave generation and consequent breaking.

Internal waves are thought to provide a transport mechanism for energy and momentum from tidal and wind sources into the abyssal ocean where, after they break, they cause localized mixing (Munk and Wunsch (1998)). In total, an estimated 2.1 TW of energy is required to drive this mixing and thus the Meridional Overturning Circulation. It is thought that both the tides and winds each provide about 1 TW of energy. Over the last decade, there has been substantial work done in better quantifying the energy input into the internal wave field by tidal flows over rough topography (see the review by Garrett and Kunze (2007)) but less in quantifying the energy input by winds.

This thesis was motivated in part by asking how the energy input by wind acting on the ocean mixed layer can generate internal waves and whether those waves could lead to ocean mixing. Waves are usually considered to be important because they can lead to turbulence and mixing. We are investigating the inverse process: how can turbulence generate internal waves?

These turbulently generated internal waves may also be significant in other geophysical applications. The interconnection between turbulence and waves is important to the mixing of biological and chemical nutrients in lakes (Wüest and Lorke (2003)). As the wind blows across the surface of a lake, turbulent eddies can form which may launch waves into the lake which, when they break, can cause localized

mixing. Another example is tailings ponds in the mining industry that are designed to have particles settle to the bottom and where mixing is generally undesirable. Finally, at the top of the troposphere sheared turbulence creates waves that may propagate into the stratosphere. Convective storms impinging upon the base of the stratosphere (Song et al. (2003), Michaelian et al. (2002)) may lead to turbulently generated internal waves.

This thesis hopes to address how significant, in terms of energy, are the waves generated by a shear turbulent layer. Kantha and Clayson (2007) suggested internal waves probably do not extract substantial energy out of the ocean mixed layer such that the turbulent kinetic energy budget needs to be modified. But, since the total amount of energy available in the ocean mixed layer is large, even a comparatively small percentage may be relevant for the energy budget of internal waves. von Storch et al. (2007) used a $1/10^{\circ}$ GCM to show that 3.8 TW of power was generated at the sea surface by the wind and 1.1 TW passed through the surface mixed layer (≈ 100 m) to the ocean beneath. However, Watanabe and Hibiya (2008) have performed simulations that show the vast majority of wind induced energy is dissipated in the top 1000 m of the ocean leaving a relatively small fraction available for deep ocean mixing. We are interested in characterizing the wave energy as a fraction of the turbulent energy of the forcing and determining whether the waves extract an insignificantly small fraction (on the order of $< 0.1\%$ of the energy), a significant but relatively small fraction (on the order of 1%), or a significant and relatively large fraction (on the order of 10%). This can then be used to motivate whether a parametrization for wind driven, turbulently generated internal waves should be developed.

1.2 Background

Here, we summarize previous studies on internal wave generation. Identification of some unresolved questions helped motivate the experiments described in this thesis.

1.2.1 Waves and intrusions

When the door to a house is opened on a calm winter day, cold dense air flows in by the occupant's feet. This is an example of a gravity current, which is an important class of stratified flow (Simpson (1997)). In a stratified fluid, a gravity current will travel at the depth of its neutral buoyancy and is called an intrusive gravity current or an intrusion. The dynamics of both gravity currents and intrusions have been extensively explored using laboratory experiments (e.g. Keulegan (1957); Maxworthy et al. (2002)), numerical simulations (e.g. Birman et al. (2007); Ungarish and Huppert (2002)) and analytical theory (e.g. Benjamin (1968); Ungarish (2006)).

Since an intrusion displaces stratified fluid, it can generate internal waves. In partial-depth lock-release experiments, Sutherland et al. (2007) observed that intrusions can force high frequency internal waves in a stratified ambient. For symmetric intrusions, laboratory experiments in Sutherland and Nault (2007) demonstrated that internal waves play an important role in maintaining a constant intrusion speed for a much greater distance than shallow water theory and numerical simulations would suggest (Ungarish (2005)). When an intrusion is not travelling at the mid-depth of the fluid, the initial intrusion speed is significantly increased (Bolster et al. (2008)). In this thesis, we focus on the properties of the internal waves generated by symmetric and non-symmetric intrusions. We are interested in the impact of internal waves on the long-term evolution of an intrusion in symmetric and non-symmetric cases.

1.2.2 Waves and topography

Winds in the atmosphere and tides in ocean can force fluid to flow over topography. This vertical displacement of stratified fluid generates internal waves. Steady flow of speed U over small-amplitude sinusoidal topography of wave number k can excite internal waves with a frequency of $\omega_{\text{exc}} = Uk$ with an amplitude proportional to the amplitude of the topography (Baines (1982)). This is valid as long as $\omega_{\text{exc}} < N$. If the excitation frequency is higher than the buoyancy frequency, exponentially decaying evanescent waves are forced.

Bell (1975) investigated wave generation by oscillating tidal flow over topography at the bottom of the ocean. As described above, the conversion from the barotropic tide to an internal tide has been the focus of much recent interest as a source of mixing in the deep ocean (Garrett and Kunze (2007)). There have been many numerical and theoretical studies examining the effects of finite depth of the ocean (Khatiwala (2003); Smith and Young (2002)), finite slope of the topography (Balmforth et al. (2002)), steep topography (Llewellyn Smith and Young (2003); St. Laurent et al. (2003)) and three-dimensional topography (Holloway and Merrifield (1999); Munroe and Lamb (2005)) on internal wave generation.

Recent experimental work by Aguilar and Sutherland (2006) looked at the flow of stratified fluid over 'rough topography' (with either rectangular or triangular 'hills'). As with sinusoidal topography, waves were observed if the forcing frequency was less than the buoyancy frequency. However, when the flow was super-critical, where $\omega_{\text{exc}} > N$, a turbulent wake in the lee of the topography could launch internal waves. The frequency was independent of the forcing frequency but equal to a fixed fraction of the buoyancy frequency ($\omega = 0.7N$). In the actual experiment, the topography is towed upside down along the surface of the fluid and the internal waves propagate downwards. By a change in reference frame, this is equivalent to having the fluid moving and the topography stationary. Also, since the flow is Boussinesq, the waves propagating downward can be treated the same as waves propagating upward. In that paper, as in most work on internal waves and topography, the fluid is stratified over the full depth of the fluid. In this thesis, we investigate the effect of a mixed layer adjacent to rough topography on the generation of internal waves for both sub-critical and super-critical flow.

1.2.3 Waves and turbulence

Turbulence is important in the ocean for mixing of biological and chemical nutrients, dispersal of pollutants, and plays a crucial role in the general circulation which is important for climate models (Thorpe (2004)). Turbulent flows can also generate internal waves. These waves can then propagate through fluid transporting energy away from their source.

Previous papers have investigated internal waves generated by turbulent wakes from towed spheres (Bonneton et al. (2006); Diamessis et al. (2005)), from a turbulent bottom Ekman layer (Taylor and Sarkar (2007)), turbulent shear flow (Sutherland and Linden (1998)) and stationary turbulence (Dohan and Sutherland (2005); Linden (1975)). Interestingly, although the forcing spans a broad spectrum of time and length scales, it has been found that the frequency, ω, of the resultant internal waves lies in a fairly narrow band in proportion to the buoyancy frequency, N, namely $\omega/N \approx 0.7$.

Turbulent entrainment of a stratified fluid can generate internal waves. Turbulent entrainment is a well-studied class of problems involving the rate at which either shear-free or sheared turbulence mixes into initially two-layered or continuously stratified fluid (Fernando (1991)). In shear-free experiments with a continuously stratified fluid, it is unclear whether internal waves are (Linden (1975)) or are not (Xuequan and Hopfinger (1986)) significant in changing the entrainment rate as compared to a two-layer fluid in which internal waves are not generated. However, it was only with the mixing box experiments of Dohan and Sutherland (2005), that the focus shifted from the turbulence and the entrainment process to a detailed study of the internal waves generated.

An example of an entrainment study of a continuous stratified fluid with a mean flow is a surface driven flow in an annular tank (Kato and Phillips (1969)). Internal waves were shown to affect significantly the entrainment rate as compared to a two-layered fluid (Kantha et al. (1977)). However, a detailed study of the internal waves has not been performed. In this thesis, we explore the properties of internal waves generated by a turbulent mean flow and especially with reference to the motivational problem of wind-driven turbulence in the mixed layer of the oceans and lakes.

1.3 Experimental considerations

Both laboratory and numerical experiments are used in this thesis to study internal waves. These tools can provide insight into generation mechanisms of internal waves by intrusions, topography, and turbulence.

Laboratory experiments are used because they are able to investigate reproducibly particular fluid dynamical processes under controlled conditions. This provides more direct insight into the underlying mechanisms than what can be obtained by observations of internal waves in field experiments.

Synthetic schlieren (Sutherland et al. (1999)), uses the changes in refraction of light with density to detect non-intrusively vertical displacements of stratified fluids. By knowing the displacement of lines of constant density, linear theory can be used to determine the velocities, amplitudes, frequencies, momentum and energy fluxes of internal waves propagating in the fluid.

To quantify the velocity field in a turbulent flow, particle image velocimetry (PIV) can be used. This is a experimental technique new to our lab but used widely elsewhere. Our version of PIV uses a laser light sheet to illuminate neutrally buoyant particles suspended in the flow. By computing the cross-correlation of video image pairs taken at a small time interval apart, the displacement of the particles and hence the velocity of the fluid can be inferred. From the velocity field, the turbulent kinetic energy can be estimated.

Laboratory experiments are limited, however, in terms of scale. Our experiments are performed in relatively small tank where the presence of walls limits the applicability of the results to, say, the ocean. Numerical studies provide one way of overcoming that limitation. Like with an analytical model, a numerical simulation is essentially a mathematical model which tries to capture the essential physics of the problem and makes assumptions about which approximations are appropriate. Here, direct numerical simulations are used to solve the equations of motion. These provide additional information and verify some of the conclusions of the laboratory experiments notwithstanding the experimental limitations.

1.4 Thesis overview

The thesis begins with an experimental investigation in chapter 2 of internal wave generation by an intrusive gravity current. Dye was used to identify the intrusion and horizontal dye lines were used to visualize the waves. The internal waves are

shown to impact significantly the evolution of the intrusion by propagating faster and taking energy away from the current.

Chapter 3 reports on the results of towed topography laboratory experiments. This experimental apparatus, which was based on the setup used in Aguilar (2005), consisted of a shallow mixed upper layer and a deep continuously stratified lower layer. A source of turbulence, namely a rectangular wave form representing isolated rough topography, was dragged through the upper layer. Internal waves could freely propagate in the lower layer. The internal waves were measured using synthetic schlieren to determine the frequencies of the generated waves. The original intention was to examine the internal waves and relate their properties to those of the turbulent wake behind the towed topography. However, it was determined that this apparatus was inappropriate for studying the coupling between sheared turbulence and waves because it did not distinguish waves generated from the turbulent wake from waves produced by flow over the topography. We did show that even with a surface mixed layer, and consistent with previous studies, stratified flow over isolated rough topography generated waves in a narrow range of a fixed fraction of the buoyancy frequency.

Chapter 4 describes and analyzes the experimental results of an original experimental setup involving a moving conveyor belt apparatus positioned at the surface that continuously forces a stratified fluid. In these experiments a turbulent mixed layer developed and internal waves were observed to propagate away. This lid-driven cavity flow has similarities with previous mixing box experiments (e.g. Dohan (2004)) but explicitly forces a mean shear. Conceptually, the setup represents the physical scenario of the wind forced ocean mixed layer which was the original motivation for this work. Particle image velocimetry was used to measure the velocity field and hence the turbulence in the mixed layer and synthetic schlieren was used to measure the waves in the stratified ambient. Empirical results are presented. Most significantly, it is shown that the energy density of the wave field is on the order of 2-3% of the turbulent kinetic energy density of the mixed layer.

Chapter 5 presents direct numerical simulations that validate and extend the laboratory results from the conveyor belt chapter. Two-dimensional simulations in a

horizontally periodic domain show the same qualitative features as the corresponding laboratory experiments. In particular, it is demonstrated that the conveyor belt experiments can be assumed to be essentially two-dimensional and that the presence of tank walls are not critical to the empirical results. Additionally, an energy budget is constructed which suggests that on the order of 10% of the energy input by the surface forcing is transferred to the internal wave field.

Finally, in chapter 6 the interconnections between each of these distinct projects is examined and future work is suggested.

Chapter 2

Intrusive Gravity Currents and Internal Waves

An initial project completed during the course of this PhD was a laboratory experiment on the generation of internal waves by intrusive gravity currents. The content presented in this chapter was published in the *Journal of Fluid Mechanics* as Munroe et al. (2009). That paper also included a section on the numerical modelling of the flow. Since the author of this thesis did not do the modelling or write up those results, the numerical section has been omitted from this chapter.

2.1 Introduction

Gravity currents are flows driven by horizontal density variations. In the simplest arrangement, heavy fluid flows beneath a uniform ambient. This describes a bottom-propagating gravity current and models natural examples such as sea breezes or cold thunderstorm outflows. At sufficiently large spatial and slow temporal scales a gravity current may be affected by a continuously stratified ambient and, in particular, may generate internal gravity waves. An internal gravity wave is caused by the displacement of a fluid parcel from rest which responds to a restoring force due to buoyancy. This interaction can be more substantial if the density of the gravity current matches the density of the stratified ambient at some vertical level, in which case it is referred to as an intrusion. Such a circumstance may arise, for example, at the outflow of a thunderstorm near the tropopause or when a rising plume spreads horizontally where it encounters an atmospheric inversion (see Simpson (1997) for

a comprehensive review of examples of gravity currents in environmental and industrial contexts.)

In laboratory experiments the most commonly studied gravity current is heavy fluid propagating along a rigid bottom boundary beneath a uniform ambient (Benjamin, 1968; Britter and Simpson, 1978; Huppert and Simpson, 1980; Keulegan, 1957; Klemp et al., 1994; Shin et al., 2004; Simpson, 1972; Simpson and Britter, 1979). In a typical lock-release experiment in a long rectangular tank, a finite volume of uniform-density salt water is held behind a gate in a lock. On the other side of the gate is uniform ambient fluid. When the gate is removed, horizontal density differences establish a horizontal pressure gradient which causes the current to flow into the ambient and the ambient to move backward into the lock as a return flow. Observations show that the speed of the gravity current is constant for several lock lengths. A prediction of this speed was given by the analytical theory of Benjamin (1968) which examined the prototype problem of the gravity current of a heavy fluid of density ρ_c propagating beneath lighter fluid of density ρ_a. For a steady current, the front speed, U, is given by

$$U = \mathrm{Fr}_B \sqrt{g' H} \tag{2.1}$$

where $g' = g(\rho_c - \rho_a)/\rho_a$ is the reduced gravity, H is the total depth of the fluid, and Fr_B is the Froude number. Using mass and momentum conservation within a control volume, Benjamin (1968) determined that

$$\mathrm{Fr}_B(\tilde{h}) = \sqrt{\frac{\tilde{h}(1-\tilde{h})(2-\tilde{h})}{1+\tilde{h}}}, \tag{2.2}$$

in which $\tilde{h} = h/H$ is the relative depth of the current head. In particular, for an energy-conserving current released from a full-depth lock, $h = H/2$ and $\mathrm{Fr}_B = 1/2$.

Bottom-propagating gravity currents beneath a two-layer ambient were examined by Rottman and Simpson (1983), and the first experiments and simulations of a gravity current travelling along a rigid bottom under a continuously stratified fluid were performed by Maxworthy et al. (2002). The latter found an empirical relationship between the speed of the front of the gravity current and the parameters of the

system such as the density of the current and the strength of the stratification. By analogy with (2.1) they found

$$U = \mathrm{Fr} N H, \tag{2.3}$$

in which N is the buoyancy frequency, which characterized the stratification of the ambient, and Fr is the Froude number appropriate for gravity currents in a stratified ambient. For gravity currents having the same density as that at the base of the ambient, they found Fr $\simeq 0.266$. They also determined that the aspect ratio of the lock is unimportant as far as the initial dynamics of the gravity current were concerned. They were interested in the transition from the supercritical case to the subcritical case. In the supercritical case the current travelled faster than the fastest long wave speed and no internal waves were generated. In the subcritical case, internal waves were generated and these were observed to act back upon the gravity current causing it to advance in a pulsating fashion.

Using an extension of shallow water theory from homogeneous to stratified ambients, Ungarish and Huppert (2002) showed that their model well captured the initial slumping phase of such bottom propagating gravity currents observed both in fully nonlinear numerical simulations and in experiments. Specifically, the speed was predicted by (2.3) with

$$\mathrm{Fr} = \mathrm{Fr}_B(\tilde{h})(1 - S + S\tilde{h}/2)^{1/2}, \tag{2.4}$$

in which $S = (\rho_b - \rho_0)/(\rho_\ell - \rho_0)$ is the ratio of the density difference between the bottom and top of the ambient to the density difference between the lock-fluid and the top of the ambient. The prediction was developed for bottom-propagating gravity currents, in which case $0 \leq S \leq 1$ (Ungarish (2006)). For a full-depth lock-release current, one expects $\tilde{h} = 1/2$ in which case $\mathrm{Fr}_B = 1/2$, as above. If the lock fluid density matches that at the bottom of the ambient, $S = 1$ and so Fr $=$ Fr$_0$ $\equiv 1/4$. This result lies in close agreement with the experimental observation of Maxworthy et al. (2002).

More recently Ungarish (2006) derived an analytic model based upon shallow water theory that predicted the long-time evolution of bottom propagating gravity currents. These results were compared with numerical simulations (Birman et al.

(2007)) and showed good agreement for shallow-depth currents ($\tilde{h} \ll 1/2$) in relatively weakly stratified fluids. For subcritical currents in strong stratification the theory predicted multiple solutions for the current speed and the simulations showed the current speed matched better with solutions slower than the fastest predicted speed.

The evolution of intrusions is less understood than that of gravity currents (Britter and Simpson (1981); Holyer and Huppert (1980); Lowe et al. (2002); Monaghan (2007); Sutherland et al. (2004)). By allowing the interface ahead of an intrusion to be vertically displaced, Benjamin's (1968) theory was adapted to predict the propagation speed of intrusions in a two-layer fluid (Flynn and Linden (2006)). This speed was predicted on heuristic grounds by Cheong et al. (2006) (hereafter referred to by "CKL"), who estimated the speed by relating the available potential energy of the system before the lock-fluid was released to the consequent kinetic energy of the intrusion.

Numerous experiments have been performed that examine the speed and structure of intrusions propagating at mid-depth in uniformly stratified ambient, these resulting either from a full-depth lock-release (Sutherland and Nault (2007)) or from a localized mixed patch (Amen and Maxworthy (1980); Manins (1976); Schooley and Hughes (1972); Silva and Fernando (1998); Sutherland et al. (2007); Wu (1969)).

Only recently have laboratory experiments been performed to examine the asymmetric circumstance of intrusions propagating at arbitrary depth in a uniformly stratified fluid (Bolster et al. (2008)). These authors extended the CKL result by fitting a quadratic to the mid-depth, top and bottom propagating intrusion speeds, that were predicted by (2.3) with $\mathrm{Fr}_0 = 1/4$ (Ungarish (2006); Ungarish and Huppert (2002)) and $\mathrm{Fr}_0 = 0.266$ (Maxworthy et al. (2002)). Thus they heuristically predicted that the speed of an intrusion propagating at depth h_L is given by (2.3) with

$$\mathrm{Fr} = \mathrm{Fr}_0 \sqrt{3\left(\frac{h_L}{H} - \frac{1}{2}\right)^2 + \frac{1}{4}}. \tag{2.5}$$

They found good agreement with both numerical simulations and laboratory experiments, the theory more closely matching the experimental results using $\mathrm{Fr}_0 = 1/4$.

Whereas Bolster et al. (2008) examined the initial intrusion speed, this paper focuses upon the generation of internal waves by asymmetric intrusions and studies the consequent influence of internal waves upon the long-time evolution of the intrusion. The length of the lock is small compared with the full length of the tank so that the initial behaviour of the intrusions can be examined as well as the long-time behaviour which is affected by the motion of internal waves in the ambient. In these experiments intrusions were created by having an intermediate density between the average density of the ambient and the density at the base of the stratification. We also conducted experiments in which the density of the fluid in the lock exceeded that of the bottom of the stratification. As such these investigations bridge the gap between studies of a bottom-propagating current and of a symmetric intrusion in a uniformly stratified ambient.

Shallow water theory and numerical simulations (Ungarish (2005)) have predicted that the intrusion should evolve from a steady state (constant speed) phase to a decelerating (self-similar) phase. Such behaviour is anticipated by shallow-water theory (Ungarish (2006)) because the current speed is predicted to decrease as the current depth decreases according to (2.4). However, our experiments show this is not the case for intrusions released from a full-depth lock. Consistent with Sutherland and Nault (2007), symmetric intrusions are found to propagate at constant speed up to 20 lock-lengths with no appearance of a self-similar phase. This occurs despite the fact that the head height continuously decreases with distance from the lock. Such behaviour occurred because the intrusion evolved into the form of a closed-core solitary wave. For asymmetric intrusions, the return flow launches internal waves that reflect off the lock-end of the tank and then catch up with the intrusion head, halting its advance. Until this occurs the intrusion propagates as constant speed even as the waves act to reduce the head depth to zero. Internal waves thus play an important role in the long-time evolution of intrusions as we show quantitatively through an analysis of the wave properties both in experiments and in numerical simulations.

The paper is organized as follows. The experimental setup and analysis methods are described in section 2.2 and the experimental results are presented in sec-

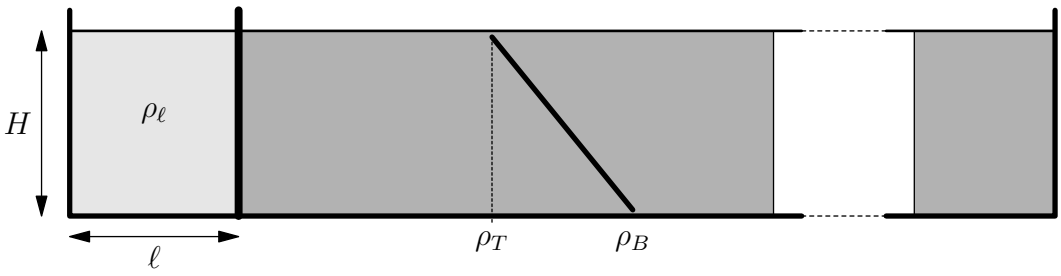

Figure 2.1: Setup and definition of parameters for intrusion experiments.

tion 2.3. The analyses focus upon the intrusion speed and the impact of internal gravity waves generated by the intrusion and upon how the waves can cause the intrusion to stop before reaching the end of the tank. Conclusions and future work are given in section 2.4.

2.2 Experimental setup and analysis

Experiments were performed in a glass tank measuring $L = 197.1$ cm long by 17.4 cm wide by 48.5 cm tall as shown in figure 2.1. The tank was left open to the atmosphere at the top. Salt water with a linearly stratified density profile filled the tank using the standard 'double bucket' technique (Oster, 1965). Dye lines of red food colouring were added every 5 cm while the tank was being filled in order to visualize internal gravity waves generated in the experiment. The total depth, H, of the ambient was either 30 cm or 15 cm for all experiments. The strength of the stratification, measured by the buoyancy frequency

$$N = \sqrt{-\frac{g}{\rho_0}\frac{d\rho}{dz}}, \tag{2.6}$$

varied between 0.34 s^{-1} and 2.0 s^{-1} (bottom to top density differences between 0.003 and 0.14 g cm^{-3}) for different experimental runs. A vertically traversing 50 cm long Fast Conductivity and Temperature Probe (Precision Measurement Engineering) was used to measure the density profile of the stratification. The probe was recalibrated before each experiment.

The experiments had corresponding Reynolds numbers, based upon N and H, ranging from Re$(= NH^2/\nu) \simeq 8 \times 10^3$ to 1.8×10^5. These values were sufficiently

large that viscosity was not expected to play a significant role in the dynamics of the intrusions. The Schmidt number was Sc $= 10^3$.

After filling the tank, a 0.4 cm thick gate was inserted between a pair of vertical glass guides to create a water-tight lock at one end of the tank. The length of the lock was set to $\ell = 8.5$ cm, 18.5 cm, or 38.5 cm. Most of the experiments were performed with a lock length of $\ell = 18.5$ cm.

A small amount of blue dye was added to the fluid in the lock and the contents were vigorously stirred until the lock-fluid had uniform density. The dye allowed the intrusion to be visualized during the experiment and was introduced in sufficiently low concentrations that it did not significantly change the density of the fluid in the lock.

In some experiments, additional salt was added to the lock-fluid before its contents were mixed. After mixing, the density of the lock was measured using a hydrometer placed in the lock. In some experiments, the density was measured using an Anton Paar Densitometer.

The intrusion propagated at a depth such that the density of the lock-fluid was equal to the density of the undisturbed stratified fluid at that depth. If no salt was added, the lock-fluid density, ρ_ℓ, was the average, $\bar{\rho}$, of the density at the top, ρ_T, and the density at the bottom, ρ_B, of the ambient and the intrusion travelled at mid-depth, $h/H = 1/2$. Here h is the vertical position of the intrusion measured from the bottom of the tank and H is the total depth of the ambient. Adding salt to the lock increased the density of the lock-fluid. If $\bar{\rho} < \rho_\ell < \rho_B$, the intrusion propagated between the bottom and mid-depth. Since the stratification was linear, we can calculate this intrusion depth to be $h/H = (\rho_B - \rho_\ell)/(\rho_B - \rho_T)$. Analogous to Sutherland et al. (2004), the depth can be characterized by a non-dimensional parameter

$$\epsilon = \frac{\rho_\ell - \bar{\rho}}{\rho_B - \rho_T}. \tag{2.7}$$

Note that $h/H = 1/2 - \epsilon$, so both h/H and ϵ are measures of the relative density of the lock-fluid subject to $0 < h/H < 1$ and $-1/2 < \epsilon < 1/2$ for $\rho_T < \rho_\ell < \rho_B$. If $\rho_\ell \geq \rho_B$ then the intrusion runs along the bottom of the tank and $\epsilon > 1/2$ even though $h/H = 0$. Although we did not run any experiments where $\rho_\ell < \bar{\rho}$

(which correspond to $\epsilon < 0$ or $h/H > 1/2$) we assume the experiment is symmetrical about $\epsilon = 0$ since the problem is Boussinesq. When $\epsilon > 1/2$ the gravity current runs along the bottom and when $\epsilon < -1/2$ the gravity current runs along the surface. The choice of a non-dimensional parameter for density is not unique. For example, in Maxworthy et al. (2002) the relative density was represented by $R = (\rho_\ell - \rho_T)/(\rho_B - \rho_T)$. We have chosen to use ϵ because it serves to emphasize the symmetry of the problem.

A digital video camera (3 CCD Sony DVD Steadycam) was positioned $3.5\,\mathrm{m}$ from the front of the tank so that the entire length of the tank was in the camera's field of view. Each experiment was recorded onto video tape for later analysis. The frame rate was as small as $\Delta t = 1/30\,\mathrm{s}$ and the spatial resolution allowed disturbances as small as $\Delta z \simeq \Delta x \simeq 0.4\,\mathrm{cm}$ to be visualized. The dynamics of the system were primarily two dimensional, as corroborated by the numerical simulations discussed later. Thus we did not analyze the cross-tank structure of the gravity current as it evolved.

After the tank was set up, the gate was quickly removed. An unavoidable side effect of this procedure was to introduce turbulence (and hence mixing) as fluid is dragged along by the upward movement of the gate. As is typical in lock-release experiments (Simpson (1982)), this mixing did not significantly affect the evolution of the intrusion after propagating a small distance from the lock.

After the removal of the gate, the lock-fluid collapsed into an intrusive gravity current which propagated horizontally along the length of the tank. The centre of the current was at a neutrally buoyant depth. We marked the end of the experiment as the point in time at which the far end-wall effects, such as the reflection of waves, started to impact the evolution of the intrusion.

The "DigImage" software package (Dalziel, 1992) was used to perform most of the analyses. One of the features of DigImage was to create horizontal and vertical time-series from the raw video signal recorded during the experiment. A horizontal time-series was constructed by choosing a vertical position (a particular pixel coordinate), extracting a row of pixels at that height from successive frames of the video and vertically stacking these horizontal slices. Vertical time-series were

created in a similar manner from successive vertical slices.

To measure the position of the gravity current as a function of time, we used a horizontal time-series taken at a vertical position corresponding to the depth of the intrusion. The front of the intrusion was identified in the horizontal time-series by the diagonal contour separating the darkly dyed intruding lock-fluid and the relatively light intensity ambient. This is shown, for example, in figure 2.2a. The horizontal time series was taken at the horizontal level corresponding to the neutral buoyancy level of the lock fluid. After a brief acceleration time, the intrusion propagated at a nearly constant speed, $U_{\rm gc}$. The distance over which the intrusion propagated in steady-state depended upon the consequent interaction between the intrusion and internal waves. In all experiments, the speed was found to be constant between 1 lock-length and at least 3 lock-lengths from the gate. The velocity of the intrusion-head was thus determined by finding the slope of the line, typically between 1 and 3 lock-lengths from the gate, as indicated in figure 2.2a. As was characteristic of all experiments, the intrusion travelled at an initial constant speed at least up to 3 lock-lengths. We denote the horizontal distance travelled by the intrusion before the nose velocity first became zero as the propagation distance, $L_{\rm max}$, which is also indicated on figure 2.2a. The notation $L_{\rm max}$ is not meant to indicate that the intrusion goes no further than this distance. At later times the intrusion moves forward in a pulsating way but, as we will show, this is a consequence of internal waves advecting the lock-fluid as was observed by Maxworthy et al. (2002). The motion does not result from horizontal density gradients establishing horizontal pressure gradients, which is the mechanism usually ascribed to drive a gravity current.

The dye-lines added when the tank was being filled allow for the analysis of internal waves generated by the intrusion. In most experiments we measured the wave phase speed, $c_{\rm p}$, of the first wave generated by creating a horizontal time-series at the $z = 25$ cm dye-line from the bottom of the tank (e.g. figure 2.2b). The superimposed vertically offset lines indicate slopes used to measure speeds. Because the intrusions propagated at mid-depth or below, a horizontal time-series at this height revealed a clear signal of the dye-line being displaced by the waves

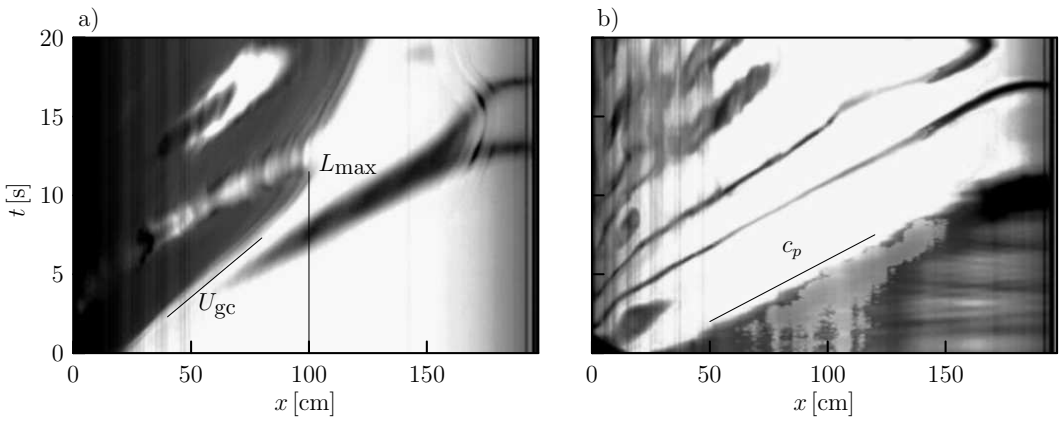

Figure 2.2: (a) Horizontal time-series taken from experiments with $\epsilon = 0.27$, $H = 30$ cm, $N = 1.8\ \mathrm{s}^{-1}$, and $\ell = 18.5$ cm. The time series is taken from a horizontal slice through movies of the experiment situated $z = 7.5$ cm above the bottom of the tank close to the neutral buoyancy level of the lock fluid. The superimposed solid lines show the intrusion speed, $U_{\rm gc}$ and propagation distance, $L_{\rm max}$. The sloped dark wedge ahead of the intrusion results from the vertical displacement of a dye-line through the level $z = 7.5$ cm. The displacement occurs due to internal waves launched ahead of the intrusion. (b) Horizontal time-series taken from the same experiment at the $z = 25$ cm. The superimposed solid line indicates the phase speed of internal waves moving ahead of the intrusion. The slope dark lines occurring at later times result from the dye line at $z \simeq 25$ cm moving vertically through the plane $z = 25$ cm above and behind the intrusion head.

without contamination by the intrusion itself. The slope of the contour in the horizontal time-series marking the initial displacement of the dye-line allowed us to compute the phase speed.

The frequency of the waves were found by using a vertical time-series at $x = 60$ cm from the lock-end of the tank, as shown in figure 2.3. We measured the time, ΔT, between the first crest and first trough to pass this point. We estimated the period to be $T = 2\Delta T$ and the frequency to be $\omega = 2\pi/T$.

The internal wave amplitude was found by measuring the maximum displacement of each dye line and dividing by two as shown for the third dye-line in figure 2.3. These amplitude measurements were performed using vertical time-series at $x = 60$ cm and $x = 160$ cm from the lock-end of the tank.

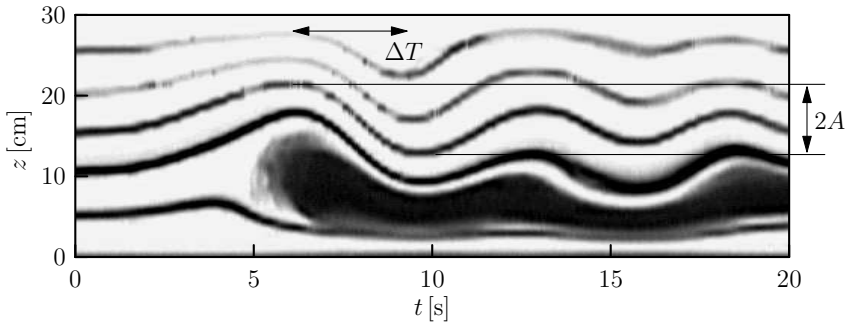

Figure 2.3: Vertical time-series from experiment with $\epsilon = 0.27$ taken at $x = 60$ cm showing the measurement of the half-period, ΔT, of the leading internal wave and the measurement of the peak-to-peak displacement, $2A$, of a dye-line.

2.3 Experimental results

Figures 2.3, 2.5, and 2.6 show three experiments demonstrating the characteristic behaviour of symmetric ($h/H = 1/2$), asymmetric ($0 < h/H < 1/2$) and bottom-propagating ($h/H = 0$) intrusions. For these experiments, the depth of the tank was $H = 30$ cm, the lock length was $\ell = 18.5$ cm, and the buoyancy frequency ranged from $N = 1.7 - 2.0$ s^{-1}.

For the experiment shown in figure 2.3, no salt was added to the lock so that $\epsilon = 0$. In this case the intrusion travelled down the middle of the tank. In the initial collapse stage at $t = 2$ s (figure 2.3a) the lock-fluid intrudes into the ambient and a return flow above and below the intrusion moves into the lock. The asymmetry in the return flow occurs because the gate is not removed instantaneously. At $t = 7$ s (figure 2.3b) a clear head develops which travels at a constant speed along the tank with a sinuous tail in its lee. At $t = 21$ s (figure 2.3d) the intrusion head has thinned considerably and the intrusion reaches the end of the tank. The leading internal wave is locked to the head of the intrusion and dye-lines are displaced only slightly in front of the head. The dye-lines reveal the existence of a mode-2 internal wave, for which dye-lines displace upward in the top half and downward in the bottom half of the tank.

In figure 2.5, salt was added to the lock so that $\epsilon = 0.27$. Note that the intrusion is asymmetric. In the initial collapse stage at $t = 2$ s (figure 2.5a) the dark lock-fluid intrudes into the ambient with return flows occurring above and below. In

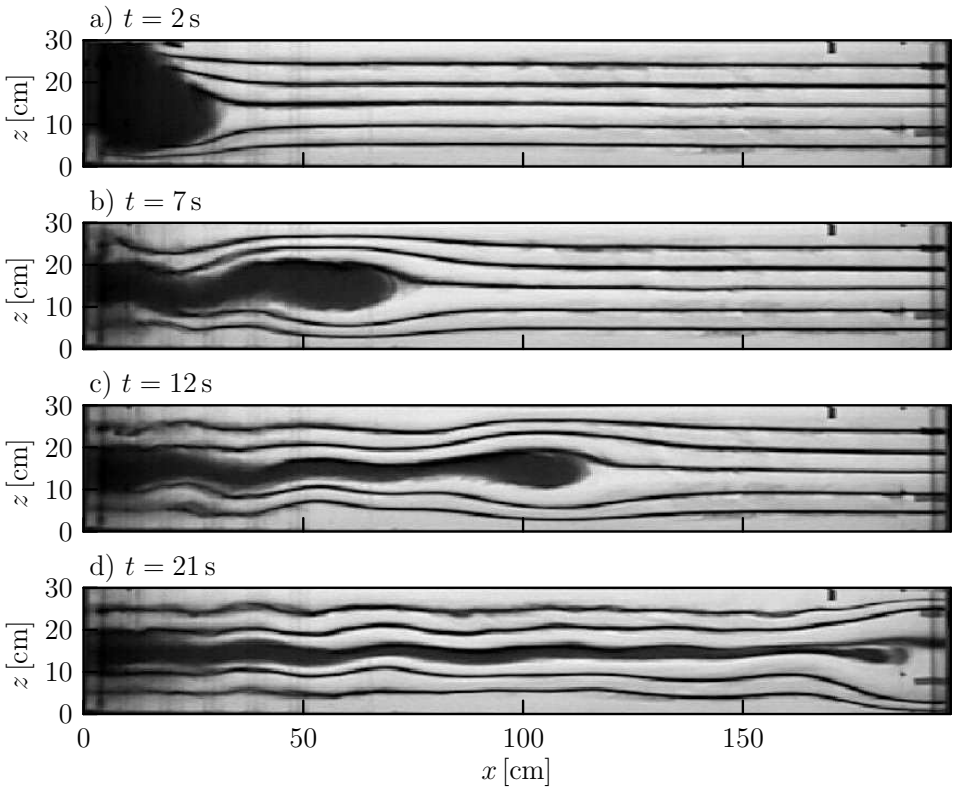

Figure 2.4: Snapshots from experiment with $\epsilon = 0$, for which the intrusion travels along the middle of the tank, at times (a) $t = 2$ s ($Nt \simeq 2$), (b) $t = 7$ s ($Nt \simeq 14$), (c) $t = 12$ s ($Nt \simeq 20$) and (d) $t = 21$ s ($Nt \simeq 42$).

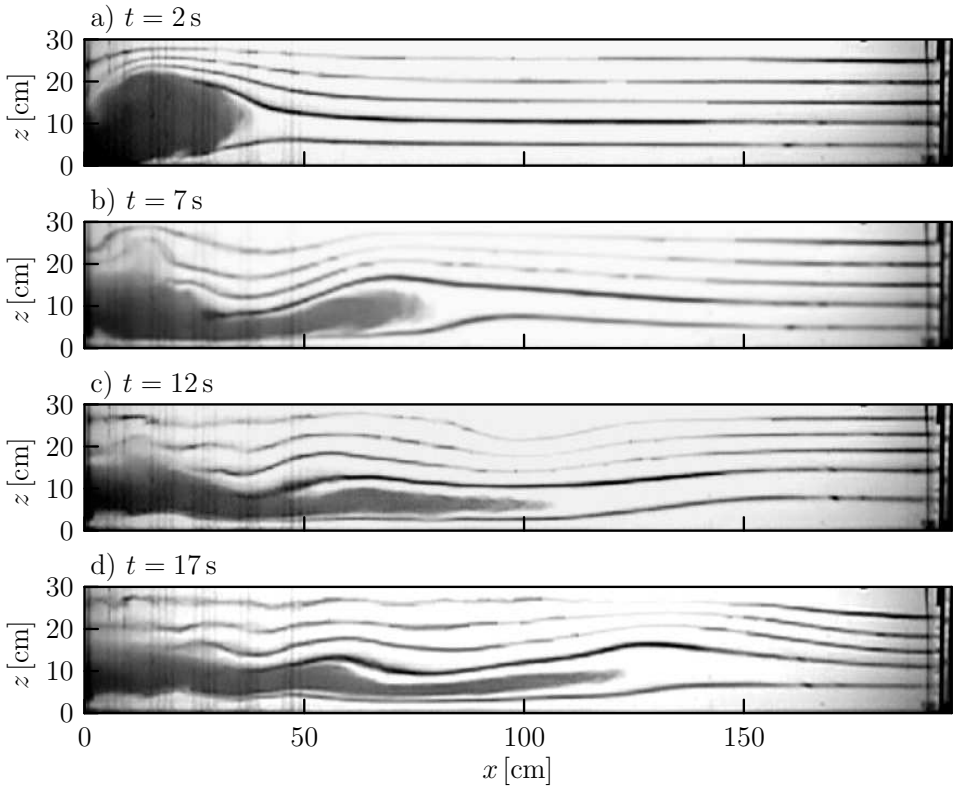

Figure 2.5: As in figure 2.3 but for an experiment with $\epsilon = 0.27$: (a) $t = 2$ s ($Nt \simeq 3.4$), (b) $t = 7$ s ($Nt \simeq 11.8$), (c) $t = 12$ s ($Nt \simeq 20.2$) and (d) $t = 17$ s ($Nt \simeq 28.7$). Corresponding horizontal and vertical time series are shown in figures 2.2 and 2.3, respectively.

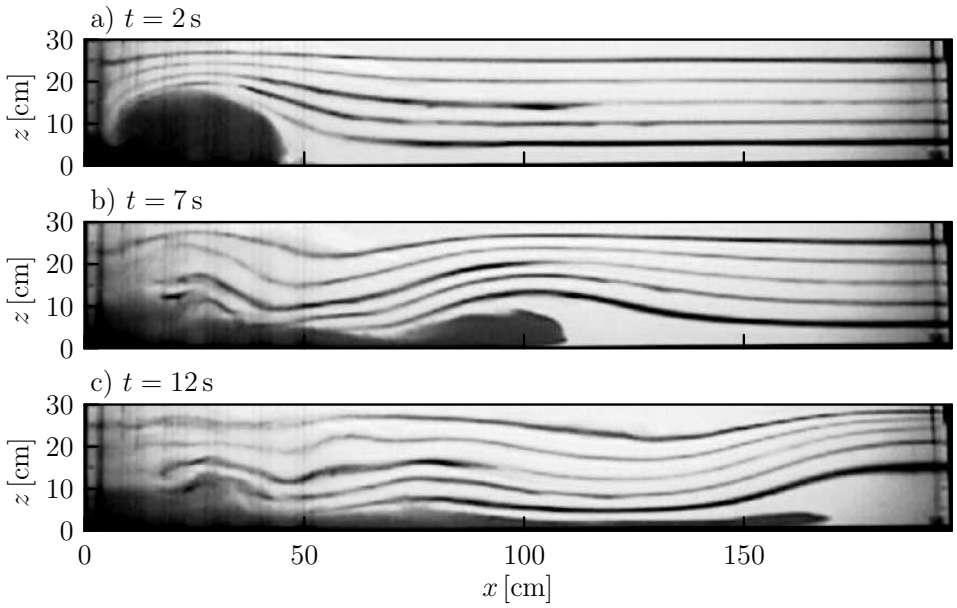

Figure 2.6: As in figure 2.3 but for $\epsilon = 0.54$: (a) $t = 2$ s ($Nt \simeq 3.6$), (b) $t = 7$ s ($Nt \simeq 12.6$)and (c) $t = 12$ s ($Nt \simeq 21.6$).

figure 2.5b a clear head develops shortly after being released. The intrusion propagates at a constant speed until $t = 12$ s (figure 2.5c) at which time the intrusion head gradually collapses due to the advance from behind of an internal wave generated by the return flow. The leading wave is far in advance of the head and has reached the end of the tank. After stopping, the lock-fluid is effectively incorporated into the wave-field. In the image shown at 17 s (figure 2.5d) the dyed fluid has been carried a short distance forward of the original stopping distance through the action of the waves. The motion of the front of the intrusion head over time is more clearly shown through the horizontal time series in figure 2.2a.

In figure 2.6, salt was added to the lock so that $\epsilon = 0.54$. The current travelled along the bottom of the tank. In the initial collapse stage at $t = 2$ s (figure 2.6a) lock-fluid flows beneath the ambient fluid. The ambient fluid flows above the lock-fluid into the lock. At $t = 7$ s (figure 2.6b) the current with a clearly defined head is propagating at a constant speed. There is a small wedge of undyed fluid beneath the head. Since the lock-fluid was slightly more dense than the bottom density of the ambient there must have been some entrainment of ambient fluid to lower the density of the head, for example, through interactions with the viscous bottom

boundary layer (Härtel et al. (2000)). At $t = 12$ s (figure 2.6c) the head is a thin wedge shape and the leading wave has reached the end of the tank. The dye-lines indicate a mode-1 internal wave for which all the dye-lines are displaced upwards above the current head.

In experiments with still larger $\epsilon \gtrsim 0.65$ (not shown) the gravity current excites mode-1 waves but the current is observed to propagate nearly to the end of the tank before its speed is affected by interactions with the wave reflecting from the end-wall of the tank.

2.3.1 Intrusion speed

In all our experiments, after a brief acceleration time the gravity current propagated at a constant speed for a distance along the tank. Figure 2.7 shows the initial intrusion speed as a function of the relative density of the lock-fluid. The error bars on ϵ indicate the sensitivity in determining this parameter from traverse data. The appropriate characteristic scaling of the intrusion speed is given by NH in which N is given by (2.6). The minimum intrusion speed occurs when $\epsilon = 0$, which corresponds to the density of the lock-fluid being equal to the average density of the ambient. As ϵ moves away from zero, the speed of the intrusion increases although its speed does not change much for $0 \leq \epsilon \lesssim 0.2$. As the system makes the transition from an intrusion to a bottom-propagating current the speed increases significantly with ϵ.

These intrusion results are compared with the prediction of Bolster et al. (2008) (eq. (2.5)), which is recast in terms of the ϵ parameter to give

$$\frac{U_{\text{gc}}}{NH} = \text{Fr}_0 \sqrt{3\epsilon^2 + 1/4}, \tag{2.8}$$

in which we use $\text{Fr}_0 = 0.25$, as predicted by Ungarish (2006). The curve is plotted as the solid line in figure 2.7. Consistent with Bolster et al. (2008) (who also examined $-0.5 < \epsilon < 0$ cases), we find the theory agrees well with the observed speeds.

The good fit might be expected because (2.8) results from making a quadratic fit to the square of the velocity as a function of ϵ insisting only that the speed in the case

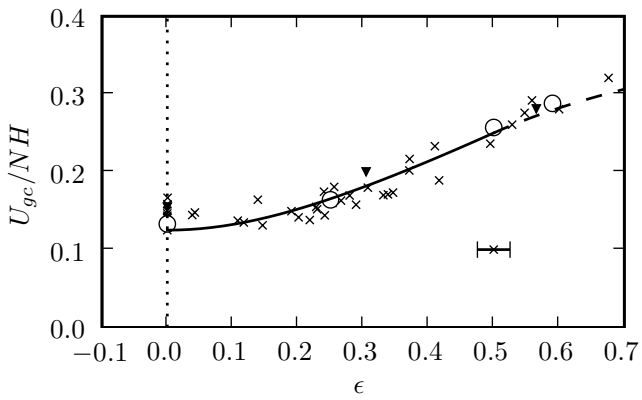

Figure 2.7: Relative intrusion speed plotted against ϵ as measured in experiments with $\ell = 18.6\,\text{cm}$ and $H = 30\,\text{cm}$ (crosses) and $H = 15\,\text{cm}$ (upside-down triangles). The open circles show the corresponding measurements determined from four numerical simulations. Plotted as a solid line is the predicted speed of intrusions determined by the adaption of CKL theory Bolster et al. (2008) as given by eq. 2.8. The dashed line shows the prediction of shallow water theory for bottom-propagating gravity currents as given by eq. 2.9. Typical errors in the estimate of ϵ are shown toward the lower right-hand corner of the plot.

$\epsilon = 1/2$ is set by $\text{Fr}_0 = 1/4$. By symmetry, the speed in the case $\epsilon = 0$ should be half this value and the change in speed as a function of ϵ should be zero about $\epsilon = 0$. One could also form a good quadratic fit by requiring the speed, not the square of the speed, be quadratic. However, Bolster et al. (2008) argue that fitting the square of the speed is appropriate on energetic grounds. The available potential energy stored in the lock is released both to the motion of the intrusion and the kinetic and available potential energy of the ambient. Assuming the partition of energy into the intrusion and ambient are in proportion, it is appropriate to compare the kinetic energy of the intrusion, proportional to its velocity squared, to the available potential energy of the lock-fluid.

The speed of bottom-propagating currents (for which $\epsilon > 1/2$) is influenced not only by the available potential energy of the lock-fluid but also by the normal force of the bottom of the tank acting upon the current. Such effects were accounted for by Ungarish (2006), who used Long's model (Long (1953, 1955)) and shallow water theory to extended Benjamin's theory (Benjamin (1968)) to gravity currents in stratified environments. Recasting (2.4) in terms of ϵ and using $\tilde{h} = 1/2$, appropri-

ate for a full-depth lock release, the speed is predicted to be

$$\frac{U_{\mathrm{gc}}}{NH} = \mathrm{Fr}_0 \sqrt{\frac{4\epsilon - 1}{\epsilon + 1/2}}, \tag{2.9}$$

Here we have related S to ϵ using $S = 1/(|\epsilon| + 1/2)$. This curve is plotted as the dashed line in figure 2.7 for $\epsilon \geq 1/2$.

We find that the theory does reasonably well though it moderately underpredicts the speed of currents with $\epsilon \simeq 0.7$. This could be a consequence of experimental error, however a similar discrepancy between numerical simulations and shallow water theory for full-depth lock-release currents was noted by Birman et al. (2007). Nonetheless, the agreement is promising considering that the full-depth lock-release case is an extreme extension of shallow water theory: predicting the current speed is 'problematic' because of the strong return flow in the ambient above the intrusion (Ungarish (2006)).

The agreement may lead one to conclude that the excitation of internal waves is inconsequential in establishing the steady-state speed. However, the situation is more 'subtle' than this (Bolster et al. (2008)). The very process of collapse means that the stratified ambient must be displaced above and below the head of the intrusion, a process that extracts part of the available potential energy from the lock fluid and which necessarily excites internal waves if not ahead of the current, certainly in its lee. In part for this reason, but also because the mean ambient density ahead of the intrusion is reduced, the Froude number for a bottom propagating current with $\epsilon = 1/2$ is $\mathrm{Fr}_0 \simeq 1/4$ (Ungarish (2006)) and not $\mathrm{Fr}_0 = 1/2$, as would be the case for a gravity current in a uniform-density ambient (Benjamin (1968)).

The discussion so far has focused upon the initial speed of the intrusion and bottom-propagating gravity currents. But the main interest of this paper is upon the its consequent evolution. Shallow water theory predicts that the currents decelerate after propagating one lock length as a consequence of the decreased depth of the current head (e.g. see Fig. 4 of Ungarish (2006)). However, we find this is not the case. Not only does the available potential energy released from the lock go into the kinetic energy of the current, but it is also transformed into the available potential energy and kinetic energy of the ambient. It is the transformation of energy into the

latter and the consequent interactions between the ambient and intrusion that results in intrusions propagating long distances from the lock at constant speed even as the intrusion head height decreases. In intermediate ϵ cases, the ambient can then act abruptly to halt its advance.

Clearly the return flow plays an important role in the generation of internal waves and their consequent impact upon the flow evolution. In the following subsection we examine the observed characteristics of these waves and so estimate the relative energy associated with wave generation and their consequent impact upon the intrusion head.

2.3.2 Internal gravity waves

The release of the lock-fluid generated internal waves, which were visualized by the vertical deflection of the horizontal dye-lines in the tank. The internal waves were vertically trapped between the rigid bottom of the tank and the free surface. The properties of the internal gravity waves generated in this experiment are set by the geometry of the tank, the stratification of the ambient, and the density of the intrusion. The characteristics of the leading internal wave were determined from the initial displacement of the dye-lines occurring in advance of the head of the intrusion. It is assumed that the trailing internal waves resulting from the return flow that reflects off the end-wall of the lock have the same characteristics as the leading waves. For example, horizontal time-series as shown in figure 2.2 reveal the phase speed of leading wave (indicated by the superimposed line labelled c_p) and that of the trailing waves (indicated by the slope of the black dye lines occurring approximately 5 and $10\,$s later) consistently match.

Figure 2.8 shows the phase speed, c_{p}, plotted against the gravity current speed, U_{gc}. For $\epsilon = 0$, the waves travel at the same speed as the gravity current and are consistent, for example, with the experiment shown in figure 2.3. As ϵ increases from 0, the wave speed increases quickly while the gravity current speed increases slowly, consistent with figure 2.7. The internal waves no longer couple to the head of the current but propagate well in front of it. Simultaneously, upon reflection from the end-wall of the lock, the return flow excites internal waves that catch up with

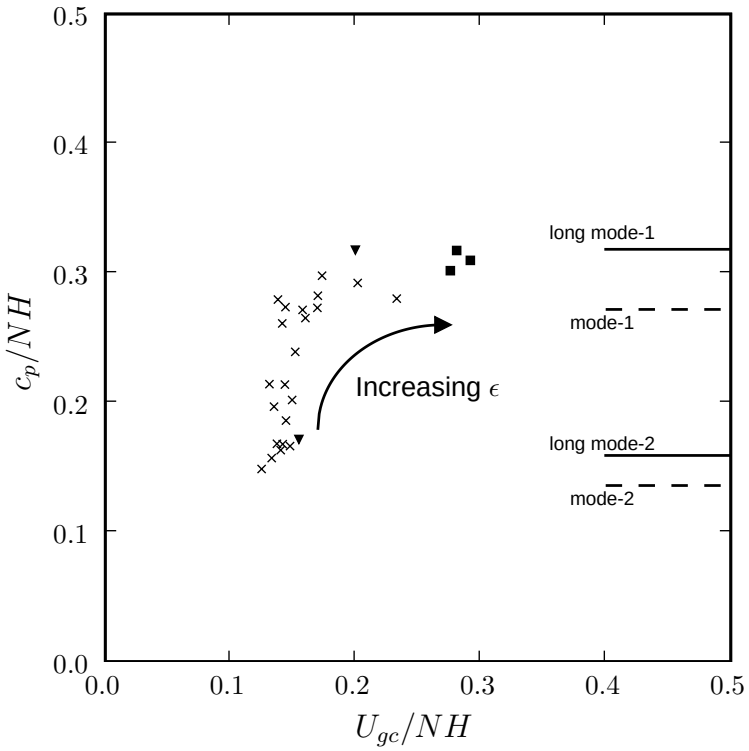

Figure 2.8: Phase speed of the leading internal wave versus intrusion speed. The solid lines (right) give the long wave speeds of mode-1 and mode-2 waves and the dashed lines (right) give the wave speeds of linear waves of mode-1 and mode-2 with frequency $\omega = 0.52N$. Points are plotted as crosses for $\epsilon \leq 0.5$ and $H = 30\,\text{cm}$, as upside-down triangles for $\epsilon \leq 0.5$ and $H = 15\,\text{cm}$, and as solid squares for $\epsilon > 0.5$.

the intrusion head, pinching it into a wedge-shape and causing the intrusion to stop propagating.

The increase in phase speed is due to a change in the structure of the internal waves. There is a transition between internal waves with a mode-2 vertical structure for small values of ϵ to a mode-1 vertical structure for larger values of ϵ. In general, the waves observed in our experiments are a superposition of different wave modes. Nevertheless, the dominant behaviour is characterized by a superposition of mode-1 and mode-2 waves. A long mode-n internal wave has a phase speed given by $c = \frac{NH}{n\pi}$. These phase speeds for long mode-1 and mode-2 waves are superimposed in figure 2.8 as solid lines.

To understand the transition from mode-2 to mode-1, consider an idealized internal wave with normalized vertical displacement given by

$$f(z) = \begin{cases} \sin\left(\frac{\pi(\frac{z}{H}-\frac{1}{2}+\epsilon)}{\frac{1}{2}+\epsilon}\right) & \frac{z}{H} \geq \frac{1}{2}-\epsilon \\ -\frac{\frac{1}{2}-\epsilon}{\frac{1}{2}+\epsilon}\sin\left(\frac{\pi\frac{z}{H}}{\frac{1}{2}-\epsilon}\right) & \frac{z}{H} \leq \frac{1}{2}-\epsilon \end{cases} \tag{2.10}$$

This function was chosen as an approximation to the actual vertical displacements of the dye-line. At the matching point, $z/H = 1/2 - \epsilon$, this function is continuous and has a continuous first derivative. Further justification of this choice of function is given below.

A discrete sine transform was used to compute the amount of relative energy in the first and second modes of the vertical displacements of dye-lines. These energies are plotted against ϵ in figure 2.9. Also plotted is a Fourier sine decomposition of the first two coefficients squared (b_1^2 and b_2^2) of equation (2.10). The typical error bars for the relative wave energy, shown to the right, reflect the coarse determination of the wave amplitudes from a discrete set of dye-lines. Despite these errors, the analytical model and the experimental data confirm that for low values of ϵ, the internal wave is primarily mode-2, as indicated by the fact that the squares (representing the fraction of energy in mode-2 waves) lie above the crosses (representing the fraction of energy in mode-1 waves). For $\epsilon > 0.18$, energy in mode-1 exceeds that in mode-2 waves, and correspondingly the crosses lie above the squares. The analytical model suggests that the mode-1 and mode-2 components account for at least 70% of the total internal wave energy.

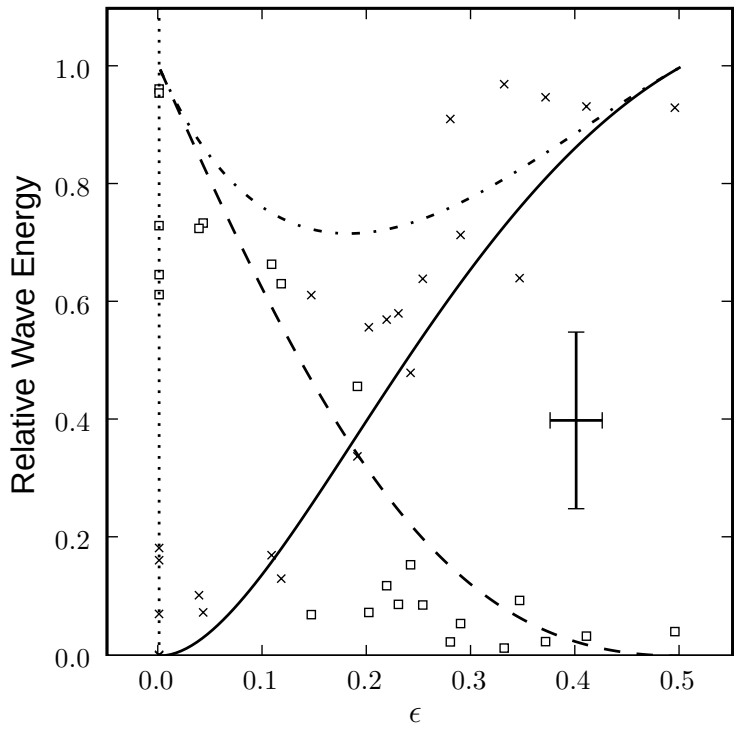

Figure 2.9: Normalized energy of mode-1 (solid line) and mode-2 (dashed line) components versus ϵ for equation (2.10). The dotted-dashed line shows the sum of mode-1 and mode-2 energies. The cross-over point where the mode-1 energy begins to exceed the mode-2 energy occurs at $\epsilon \simeq 0.18$ and the minimum energy captured by the mode-1 and mode-2 components is 0.72. The data points show the relative energy in the mode-1 component (crosses) and in the mode-2 component (squares) as computed from a range of experiments. Typical error bars of the experimental data are indicated to the right.

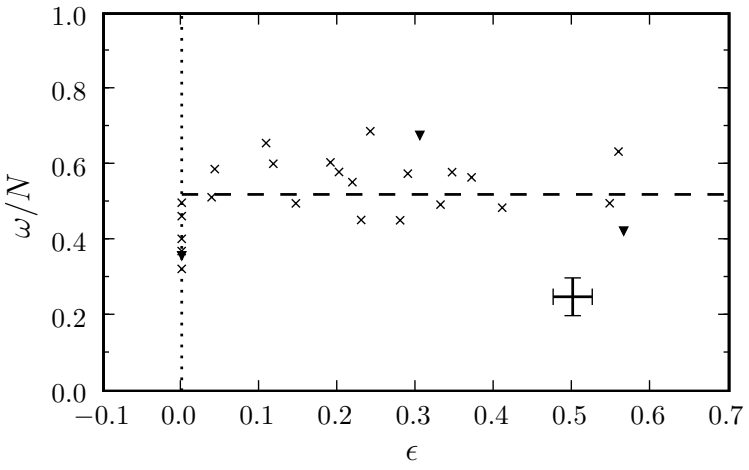

Figure 2.10: Frequency of the internal wave normalized by the buoyancy frequency in experiments with $\ell = 18.5\,\text{cm}$ and $H = 30\,\text{cm}$ (crosses) and $H = 15\,\text{cm}$ (upside-down triangles). The dashed line shows the mean frequency. Typical error bars are indicated.

Thus the intrusion exists in one of three regimes depending upon the value of ϵ. For $\epsilon \simeq 0$, the advance of the intrusion is supercritical to the mode-2 internal waves that are dominantly excited, for $0.18 \lesssim \epsilon \lesssim 0.6$ the intrusion and bottom-propagating gravity currents are subcritical to mode-1 internal waves that are dominantly excited, and for $\epsilon \gtrsim 0.6$ the bottom-propagating gravity currents are supercritical to the mode-1 waves that are dominantly excited.

Figure 2.10 shows that the frequency, ω, of these waves normalized by the buoyancy frequency is independent of ϵ with $\epsilon \neq 0$ and has a mean value of 0.52 and a standard deviation of 0.10 over all experiments. Although one might expect that the collapse of the lock-fluid would generate a spectrum of frequencies, the waves themselves are excited in a narrow frequency band. This frequency selection has been observed in a variety of experiments and simulations in which waves were generated by grid-generated turbulence (Dohan and Sutherland, 2002, 2003), turbulence resulting from flow over rough topography (Aguilar and Sutherland, 2006), and from an intrusion at the interface of a uniform density fluid and a uniformly stratified fluid (Flynn and Sutherland, 2004).

Because ω is comparable to N, the waves cannot be treated as long. The phase speed of a mode-n internal wave of frequency ω is given by $c = \frac{H}{n\pi}\sqrt{N^2 - \omega^2}$.

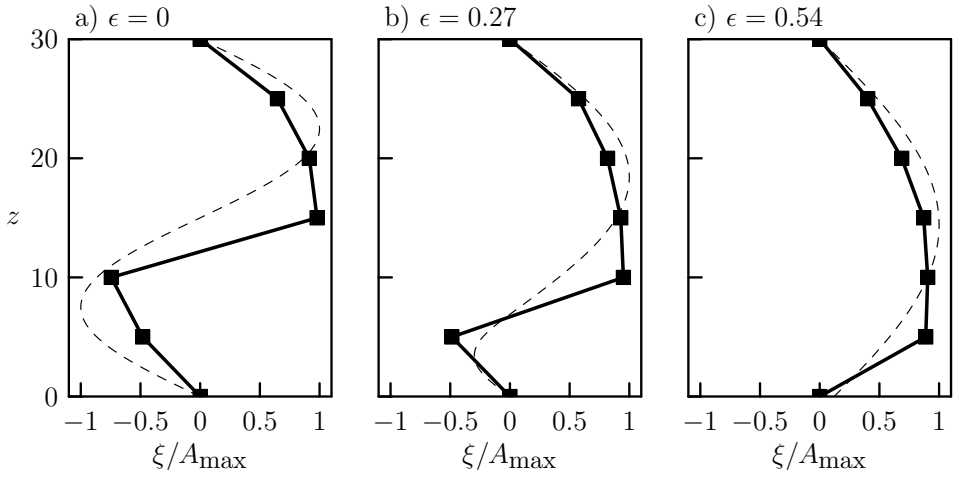

Figure 2.11: Normalized maximum vertical displacement of dye-lines as function of height taken at $x = 60$ cm and computed over first wave period. The dotted lines show equation (2.10) plotted for the corresponding value of ϵ with (a) $\epsilon = 0$ (b) $\epsilon = 0.27$ (c) $\epsilon = 0.54$.

Since we found on average $\omega = 0.52N$, we can compute the speed of a typical mode-1 and mode-2 wave. These speeds are plotted as dashed lines on figure 2.8. These phase speeds underestimate the phase speeds observed in our experiments. The fact that the observed phase speeds are larger than linear theory predicts indicates the waves are nonlinear.

Figure 2.11 shows vertical profiles of the maximum vertical displacement of the ambient measured in three experiments from vertical time series examining the displacement of 5 dye lines at $x = 60$ cm. This distance, a little more than 2 lock-lengths from the gate, is chosen to be sufficiently close to the lock that reflecting waves from the lock-end of the tank do not interact with the intrusion head as it passes this position. The dashed lines in the figure show amplitude profiles using equation (2.10) overlaid on measurements taken from three sample experiments. The three profiles, which correspond to the experiments with snapshots shown in figures 2.3, 2.5 and 2.6, clearly reveal displacements with a mode-2 shape if $\epsilon = 0$ (figure 2.11a), a mixed mode-1 and mode-2 shape if $\epsilon = 0.27$ (figure 2.11b), and a mode-1 shape if $\epsilon = 0.54$ (figure 2.11c).

From the amplitude, frequency and vertical mode structure of the waves, we estimate the energy associated with waves in the ambient during the slumping-phase

of the intrusion. Defining the vertical displacement amplitude, A_ξ, to be the largest displacement of the set of the five dye-lines, the energy density per unit mass is given by

$$< E_{\text{wave}} >= \frac{1}{2} N^2 {A_\xi}^2. \tag{2.11}$$

The energy per unit tank-width associated with the ambient is then estimated by multiplying the energy density by the area

$$\mathcal{A}_{\text{wave}} = \begin{cases} (1+2|\epsilon|)\ell H & |\epsilon| < 1/2 \\ 2\ell H & |\epsilon| \geq 1/2. \end{cases} \tag{2.12}$$

Here the horizontal length-scale is assumed to increase in proportion to ϵ as the waves evolve from having a mode-2 to a mode-1 structure. This is consistent with the observation that the frequency is fixed but the vertical scale doubles as ϵ increases from 0 to $1/2$.

The resulting energy is compared with the available potential energy per unit width of the fluid in the tank before the gate is extracted. This is calculated as the difference between the potential energy of the initial state and the final state that would occur in the absence of mixing:

$$\text{APE}_0 = \int_0^L \int_0^H g\left(\rho_{\text{initial}}(x,z) - \rho_{\text{final}}(z)\right) z dz dx \tag{2.13}$$

In the initial configuration, homogeneous fluid of density ρ_ℓ resides in a lock of length ℓ beside the uniformly stratified ambient of length $L-\ell$, as shown in figure 2.1. Explicitly, the density structure is given by

$$\rho_{\text{initial}}(x,z) = \begin{cases} \rho_\ell & 0 < x < \ell \\ \rho_B + (\rho_T - \rho_B)\frac{z}{H} & \ell < x < L. \end{cases} \tag{2.14}$$

Assuming no mixing occurs, the final state is that of a piecewise-uniform stratified fluid with a horizontal slab of fluid of density ρ_ℓ occupying the full length L of the tank about the neutrally buoyant depth of the ambient before the experiment begins. (See figure 2.3d). From conservation of mass of the lock- and ambient-fluid, this final density profile is given by

$$\rho_{\text{final}}(z) = \begin{cases} \rho_\ell + (\rho_T - \rho_\ell)\frac{z-h_0}{H-h_0} & h_0 < z < H \\ \rho_\ell & h_1 < z < h_0 \\ \rho_B + (\rho_\ell - \rho_B)\frac{z}{h_1} & 0 < z < h_1. \end{cases} \tag{2.15}$$

If $\rho_\ell < \rho_B$, then

$$h_1 = \frac{\rho_\ell - \rho_B}{\rho_T - \rho_B} H \frac{L-\ell}{L} \text{ and } h_0 = h_1 + H\frac{\ell}{L}.$$

Otherwise, if $\rho_\ell > \rho_B$, then $h_1 = 0$ and $h_0 = H\ell/L$. The available potential energy per unit width is thus given by

$$\text{APE}_0 = \frac{1}{24}\rho_0 \left(1 - \frac{\ell}{L}\right) \ell H^3 N^2 \begin{cases} 12\epsilon^2 + 1 & |\epsilon| < 1/2 \\ 12|\epsilon| - 2 & |\epsilon| > 1/2, \end{cases} \tag{2.16}$$

which increases with the absolute value of ϵ and with the strength of the stratification.

Using (2.16) to normalize the energy associated with waves given by (2.11) and (2.12), we compute the relative percentage of energy and plot this against ϵ in figure 2.12. The internal waves generated by the release of the lock-fluid accounted for between 7% and 22% of the available potential energy in the system over 25 experiments where the vertical displacements were measured. This is smaller than the 36% of energy determined by Ungarish and Huppert (2006) for the case $\epsilon = 1/2$ in part because we make a conservative estimate of the wave energy based upon the one wavelength of the disturbance determined by the lock-length and the wave-mode, the latter which depends upon ϵ. The relative energy is larger between $\epsilon = 0.1$ and 0.5, corresponding to the cases in which the intrusion stopped before reaching the end of the tank. This analysis demonstrates that a significant enough amount of the available potential energy goes into internal waves and this energy transfer, as a result, significantly influences the dynamics of an intrusion not only at long times but also during the initial stages of its evolution.

2.3.3 Wave amplitudes and energy

To illustrate this impact, we assume the depth-relative amplitude of the waves increases linearly with ϵ until this parameter exceeds $1/2$. Thereafter the amplitude is assumed to be constant. By symmetry, we expect the relative amplitude to double as ϵ increases from 0 to $1/2$. Therefore, we have

$$A_\xi/H = \begin{cases} \alpha(1/2 + |\epsilon|) & |\epsilon| \le 1/2 \\ \alpha & |\epsilon| > 1/2 \end{cases} \tag{2.17}$$

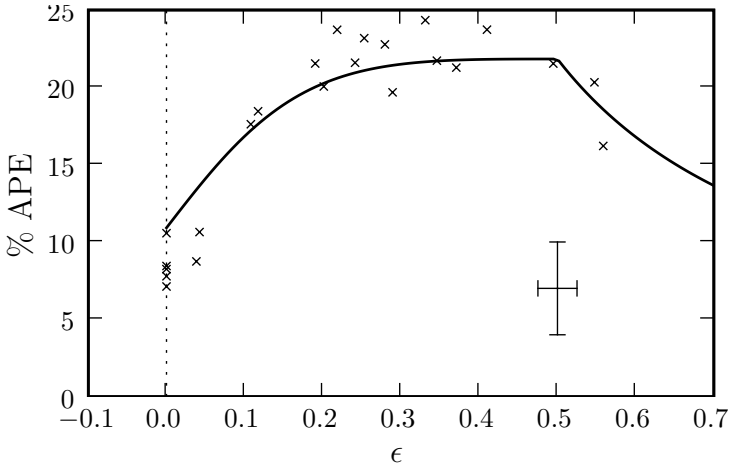

Figure 2.12: Total energy associated with internal waves, shown as a fraction of the initial total available potential energy of the system and plotted versus ϵ. The solid line shows an empirically determined curve using (2.11), (2.12) and (2.16) which is fit to the data using $\alpha = 0.18$. Typical error bars are indicated.

Using this formula, we compute the associated energy of the waves over a volume given by (2.12) and empirically determine the value of α that fits the observed data. Explicitly, we find $\alpha = 0.18 \pm 0.01$. This implies, in particular, that intrusions with $\epsilon \simeq 0.5$ excite internal waves whose amplitudes are almost one-fifth the tank depth.

The corresponding energy normalized by the initial available potential energy of the system is plotted as the solid line in figure 2.12. Note that the relative energy decreases for $\epsilon > 1/2$ because the energy associated with waves generated by bottom-propagating currents is constant whereas the available potential energy of the system increases with increasing density of the lock fluid.

As the waves change from mode-2 to mode-1, their amplitude and wavelength doubles and so their associated available potential energy increases by a factor of 8. Meanwhile, the available potential energy associated with the lock fluid given by (2.16) increases by a factor 4 as ϵ changes from 0 to $1/2$. Therefore, as expected from symmetry. The percentage change in relative available potential energy is twice as large for mode-1 waves with $\epsilon = 1/2$ as for mode-2 waves with $\epsilon = 0$.

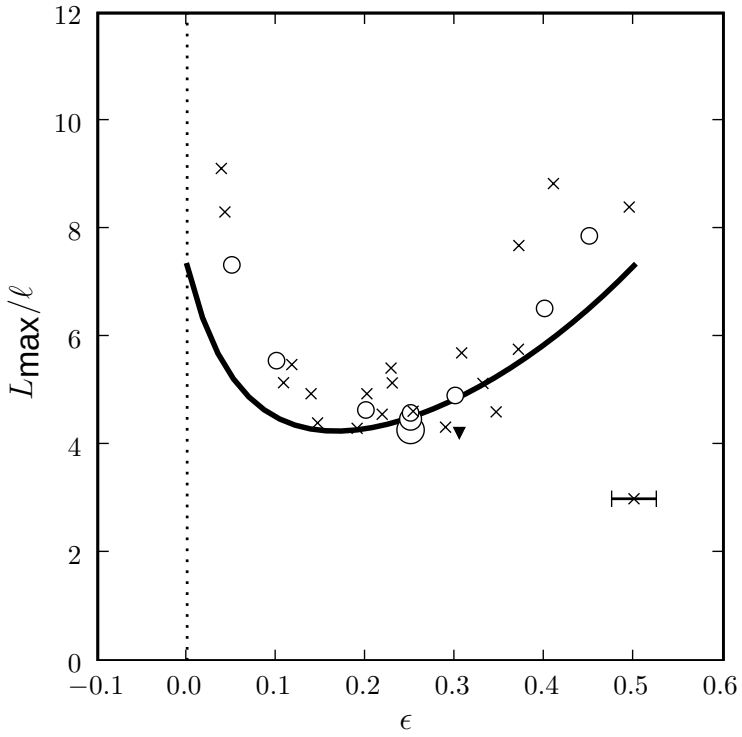

Figure 2.13: Maximum distance travelled by intrusion in experiments with $\ell = 18.5\,\mathrm{cm}$ and $H = 30\,\mathrm{cm}$ (crosses) and $H = 15\,\mathrm{cm}$ (upside-down triangles). The results of numerical simulations are shown by open circles. For these $H = 30\,\mathrm{cm}$. Small, medium and large circles represent the intrusion distances found in simulations with $\ell = 18.6$, 40 and $80\,\mathrm{cm}$, respectively. Typical errors in estimating ϵ in experiments are indicated toward the bottom right-hand side of the plot. Values are plotted only for those experiments in which the intrusion did not interact with the far end of the tank before being stopped by internal waves catching up to the intrusion head from the lock-end of the tank.

2.3.4 Intrusion propagation distance

A universal feature of our experiments is that the intrusions started off at an initially constant speed after a brief acceleration phase. In some cases the intrusion propagated to the end of the tank where it stopped due to the rigid vertical boundary. This occurred either in experiments with $\epsilon \sim 0$ or $\epsilon \gg 1/2$. Otherwise, due to interactions with internal gravity waves, the intrusion stopped abruptly midway along the tank.

Figure 2.13 shows the relative distance the intrusion travelled in units of lock lengths before this stopping first occurred.

Such an interaction between internal waves and subcritical bottom-propagating gravity currents was also observed by Maxworthy et al. (2002). An estimate of the distance over which the the waves interact strongly with the current head was provided by Ungarish and Huppert (2004), who claimed the internal waves were locked with the head over the first two wavelengths of motion. Thereafter the waves "unlocked from the head and moves forward relative to the current until the crest reaches the nose (and thus slows it down)". Our intrusion experiments demonstrate a different interaction mechanism. As shown, for example, in Figure 2.2a, we find the waves are not locked with the head but advance at constant speed toward the intrusion head after reflecting from the lock-end of the tank. The current does not slow down after interacting, but stops abruptly. Stopping occurs if the intrusion speed is slower than the internal wave speed.

The speed of both waves and intrusions depends upon the value of ϵ. If $\epsilon \sim 0$ the intrusion speed is comparable to the mode-2 internal wave speed. If $\epsilon \gg 1/2$, the bottom-propagating gravity current propagates at speeds comparable to or faster than the mode-1 internal wave speed. In both circumstances the intrusion is supercritical and so waves reflecting from the lock-end of the tank do not catch up with the intrusion head.

At intermediate values of ϵ, the return flow into the lock excites internal waves that reflect off the lock-end of the tank and then propagate toward the intrusion head at a faster speed than the intrusion itself: the intrusion is subcritical. The advance of the intrusion stops when the waves catch up with the head. This occurs on a time scale which, for fixed N and H, depends upon the mode number (depending upon ϵ) and the lock length.

We estimate the stopping distance of intrusions from the time taken for internal waves generated in the return flow to reflect off the lock-wall of the tank and then catch up to the intrusion head. We crudely estimate the speed of these waves to be given by

$$c = \frac{NH}{\pi}(1/2 + |\epsilon|) \quad |\epsilon| \leq 1/2. \tag{2.18}$$

This corresponds to a linear increase in the phase speed from that of mode-2 to mode-1 waves as ϵ increases from 0 to 0.5. The relative distance from the gate that

a subcritical intrusion moving at speed U_{gc} travels before internal waves at speed $c > U_{\mathrm{gc}}$ catch up to it is

$$\frac{L_{\mathrm{max}}}{\ell} = \frac{2U_{\mathrm{gc}}}{c - U_{\mathrm{gc}}}. \tag{2.19}$$

Using (2.8) and (2.18) gives the solid curve plotted in figure 2.13. This estimate agrees well with the observed stopping distance of the intrusion.

2.4 Discussion and conclusions

Experiments have investigated intrusions and their interactions with internal waves in a uniformly stratified ambient.

Two-dimensional numerical simulations of this laboratory experiment (described and analyzed in Munroe et al. (2009)) capture the observed structure and speed of the intrusions which indicates that their macroscopic dynamics can be well described by a two-dimensional model.

The speed of the intrusion was found to match the prediction of Bolster et al. (2008) in circumstances with $\epsilon < 0.5$. For $\epsilon > 0.5$, the theoretical prediction of Ungarish and Huppert (2002) and the empirical prediction of Maxworthy et al. (2002) is close to the observed speed of bottom-propagating gravity currents, though theory moderately underpredicts the speed.

It is well-established that a gravity current in a uniform-density ambient propagates 6 to 10 lock-lengths before entering the 'self-similar' phase in which the current decelerates. This occurs because the finite volume of lock-fluid requires the head-height to decrease and, consequently, the horizontal pressure gradient force driving the current decreases. Our results show this does not occur for intrusions released into a uniformly stratified ambient from a high aspect-ratio lock. Internal waves interacting with the intrusion head dominate the long-time evolution of the intrusion. In symmetric cases, the waves propagate at the same speed as the intrusion and carry the lock-fluid at constant speed well past 10 lock lengths, even though the vertical extent of the head decreases substantially. In asymmetric cases, waves that reflect from the lock-end of the tank catch up with the head and halt its advance. Thereafter, the lock-fluid slowly undulates forward driven dominantly by

the wave field and not by horizontal pressure gradients established through horizontal density changes between the intrusion and ambient.

The distance travelled by the intrusion before stopping is related to the wave speed of the internal waves generated. Intrusions travelling near the mid-depth of the tank excite mode-2 waves. In the limit of an intrusion becoming a gravity current, more mode-1-like waves are produced. Mode-1 waves travel faster than mode-2 waves and faster than the intrusion for intermediate values of ϵ. The mode-1 waves, which reflect off the rear wall of the tank and then catch up with the intrusion head, cause the intrusion to stop before hitting the end of the tank. The energy associated with the waves lies between 10 and 20% of the initial available potential energy of the lock-fluid. This may not be so large as to have a leading order effect upon the intrusion speed, but it is large enough to affect non-negligibly the consequent evolution of the intrusion in terms of the propagation distance.

Energy analyses of intrusions in the supplementary numerical simulations (Munroe et al. (2009)) show that a substantial fraction of the initial available potential energy is transferred to the ambient if ϵ is sufficiently larger than zero and mode-1 waves are predominately excited.

Experimental data were used to derive an empirical formula for the wave energy. This result showed that, for bottom-propagating gravity currents, the energy of waves relative to the initial available potential energy decreases as ϵ increases. These results are consistent with the observation that internal waves do not strongly influence the consequent motion of the current if ϵ is large.

In none of the experiments performed did we observe the transition from steady-state to self-similar propagation of the intrusion, as predicted by Ungarish (2005). The symmetric intrusion propagates beyond 10 lock lengths without deceleration. Indeed, Sutherland and Nault (2007) have shown that symmetric intrusions can propagate up to 22 lock-lengths without decelerating as a result of coupling with mode-2 internal waves. The long-time evolution in this case is best described by the propagation of closed core solitary waves. Asymmetric intrusions with $0.18 \lesssim \epsilon < 0.5$ propagate at constant speed until suddenly stopping due to interaction with internal waves.

Some signature of a self-similar phase seemed to occur in experiments by Wu (1969) and Amen and Maxworthy (1980), consistent with shallow water predictions (Ungarish (2005)). So why was the self-similar phase not observed in our experiments? A likely explanation is that those experiments generated symmetric intrusions from the collapse of a mixed region that did not extend over the full depth of the tank, a circumstance that is better described by the approximations of shallow water theory. Thus it seems in those circumstances that the collapsing mixed fluid did not excite such large amplitude internal waves and that the fluid became sufficiently diluted through mixing with the ambient that its advance slowed. Clearly more experiments on partial-depth mixed region collapse should be performed to examine this circumstance in more detail.

In order to focus upon the interactions between intrusions and internal waves, our laboratory experiments were confined to the examination of relatively short locks compared to the length of the tank. In longer tanks with longer locks a proportionally smaller volume of the intrusion would mix with the ambient. In these circumstances it may be that asymmetric intrusions would evolve into a self-similar phase before interacting with internal waves reflecting from the lock-end of the tank (Paul F. Linden, private communication). Nonetheless, we have seen that symmetric intrusions (with $\epsilon = 0$) propagate over 10 lock-lengths without decelerating all the while with the head-height decreasing. Internal waves locked to the intrusion head, not horizontal density gradients between the intrusion and ambient, are responsible for the transport at constant speed. Likewise, in asymmetric circumstances the intrusion stops due to interactions with internal waves and thereafter the transport of lock-fluid is governed primarily by the waves, not horizontal density gradients. In general, the experimental results show that the long-time evolution of intrusions in uniformly stratified fluid is not necessarily well modelled by a straightforward adaptation of Benjamin's theory that neglects the generation and consequent influence of internal waves upon the flow.

Chapter 3

Forcing by Turbulence near Rough Isolated Topography

The content of this chapter was previously published in the journal *Environmental Fluid Mechanics* as Munroe and Sutherland (2008).

3.1 Introduction

In this chapter, we examine the generation of internal gravity waves by a moving source of turbulence. We have reused the apparatus of the towed topography of Aguilar and Sutherland (2006) but changed the stratification. In our experiments, internal waves in a linearly stratified layer are forced from above by sheared turbulence in a uniform density layer. Thus, we can compare the effect of a moving source of turbulence in a fully stratified fluid, the case presented by Aguilar and Sutherland (2006), to a stratified fluid with a well-mixed upper layer, the case investigated here. Since the physical application of this work is to the turbulence from wind driven eddies in the ocean mixed layer it is more reasonable to use this shear turbulence apparatus as opposed to a grid generated stationary turbulence setup (Dohan and Sutherland (2005)). Note that the focus of the present study is not on topographically generated waves, although the apparatus has been used previously for that purpose. Rather, we are looking at waves launched by turbulent eddies. We view the 'rough topography' acting as an eddy generator due to boundary layer separation and its turbulent wake. We show that for our surface mixed case the generated internal waves have frequencies, as expected, in a narrow range of a fixed

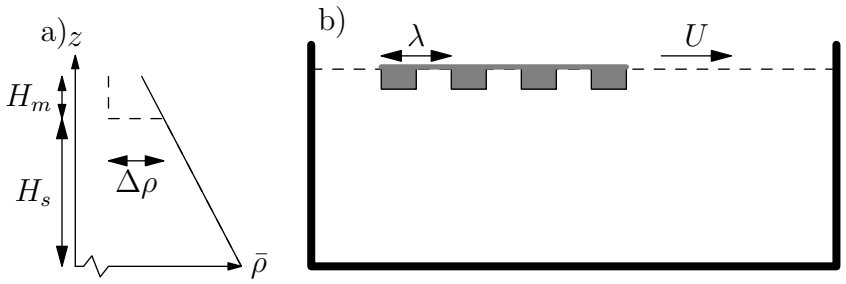

Figure 3.1: a) Typical stratifications. The solid line shows the density profile of the uniform stratification experiments. The dashed line shows the density profile of the surface mixed layer experiments. b) Setup of apparatus.

factor of the buoyancy frequency.

3.2 Setup and methods

We performed our experiments in a 197.1 cm long glass tank that is 48.5 cm deep and 17.4 cm wide. A linearly stratified fluid was created in the tank using the standard 'double bucket' technique (Oster (1965)) to a total depth $H = 27$ cm. The typical buoyancy frequency for all experiments in the stratified lower region was $N \approx 1.1$ s^{-1}. The density was measured using a Standard Precision Conductivity Probe set up to traverse the entire depth of the fluid. This was the stratification used for uniformly stratified experiments and is sketched by the solid line in Figure 3.1a. For the surface mixed layer experiments, approximately 5 cm of the fluid was siphoned off and was replaced with an equal volume of fresh water, $\rho_m = 1.0$ g cm^{-3}. This created a density profile as sketched in Figure 3.1a using a dashed line. After repeated experiments this mixed region may deepen to approximately 7 cm. A wooden square waveform of the same width as the tank, with peak-to-peak height 2.7 cm and wavelength $\lambda = 13.7$ cm is towed at a constant speed using a pulley system along the top of the tank as shown in Figure 3.1b. The topographic wave number is $k = 2\pi/\lambda = 0.46$ cm^{-1}.

The goal of this apparatus is to produce a moving patch of turbulent eddies in a mixed layer and then observe internal waves generated in the linearly stratified ambient beneath. The rectangular waveform acts as an eddy generator as fluid

separates off the sharp corners and produces vortices. The waveform, which is pulled from left to right, is connected to a motor such that the towing speed is in the range $U = 0.8$ cm s^{-1} to 5.0 cm s^{-1} to within ± 0.05 cm s^{-1}. Using a characteristic horizontal length scale of the towed object, $L = 14$ cm, and the viscosity of water, $\nu = 0.01$ cm^2/s we calculate a Reynolds number of Re $= UL/\nu$ as ranging from Re $= 1100$ to 7000. With this range of Reynolds numbers we expect to see flow separation and eddies form in the lee of the topography. The waveform, which floats on the surface, is weighted such that the troughs are at the waterline. Different towing speeds excite eddies of different dominant frequencies, namely $\omega_{\text{exc}} = Uk$. It is natural to form a Froude number, Fr $= Uk/N = \omega_{\text{exc}}/N$ to characterize the towing speed and hence the excitation frequency.

The turbulence in the lee of the towed object can be characterized using particle image velocimetry (Fincham and Delerce (2000)). Figure 3.2 shows some details of the structure of the forcing velocity field for the case with a mixed layer. The upper frame shows a typical vector plot of the velocity field obtained in the lee of the towed object as a time series. From this time series, it can be seen that the integral length scale of the dominant eddies is about 6 cm which is the same as the thickness of the mixed layer. The integral time scale is approximately 5 seconds. The lower frame shows the energy density in the mixed layer as a function of time for three independent experiments.

The turbulent eddies impinge upon the stratified region to force internal waves. The internal waves are measured using synthetic schlieren (Sutherland et al. (1999)). This optical technique takes advantage of the variation of index of refraction of light as a function of density and allows us to measure non-intrusively the frequency, wave numbers, and amplitudes of the internal waves.

Figure 3.3 shows images produced using synthetic schlieren taken from typical experiments. The field shown is N_t^2 which is proportional to the vertical displacement of the fluid. Although the entire length of the tank is almost 2 m, the camera's field of view is only 27.5 cm wide by 20 cm high. We define a world coordinate system where $x = 0$ cm corresponds to the left edge of the field of view and $z = 0$ cm is the surface. In this region of interest, located at the middle of the tank, we assume

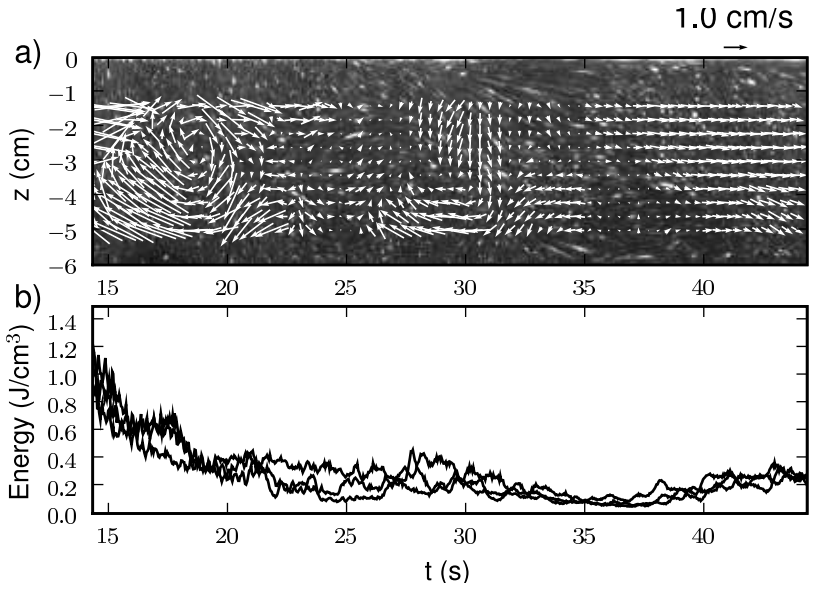

Figure 3.2: The lee of the towed object for Fr $= 1.46$ showing a) velocity field as a vertical time series and b) the energy density of the mixed layer as a function of time for three separate runs of the experiment.

the end walls of the tank are far enough away that reflection of waves is unimportant. Reflection of waves off the bottom of the tank still occurs. Figure 3.3a,c,d shows an experiment with Fr $= 0.53 < 1$. This is a sub-critical experiment since the forcing frequency is less than the buoyancy frequency. Figure 3.3b,d,e shows an experiment with Fr $= 1.73 > 1$. This is a super-critical experiment since the forcing frequency is greater than the buoyancy frequency. Vertical (Figure 3.3a,b) and horizontal (Figure 3.3c,d) time series show how the waves in these two cases are generated and propagate over time. In the vertical time series taken at $x = 13.7$ cm, which is halfway through the field of view, we can see that there is not much signal directly over the topography. In the wake of the topography, where there is more turbulence visible, strong vertically propagating waves can be seen. On the upper axis is the equivalent horizontal spatial scale defined as taking time and multiplying by the towing speed. It is difficult to isolate individual waves in a vertical time series since waves generated at different times are visible in the same image. However, using a horizontal time series, taken at $z = -15$ cm, it is much clearer to see waves produced at the same time.

The window selected in time for the time series ranges from $t = 0$ s to $t = 60$ s.

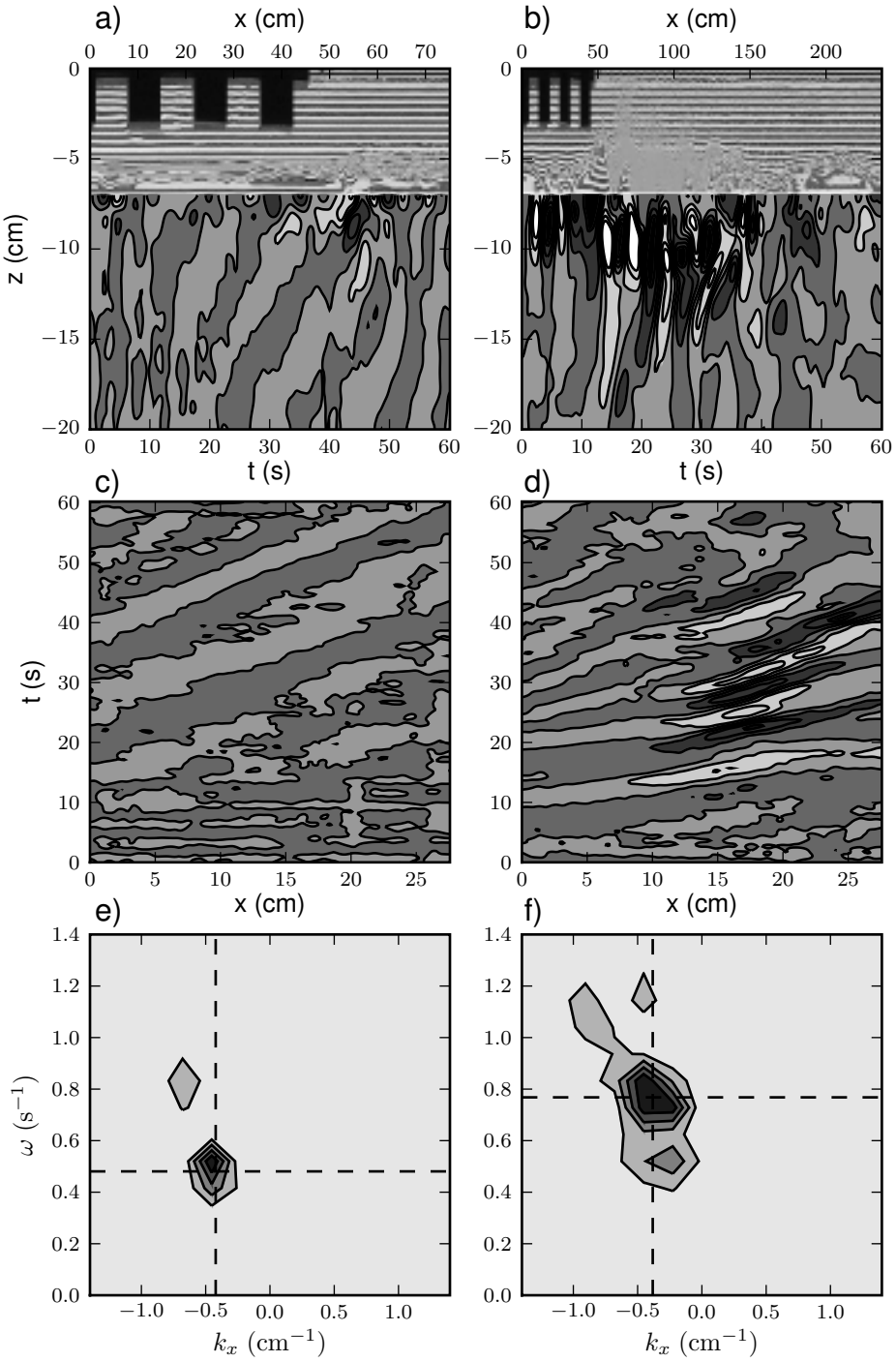

Figure 3.3: Turbulently generated internal waves shown using a) vertical time series at $x = 13.7$ cm with the equivalent horizontal scale ($x = |U|t$) shown in the top axis, c) horizontal time series at $z = -15$ cm, and e) power spectrum of the horizontal time series for an experiment with Fr $= 0.53$. b), d), f) are respectively the same but for Fr $= 1.73$. Contours in a-d) are plotted at values between -0.15 and 0.15 s^{-3} spaced by 0.10 s^{-3}. The spectra are normalized to have maximum value of unity.

Here, $t = 0$ s is defined as the time at which the waveform started moving. The frequency and the wave number of the internal waves were calculated using a discrete Fourier transform. Examples of power spectra measured are given in Figure 3.3e, f. Note that the resolution is proportional to the inverse of the domain of our field of view and can not easily be improved without using a larger tank and apparatus. We estimated the location of the peak and the error using a Gaussian best fit. The largest peak is indicated by the intersection of dashed lines. The width of Gaussian fit gives the standard deviation in the error which is typically 10% of the frequency measurement. Comparing the different experiments, the spectra are noticeably broader for super-critical forcing than for sub-critical forcing. As can been seen in Figure 3.3e, there may be more than one peak in the power spectrum. Being more restrictive in choosing the window in time on a per-experiment basis could be done to isolate waves generated directly beneath the topography from those generated by the lee of the topography. Reducing the length of the window in time, however, reduces the resolution in determining the frequency. We define the dominant wave frequency as the frequency associated with the largest peak in the power spectrum and hence the waves with the largest energy. The consistent approach of using a window in time with a fixed length was applied to all experiments.

3.3 Analysis and results

Figure 3.4 shows the relative wave frequency, ω/N, as a function of the forcing frequency expressed as a Froude number, Fr $= Uk/N$. The plotted values are the means of dominant frequencies determined according to the method in the previous section for each of three horizontal time series at $z = -13, -15$, and -17 cm. The error bars are the standard error in the mean for each experiment. The dotted line shows $\omega = N\text{Fr} = \omega_{\text{exc}}$, which is the wave frequency predicted by linear theory for flow over sinusoidal hills. The vertical dashed line indicates the boundary between sub-critical, $\omega_{\text{exc}} < N$ and super-critical, $\omega_{\text{exc}} > N$.

A series of 12 experiments using a uniform stratification over the entire depth (Aguilar and Sutherland (2006)) is given in Figure 3.4a. When Fr < 0.7, topo-

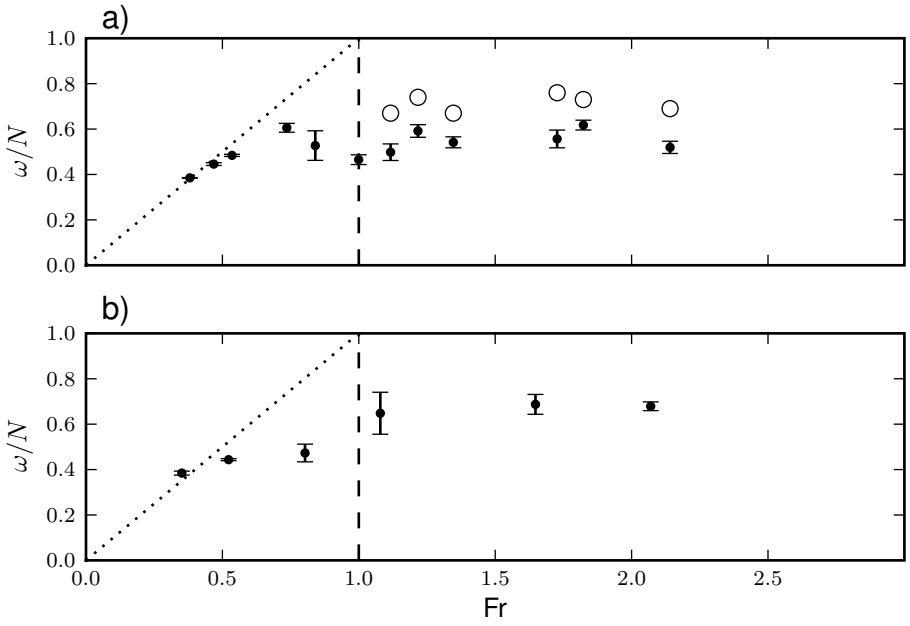

Figure 3.4: Plot of measured dominant relative internal wave frequency, ω/N, as a function of Fr $= \omega_{\text{exc}}/N$ for a) uniformly stratified experiments and b) surface mixed layer experiments. The open circles in a) are waves generated in the far lee by turbulence only.

graphically generated waves with the same frequency as the forcing frequency are observed as the dominant signal. In the super-critical region, the dominant wave frequency is independent of Fr and has a mean value of 0.55 ± 0.04. It is known from previous work (Aguilar and Sutherland (2006)) that this frequency corresponds to internal waves generated in the near lee of the towed topography. The near lee is characterized by an undulating "boundary-trapped lee wave" which acts as a source of internal waves. Waves generated by turbulence in the far lee are distinguished from orographic- and lee-generated waves by separation in time. In the far lee, defined as beyond two buoyancy periods after the trailing edge of the topography has passed, the flow is much less coherent and more turbulent. The open circles in Figure 3.4a correspond to horizontal time series being windowed in time such that only information from the far lee is included. The waves here have a mean frequency of 0.71 ± 0.09.

We can compare these uniform stratified experiments with our surface mixed experiments to determine the importance of the turbulent forcing being located in a

mixed layer as opposed to a stratified layer. The relative wave frequency, as shown in Figure 3.4b, increases until Fr ≈ 0.7. In the super-critical region, the wave frequency is independent of Fr and has a mean value is 0.69 ± 0.03. This is the same as the frequency observed in the far lee of the uniformly stratified experiments. Note that in this case no windowing in time has been used to differentiate the near lee versus far lee. This suggests that the dominant frequency observed is due to waves generated by shear turbulence. Towing rough topography through a mixed layer precludes the development of a boundary-trapped lee wave and leaves only the turbulence in the wake as a source for internal wave generation. The horizontal wave number is a constant for all experiments.

This wave number, $|k_x| = 0.46$ cm^{-1} is coincidentally the same as the wave number given by the periodicity of the rectangular topography. However, length scales of topographic amplitude and wave length and mixed layer depth are all similar for these experiment so it not clear what sets the horizontal length scale of the waves. From other experiments performed (not shown) using a towed plate with an effective wavelength of $\lambda = 0$ cm and the same amplitude as the rectangular topography we have observed generated waves have the same horizontal length scale and frequency but much larger amplitude.

Further experiments to distinguish which length scale sets the length scale of the dominant eddies of turbulence in the lee and thus the length scale of the internal waves is on-going. The results presented here show that the frequency of the waves depends weakly on the thickness of the mixed layer.

The amplitude of the waves, computed as the root mean square of the horizontal time series, increases with towing speed. The dependence seems to be a fractional power law and further analysis is currently being performed. The wave amplitude also depends on the topographic amplitude (Aguilar and Sutherland (2006)) and may depend on the thickness of the mixed layer.

3.4 Discussion and conclusions

Experiments with a surface mixed layer above uniformly stratified fluid demonstrate that the frequency of turbulently generated internal waves occur in a narrow band around a fixed fraction of the buoyancy frequency.

The observation that the wave frequency matches the forcing frequency up until Fr $\simeq 0.7$ and then remains roughly constant at $\omega/N \simeq 0.7$ is consistent with previous experimental studies of turbulence generated internal waves (Aguilar and Sutherland (2006); Dohan and Sutherland (2005)). It has been suggested by Dohan and Sutherland (2005) that waves of this frequency are dominant because waves with $\omega/N = 1/\sqrt{2} \simeq 0.71$ are the ones that have the maximum vertical flux of horizontal momentum and thus there is an interaction between the wave field and the turbulent region which excite waves close to this frequency. Another explanation is proposed by Taylor and Sarkar (2007) where it is suggested that waves of this frequency endure the least amount of viscous damping and thus are the dominant waves observed.

Internal waves from both sheared turbulence, such as in this experiment, and stationary turbulence, such as the the experiments by Dohan and Sutherland (2005) are observed to have the same characteristic frequencies. From observations in Dohan and Sutherland (2005), a broad range of turbulent eddies with different characteristic velocity and length scales generates a relatively narrow band of internal waves in terms of frequency and length scales. This suggests the properties of these turbulence generated waves are universal and independent of the forcing mechanism.

3.5 Afterword

This experimental apparatus was originally intended to explore the generation of internal waves by sheared turbulence. Further analysis showed that although there was a turbulent wake and internal waves were observed to be generated, it was impossible to identify only the waves forced directly by the turbulence. When the towed waveform is stopped before it reaches the end of the tank, the fluid that had been pushed ahead of the topography is forced to run under the waveform. This

displacement of stratified fluid is an additional source of internal waves.

Since the turbulently generated waves are only forced while the topography is in motion, the waves are transient and it is difficult to use Fourier-transformed time series to analyze the wave properties.

For these two reasons, a new experimental apparatus involving a conveyor belt forcing the surface the fluid was designed to study internal waves generated by sheared turbulence. This is the focus of chapter 4.

Chapter 4

Conveyor Belt Driven Flow

The primary focus of the research in this thesis is the amount of energy transferred to internal waves by a turbulent mixed region. As was mentioned in the previous chapter, the towed topography experiments do not appropriately model a sustained sheared turbulent flow forcing internal waves in a stratified ambient fluid. The experiment was redesigned to resemble more directly the physical scenario of wind stress on the surface of a stratified ocean. In particular, a conveyor belt was set up to drag the surface fluid thus imparting a shear stress to the fluid. The fluid was initially linearly stratified as it was hypothesized that a turbulent mixed layer would develop near the belt and internal waves would be observed propagating away from the mixed region.

The chapter is organized as follows. In section 4.1 a description of the experimental apparatus and setup is presented. In section 4.2, results about the deepening rate of the mixed layer are shown. In sections 4.3 and 4.4 analysis of the wave properties and turbulence properties are given, respectively. Section 4.5 combines these results to give a prediction of waves based on the turbulent description. Finally, in section 4.6, we conclude with future work and suggest methods to test our predictions.

4.1 Apparatus

These experiments are conducted in an acrylic tank with length 47.6 cm, width 9.7 cm, and height 50.0 cm as shown in figure 4.1. The wall thickness is 0.8 cm.

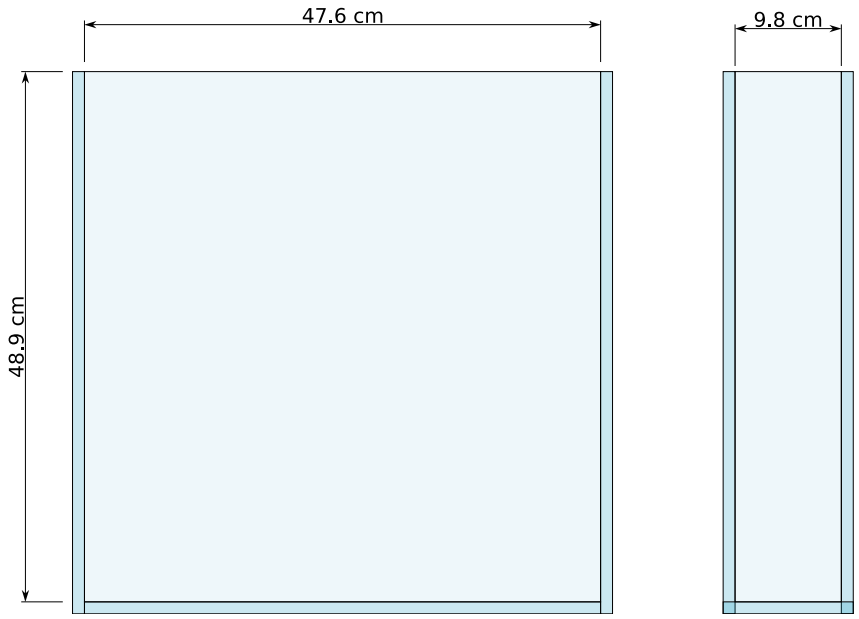

Figure 4.1: Front and side view of tank showing dimensions.

This tank is only a quarter of the length and half as wide as the towed topography tank described in chapter 3.

A conveyor belt at the surface drives the flow in the tank. The support structure for the conveyor built was prototyped using Lego Technic/Mindstorms sets, shown with a computer rendering in figure 4.2, and it was determined that this prototype worked sufficiently well that useful data could be collected. That data is presented here. A photograph of the conveyor belt apparatus in the tank is shown in figure 4.3.

In the broadest sense, this experiment mimics wind blowing across the surface of the ocean. Although not attempting to replicate the full-scale dynamics, an apparatus has been developed that physically models the phenomena of turbulently generated waves by wind driven turbulence in the ocean mixed layer. The setup is shown schematically in figure 4.4. A variable-speed conveyor belt is half-way submerged in a tank of salt-stratified fluid. The conveyor belt is 8 cm wide and has a distance 40 cm between the two wheels. The radius of the wheels is $r = 2.5$ cm. The belt is made of flexible rubber with plastic plates every 2 cm. The plates span the width of the belt, have height of 0.4 cm, and a thickness of 0.1 cm. The purpose

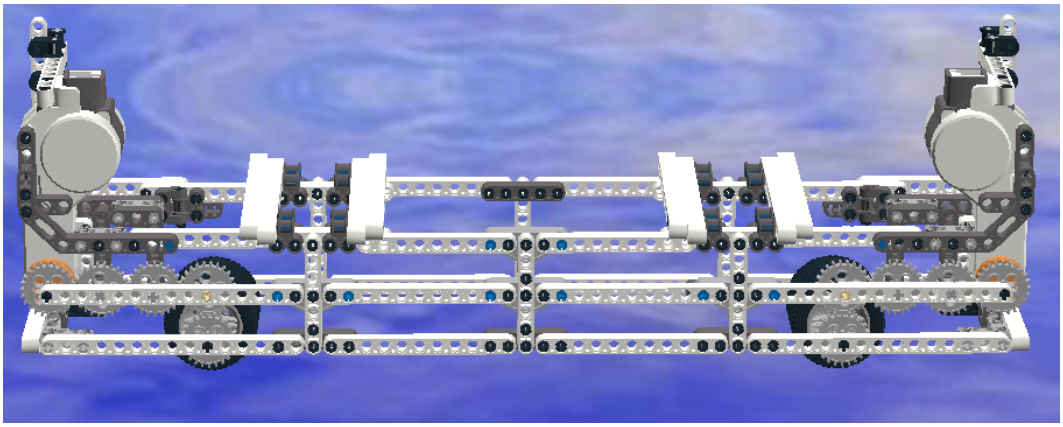

Figure 4.2: Computer rendering of conveyor belt apparatus.

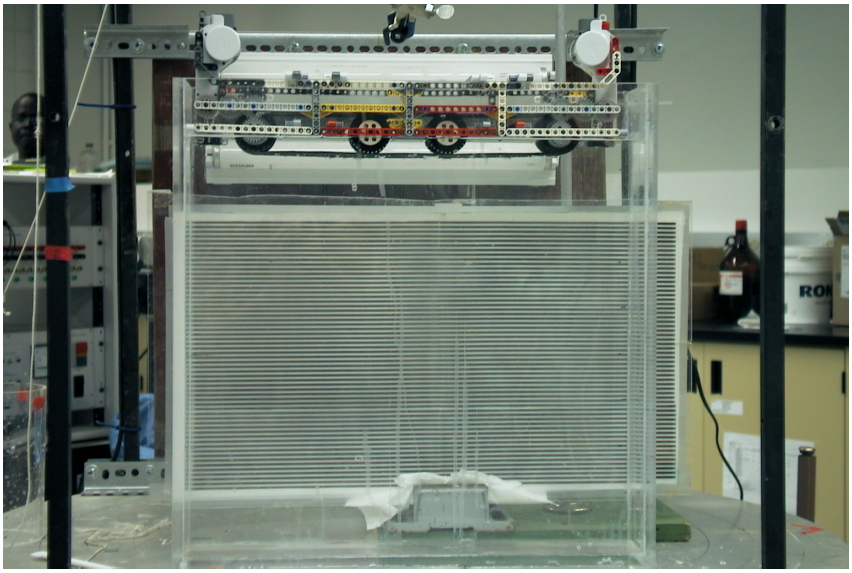

Figure 4.3: Photograph of conveyor belt and tank. The conveyor belt structure rests on the top of the tank. A screen of black and white lines and a bank florescent lights are positioned behind the tank to be used to visualize the internal waves using synthetic schlieren.

of the plates is to increase the drag of the belt on the fluid. The belt is usually immersed in the fluid such that the center of the driving wheels are at the water line. Each driving wheel is connected via gears to a computer controlled servo motor which is synchronized to move at the same speed. The belt moves in a counter-clockwise direction. The speed of rotation of the wheels is set in units of n degrees per second. Based on the radius of the driving wheel, r, the speed of the belt can be estimated as $U = 2\pi rn/360 = n\pi/90$. The range of belt speeds achievable is from 0 to 20 cm s^{-1}. The belt speed is held constant for any particular experimental run.

During an experiment, the belt is impulsively started to run a specific speed and not ramped slowly up to speed. The stratified fluid is mixed at the surface. This mixing layer deepens quickly over about 10 to 30 s and then deepens much more slowly. This behaviour is explored in section 4.2.

A coordinate system is defined where x is increasing to the right and z is decreasing downwards. The origin was chosen at the left side of the tank and at the base of the structure of the conveyor belt apparatus (see figure 4.4). The choice of origin is arbitrary but this particular choice made it easier to compare between different experiments as the large feature of the conveyor belt is easily identified in digital video. For analysis, only selected fields of view in the upper and lower parts of the tank are used to measure the turbulence and the waves, respectively. These are indicated in the sketch of figure 4.4. These fields of view are called 'regions of interest.'

Up to three digital cameras were used in a single experiment measuring of the thickness of the mixed layer, the turbulence in the mixed layer, and the waves in the stratified lower layer, respectively. Most experiments, however, were ran with only one camera measuring one of these three aspects.

The stratification was created using a double-bucket apparatus (Oster (1965)) with a buoyancy frequency of $N = \sqrt{-\frac{g}{\rho_0}\frac{d\rho}{dz}} = 1.4$ s^{-1} where g is the acceleration due to gravity, $\rho_0 = 1.00$ g cm^{-3} is a reference density, and $\rho(z)$ is the density of the fluid as a function of depth.

A conductivity probe (Precision Measurement Engineering) was used to measure the density stratification at the beginning of each experiment. Experiments

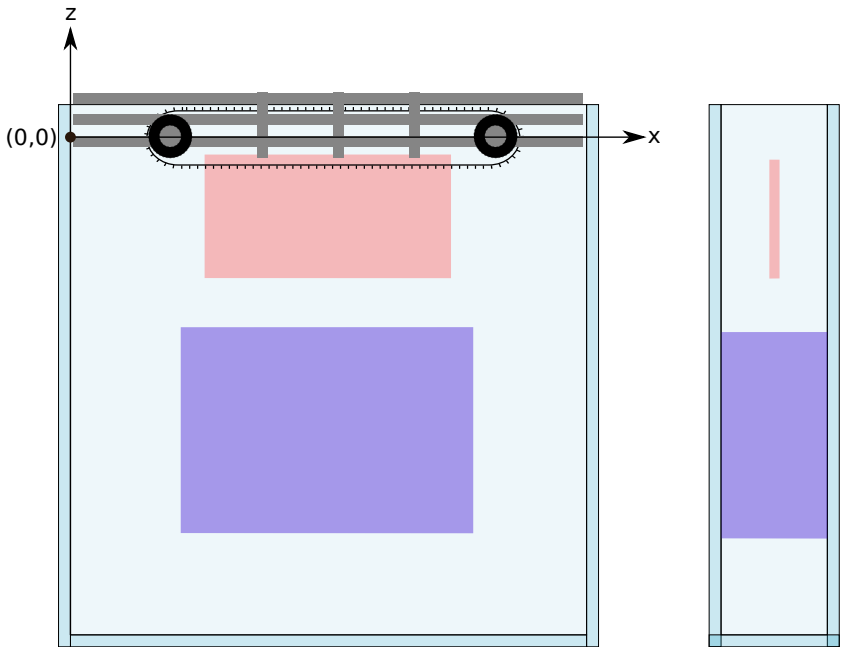

Figure 4.4: Front and side views of the tank. The left inside edge of the tank is defined as $x = 0$ increasing to the right and the base of the support structure for the conveyor belt is defined as $z = 0$ increasing up., The upper shaded region indicate the plane where PIV measurements for turbulence are taken. The lower shaded region shows where synthetic schlieren measurements for waves are taken. Note that for synthetic schlieren, the waves are assumed to be uniform across the width of the tank.

with different values of U were performed consecutively with at least a 20 minute delay for the fluid to come to rest. This allows investigation of the effect of difference thicknesses of the layer and saves having to drain and refill the tank.

Vertical traverses of density data were taken at the beginning and part way through sets of experiments. Figure 4.5 shows examples of the density profiles achieved. The buoyancy frequency was estimated by a linear regression through the linearly stratified region. Over several sets of experiments values of $N = 1.38$ s^{-1} to 1.50 s^{-1} were achieved using the same mass of salt and volume of water in the double-bucket apparatus. The error in estimating N is ± 0.1 s^{-1}.

There was usually a small mixed region near the bottom of the tank due the initial mixing when the tank is being filled.

4.2 Mixed layer deepening

Food-grade dye was added to the upper part of the fluid to act as a passive tracer marking the thickness of the mixed layer. Red dye as opposed to, say, blue dye was chosen for the mixed layer because the red light of the laser light sheet used to observe the turbulence is absorbed the least by red dye. The experiments listed in table 4.1 were used to explore how the depth of the mixed layer deepened over time. These mixed layer deepening experiments took several hours to run.

Because the mixed layer deepened relatively slowly (on the order of several hours to reach the bottom of the tank), a time-lapse camera was set up. Figure 4.6 shows a sequence of images taken at progressively larger time intervals. The time lapse method sequentially captured 1 image every second for 10 minutes, then 1 image every 10 seconds for 20 minutes, and finally 1 image every minute until the end of the experiment.

A vertical time series through the center of the tank ($x = 24$ cm) is used to measure the deepening mixed layer over time as shown in figure 4.7a. The colour image is converted to a gray scale image and then a threshold filter is applied to convert it to a black and white image. This creates a region of 'white' on the interior of the vertical time series which represents the undyed fluid. Searching for the

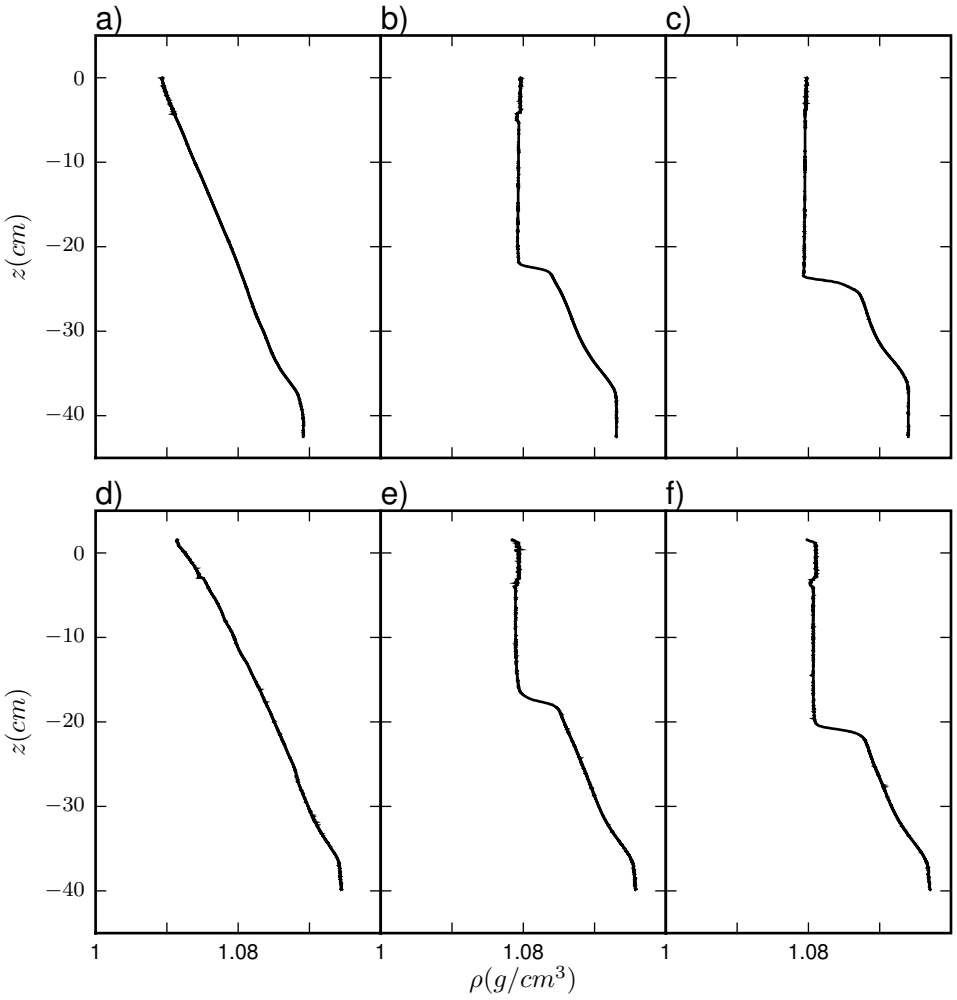

Figure 4.5: Examples of stratifications measured in conveyor belt experiments. Panels a, b, c show the stratifications obtained at the beginning, middle, and near the end of a single 5 hour long mixed layer deepening experiment (e090128a). Panels d, e, f show the stratifications obtained before and after distinct experiments performed using the same starting stratification (e090224).

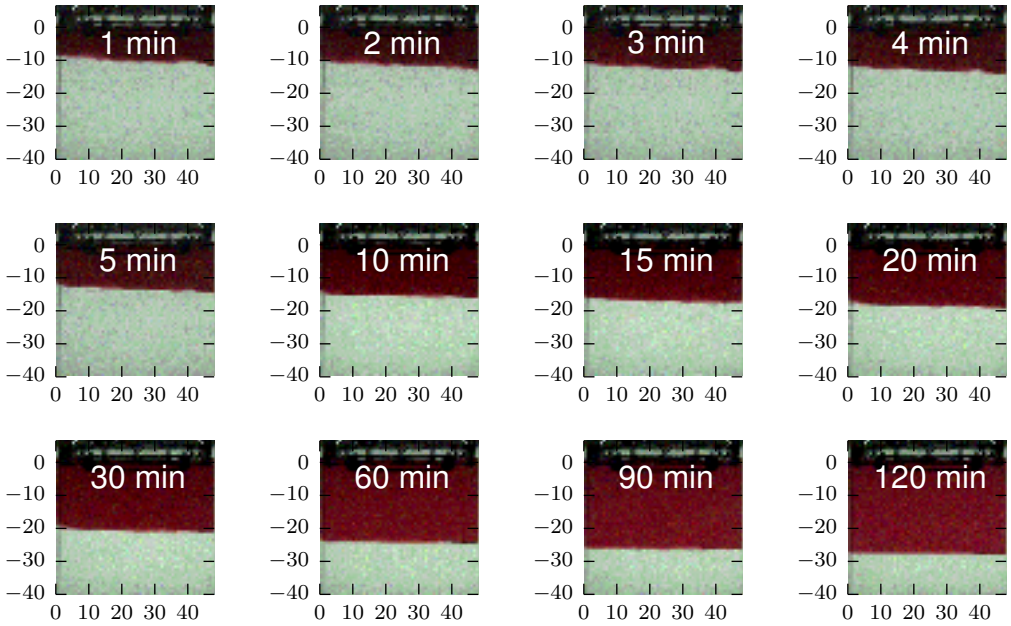

Figure 4.6: Snapshots at various times showing deepening of mixed region (for experiment e090120a). Red dye marks the thickness of the mixed layer at the times shown. The mixing is fairly uniform across the tank with slightly more mixing at the right side and slightly less on the left side.

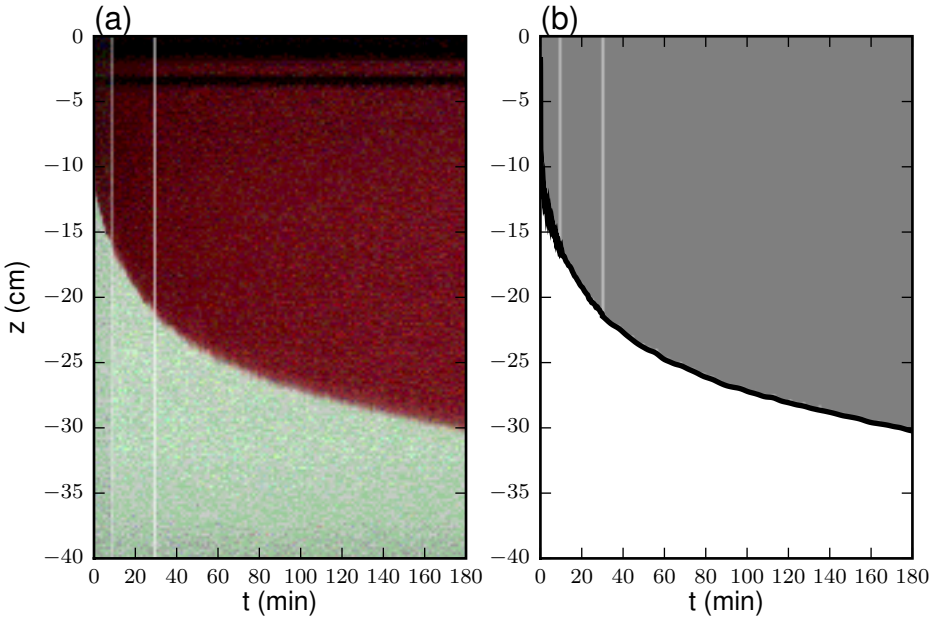

Figure 4.7: (a) Vertical time series through centre of the tank, $x = 24$ cm. The vertical white lines indicate changes in the sampling rate of the time lapse video (see text for details). (b) Thresholded image shown in gray and white and the interface (with a 10-element smoothing filter applied) shown as the solid black line.

largest coordinate of only the white pixels thus gives the position of the base of the mixed layer. This process is shown in figure 4.7b.

The mixed layer depth is plotted against time, figure 4.8, for each of the three experiments listed in table 4.1. To fit a power law, the graph is made on log-log axes and a linear regression is used. The results are listed in the same table. For experiment e090128a, vertical barriers were placed at $x = 12$ cm and $x = 36$ cm in order to investigate the effect of a narrow tank. The width does not seem to impact significantly the deepening rate of the mixed layer.

After the initial deepening, this analysis shows that mixed layer deepens slowly compared to the time scales of the waves and turbulence studied in the rest of this chapter. Hence, we can assume that the depth of the mixed layer is fixed for the purposes of analysis of waves and turbulence for any particular experiment. The depth of the mixed layer is still a relevant parameter but will assumed to be a constant parameter when comparing individual experiments.

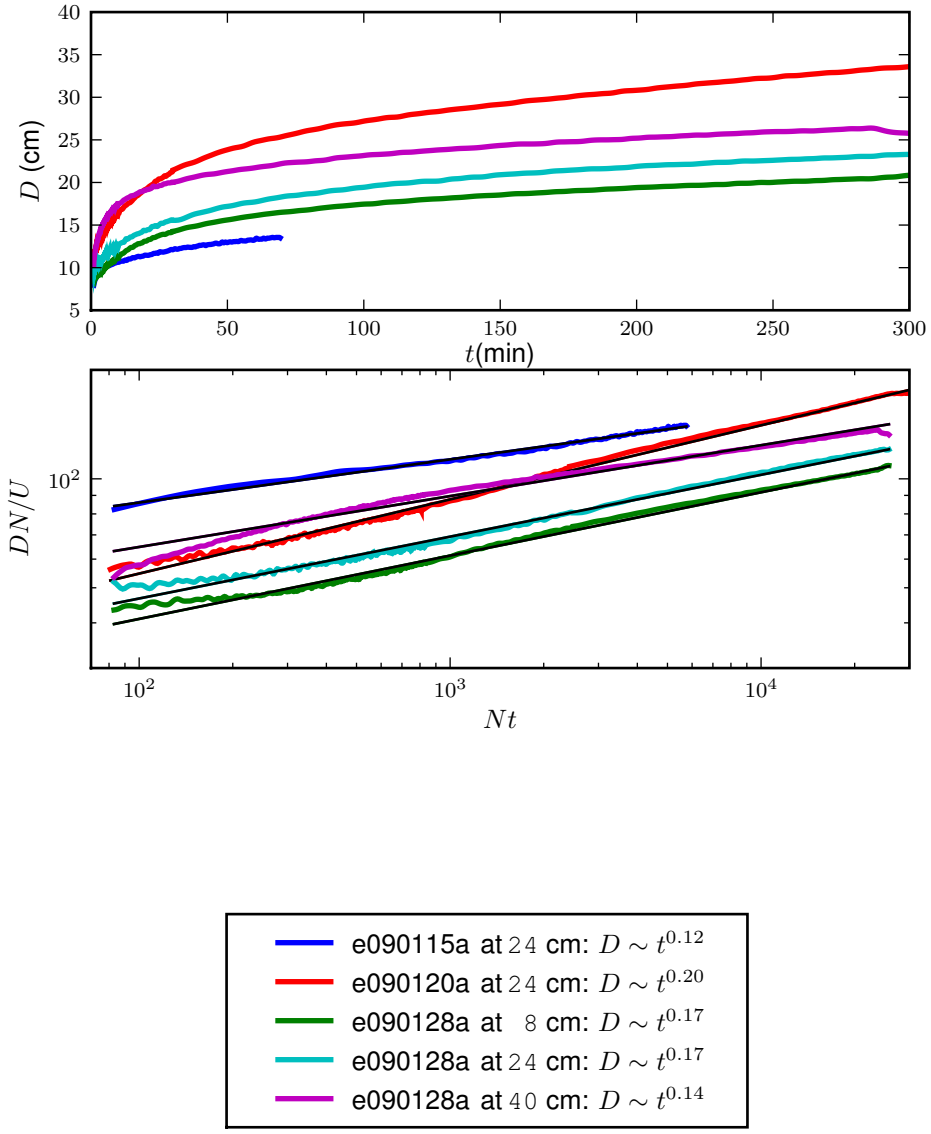

Figure 4.8: (a) Curves show mixed layer depths as a function of time for different experiments. (b) as in (a) but on a log-log scale and showing linear regressions and using non-dimensional units. The legend indicates the power law measured for each experiment.

Table 4.1: List of experiments measuring rate of mixed depth deepening

Experiment	U (cm/s)	Power law	Note
e090115a	8	$\sim t^{0.12}$	x = 24 cm
e090120a	16	$\sim t^{0.20}$	x = 24 cm
e090128a	16	$\sim t^{0.17}$	x = 8 cm
e090128a	16	$\sim t^{0.17}$	x = 24 cm
e090128a	16	$\sim t^{0.14}$	x = 40 cm

Entrainment of stratified fluid by turbulent mixing has a long history in the literature. There are industrial applications such as gases in mines, and environmental processes such as deepening of the ocean mixed layer by a storm and eroding of an atmospheric inversion. In laboratory studies two primary types of experiments are performed: shear-free turbulence and turbulence with a sheared mean flow. The former is often created using a mixing box experiment (Rouse and Dodu (1955), Turner (1968), Linden (1975), Xuequan and Hopfinger (1986), Dohan and Sutherland (2003)). The latter is either done through a surface stress in a annular tank (Kato and Phillips (1969), Kantha et al. (1977)), a buoyant overflow (Ellison and Turner (1959)) or a Odell-Kovasznay flume with an accelerated upper section and a stationary lower section (Narimousa and Fernando (1987)). The stratification is either a two layer fluid or linearly stratified. In a linear stratified fluid, internal waves can propagate away from the mixing region slowing the rate of deepening (Linden (1975)). It is common to express the rate of deepening in terms of an *entrainment coefficient*, $E = u_e/u$ which is the ratio of the deepening rate $u_e = dD/dt$ to the characteristic velocity scale u. Ellison and Turner (1959) were the first to conjecture that the rate of entrainment should be a function of the Richardson number, $E = f(\mathrm{Ri})$. See Fernando (1991) for a review of turbulent mixing of both shear-free and sheared stratified flows.

Typically, papers discussing the turbulent entrainment rates report their results in terms of a power law based on Ri of the form $E = k\ \mathrm{Ri}^{-n}$ (e.g. the review by Fernando (1991)). However, there are several different 'Richardson numbers' based on several different velocity and length scales that have been used. All capture the relative importance of buoyancy forces versus shear stresses but direct comparison

of results from one paper to another can be non-trivial.

For example, Kato and Phillips (1969) suggested that $E \sim Ri^{-1}$ using a bulk Richardson number of Ri $= (g\Delta\rho/\rho_0)D/u_*^2$ where u_* is the frictional velocity imposed on the surface of an annular tank with linear stratification. For our experiment, we choose a characteristic velocity as $u = U$, the belt speed. A linear background stratification with constant gradient of $\Gamma = d\rho/dz$ gives a depth dependent density jump of $\Delta\rho = \Gamma D/2$. Integrating

$$E = \frac{u_e}{u} = \frac{dD/dt}{u} \sim \left(\frac{g\Gamma/\rho_0 D^2}{u^2}\right)^{-n} \tag{4.1}$$

leads to a power law of the form

$$D \sim t^{1/(1+2n)} \tag{4.2}$$

A different choice of characteristic velocity, assuming that u is time independent, would lead to a different constant of proportionality but the same exponent in the power law. As shown in figure 4.8, we observed that our mixed layer depth increased with a power law in the range of $D \sim t^{0.12}$ to $D \sim t^{0.20}$. This corresponds to values of n in the range of 2 to 3.5 which is much higher than what Kato and Phillips (1969) found. Expressed as power law, their experiments suggest that $D \sim t^{1/3}$. We only performed a few experiments on the rate of change of the mixed layer depth and hence the errors is the estimate of the power law are fairly large with the uncertainty in the exponent being 25%. However, these measurements are sufficient to demonstrate a difference in behaviour with the Kato and Phillips (1969) experiments, namely, that the mixed layer deepens much more slowly in our experiments.

Unexpectedly, we find that our deepening rates are more consistent with the rates reported in Xuequan and Hopfinger (1986) of a shear-free mixing box experiment with a oscillating grid. They reported deepening rates of $D \sim t^{1/5}$ for two layer stratifications and $D \sim t^{1/8}$ for constant gradient stratifications.

4.3 Wave measurements

The turbulent forcing in the upper mixed region produces internal waves in the lower stratified region. To quantitatively measure the internal waves in the stratified region, synthetic schlieren (Sutherland et al. (1999)) was used.

Behind the tank a bank of fluorescent lights illuminated a screen of black and white lines. The lines were 0.2 cm thick and the screen was placed 10 cm behind the tank. A digital video camera recorded the image of the screen through the salt-stratified fluid. Internal waves change the local density and hence the index of refraction. This distorts the image of the lines. This technique, called synthetic schlieren, can be used to determine the changes in the stratification, characterized by the perturbation buoyancy frequency, ΔN^2, or the rate of change of the perturbation buoyancy frequency, ΔN_t^2.

For these conveyor belt experiments, sample raw images of data applicable to schlieren analysis are shown in figure 4.9. For the conveyor belt experiments, there are 36 distinct experiments that have data which can be analyzed by synthetic schlieren. Often these experiments are done in sequence with different belt speeds but increasing mixed depth. Variation between sequences of experiments is primarily due to the experimental error in creating the initial linear stratification of salt water.

We analyzed a region of interest away from the sides, bottom, and mixed layer for waves. In particular, we define the region as 10 cm $< x <$ 34 cm at $\Delta x =$ 1.0 cm intervals, -35 cm $< z < -15$ cm using every pixel of resolution available, and all frames (either 24 fps or 30 fps depending on the camera used) in time.

The simplest analysis is to perform qualitative schlieren by subtracting from the current image an initial image before the experiment began. This is depicted in figure 4.10.

To use quantitative synthetic schlieren, the open source software *igwtools* was used. Specifically, the 'dn2t' mode is used with the derivative computed over frames spaced by $\Delta t = 1/15$ s apart. The physical parameters of the distance from the grid to the back of the tank, the thickness of the tank walls, and the width of the tank

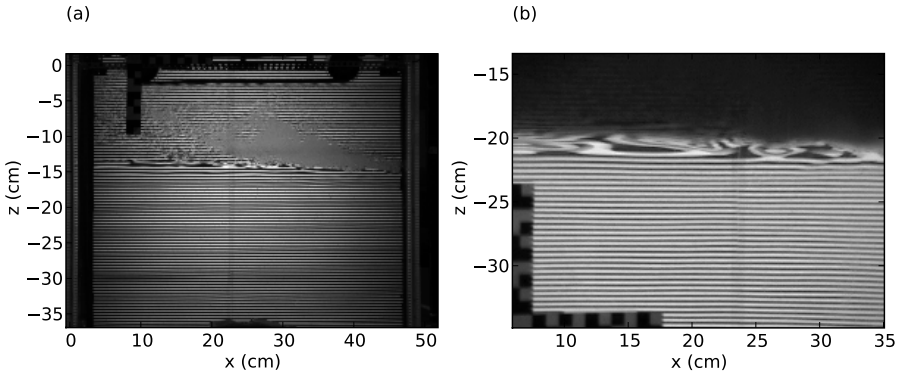

Figure 4.9: Examples of the raw images used for synthetic schlieren analysis of internal waves. a) Early experiments captured the entire tank in the field of view, e.g. e080730e at $t = 50$ s. b) Later experiments zoomed in on only a region of interest below the mixed region, e.g. e090303f at $t = 50$ s.

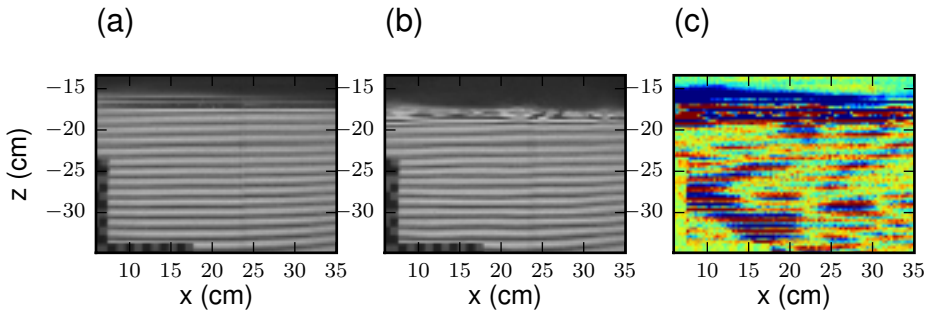

Figure 4.10: An example of qualitative schlieren. (a) A snapshot from before the experiment is started. (b) A snapshot during the experiment. (c) The difference in pixel intensities between (a) and (b). This shows the structure of the internal waves. Note the horizontal lines are actually more finely spaced than (a) and (b) suggest. See figure 4.9 for a better image of the lines.

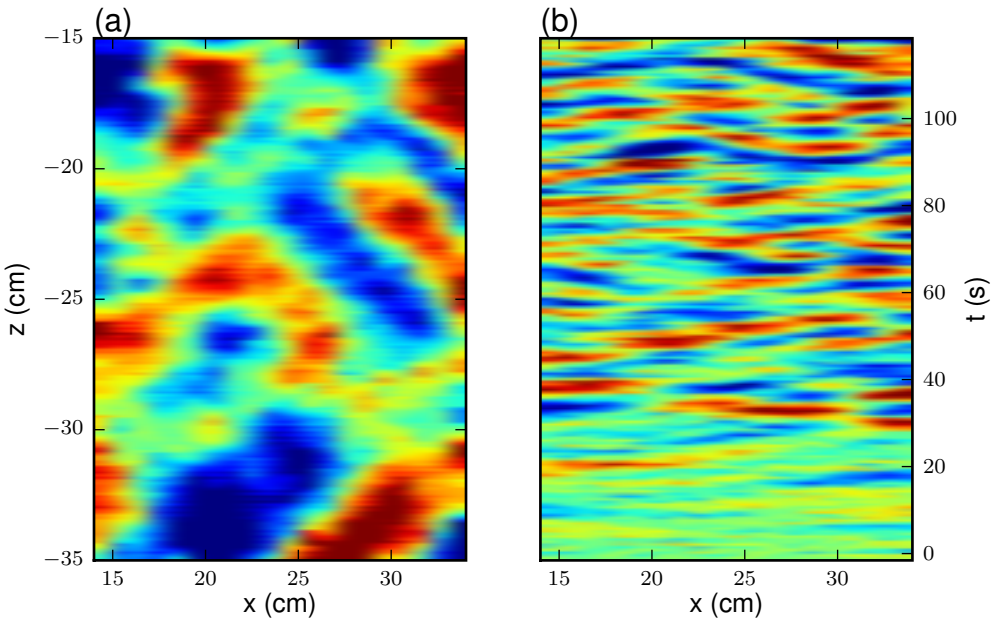

Figure 4.11: ΔN_t^2 field (a) snapshot at $t = 50$ s (b) horizontal time series at $z = -25$ cm of experiment e080730c. The colour scale used ranges from -0.1 s^{-3} (blue) to 0.1 s^{-3} (red).

were used. This gives the ΔN_t^2 field as shown, for example, in figure 4.11.

We observed wave packets propagating downwards. Wave packets travelling both towards the right and the left are observed. Horizontal time series were constructed to observe the waves passing a particular vertical position (see figure 4.11b for an example). There was a dominant observed frequency in the waves of approximately $\omega = 1$ s^{-1} (or $\omega/N = 0.7$) as can been seen by the quasi-uniformly spaced lines of constant phase in the horizontal time series.

To compute the energy of the waves, the horizontal time series was Fourier transformed to $k_x - \omega$-space (e.g. figure 4.12). The DC component of the spectra ($k_x = 0$ and $\omega = 0$) was explicitly set to zero. The spectra were low-pass filtered with a cut-off such that $\omega < N$, to consider only freely propagating internal waves, and $k_x < 1.0$ to eliminate high frequency noise.

The vertical displacement, ξ, in Fourier space is related to ΔN_t^2 by

$$A_\xi = A_{\Delta N_t^2}/(N^3 k_x \sin\Theta) \tag{4.3}$$

where $A_q(k_x, \omega)$ represents the amplitude of the spectral component of the field q

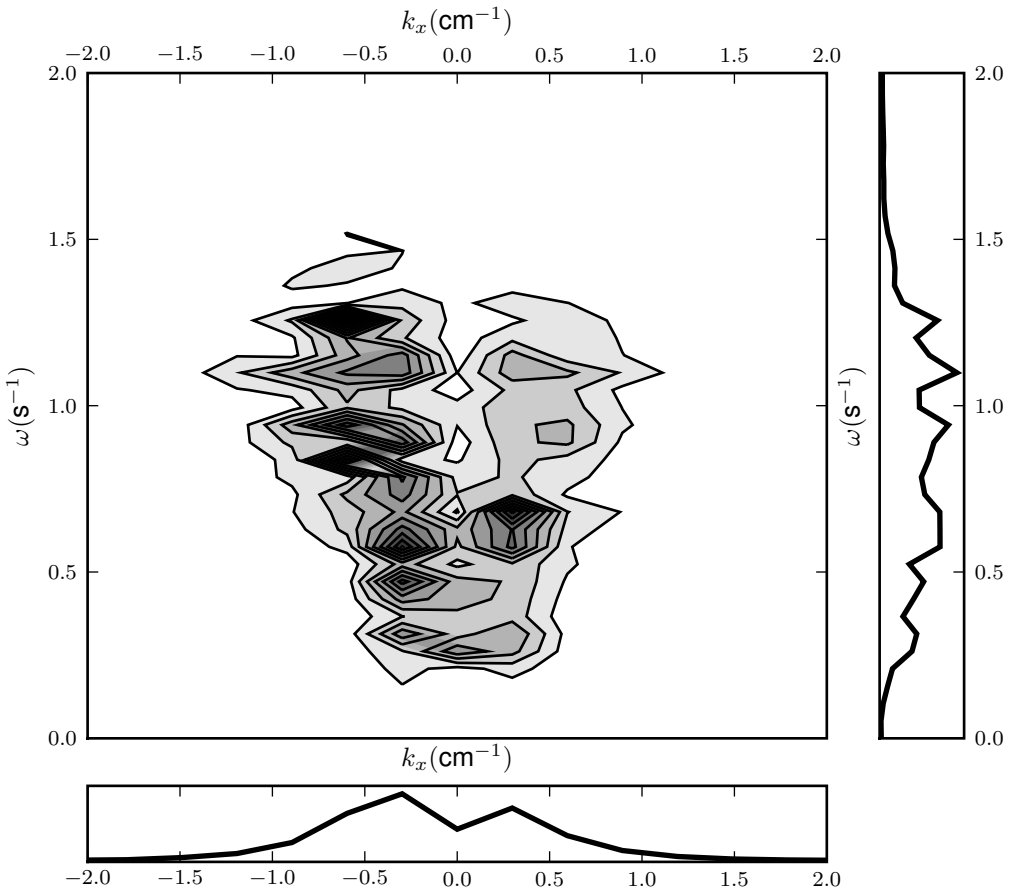

Figure 4.12: Wave spectrum in k_x, ω-space of the horizontal time series shown in figure 4.11. The right axis shows the sum in energy over all k_x while the lower axes shows the sum in energy over all ω (experiment e080730c).

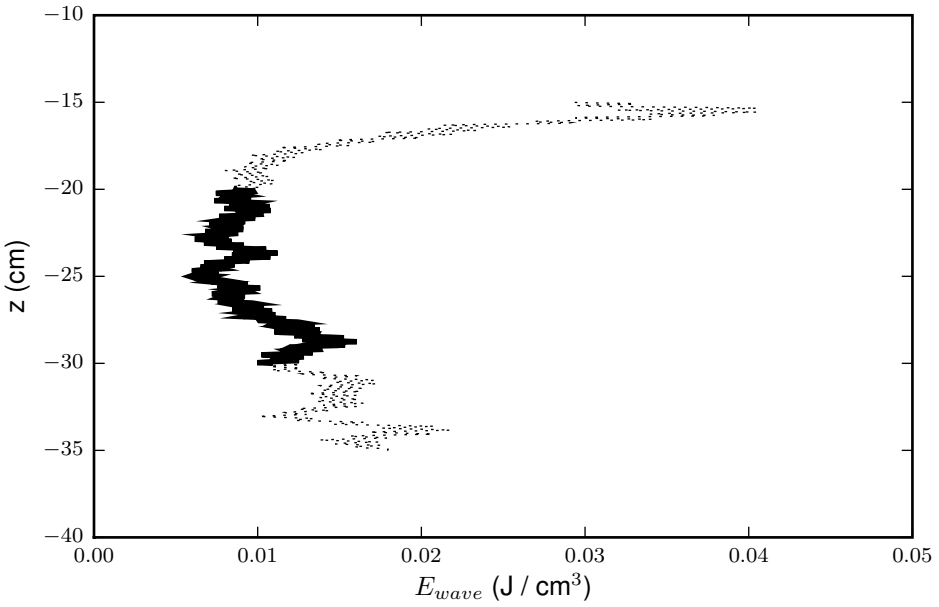

Figure 4.13: Wave energy density as a function of depth for experiment e080730c. A representative value of the wave energy density is taken as the average value over the solid black region.

where $\omega = N\cos\Theta$. Using characteristic values of $N = 1.4s^{-1}$, $\sin(\theta) = 1/\sqrt{2}$, and $A_{\Delta N_t^2} = 0.1$ (as given in figure 4.11) we use equation 4.3 and find that A_ξ/λ has a typical value of approximately 0.8% justifying the use of linear theory to analyze the internal waves. The energy density of a single plane wave is given by

$$E'_{wave} = \frac{1}{2}\rho_0 A_\xi^2 N^2. \tag{4.4}$$

This energy was computed for each component k_x, ω and integrated to give the total wave energy density in the horizontal time series.

$$E_{wave} = \int E'_{wave} dk_x d\omega \tag{4.5}$$

Repeating this procedure for each horizontal slice taken at different vertical levels allows us to plot E_{wave} as a function of depth, z, as shown in figure 4.13. The wave energy density is approximately constant below $z = -20$ cm so a vertical average between -30 cm $< z < -20$ cm is taken to get a measurement of the wave energy as a function of the conveyor belt speed.

Table 4.2: The wave energy density, E_{wave}, for each synthetic schlieren experiment.

Expt:DatasetId	U (cm/s)	N (1/s)	D (cm)	E_{wave} (J/cm^3)
e080729a:22	4	1.50	4.2	0.0054
e080730a:2	4	1.44	4.9	0.0011
e090224a:46	4	1.47	6.1	0.0020
e080730f:7	4	1.44	16.5	0.0003
e090224f:54	4	1.47	18.9	0.0005
e090303a:60	6	1.41	6.1	0.0056
e080729b:23	8	1.50	5.6	0.0358
e080730b:3	8	1.44	6.7	0.0041
e090303h:67	8	1.41	7.0	0.0142
e090224b:47	8	1.47	8.0	0.0055
e090224b:48	8	1.47	8.0	0.0053
e080730g:8	8	1.44	16.3	0.0021
e090224g:55	8	1.47	19.2	0.0032
e090224g:56	8	1.47	19.2	0.0058
e090303b:61	10	1.41	9.2	0.0158
e080729c:24	12	1.50	8.4	0.0636
e080730c:4	12	1.44	8.8	0.0095
e080730c:18	12	1.44	8.8	0.0258
e080730c:73	12	1.44	8.8	0.0090
e090224c:49	12	1.47	10.8	0.0168
e090224c:50	12	1.47	10.8	0.0190
e090303i:68	12	1.41	11.0	0.0376
e080730h:9	12	1.44	17.7	0.0052
e090224h:57	12	1.47	19.8	0.0104
e090303c:62	14	1.41	12.9	0.0286
e090303c:70	14	1.41	12.9	0.0911
e080730d:5	16	1.44	11.1	0.0179
e090224d:51	16	1.47	14.5	0.0253
e090224d:52	16	1.47	14.5	0.0260
e090303j:69	16	1.41	14.9	0.0366
e090303d:63	16	1.41	15.9	0.0163
e080730i:10	16	1.44	17.3	0.0085
e080729d:25	16	1.50	20.0	0.1458
e090224i:58	16	1.47	20.4	0.0485
e090303e:64	18	1.41	18.9	0.0208
e080730e:6	20	1.44	14.2	0.0195
e080729e:26	20	1.50	14.3	0.1213
e090224e:53	20	1.47	17.4	0.0299
e080730j:11	20	1.44	19.2	0.0158
e090303f:65	20	1.41	21.7	0.0269
e090224j:59	20	1.47	21.9	0.0144
e090303g:66	22	1.41	23.6	0.0196

This analysis was repeated for each experiment that could be processed with synthetic schlieren. In figure 4.14 we show how E_{wave} varies with the belt speed U. The average energy of the waves increases with the belt speed U but there is also an increase in the range of E_{wave}. The depth of the mixed layer is also changing between experiments which is another relevant parameter in describe the energy of the waves. The values are given in table 4.2. The energy densities seems to be linearly dependent on the belt speed which is unexpected since one would expect that energy should scale with velocity squared. The figure also shows that the energy density decreases with increasing mixed layer depth.

Figure 4.14 demonstrates that as the belt speed U increases then so does the energy density of the wave field. However, either a peak of wave energy is occurring at about $U = 16$ cm s^{-1} or the wave energy is reaching a saturation level. Saturation in this case means that the turbulence is unable to force waves with larger amplitudes.

Figure 4.14 also shows that for a series of experiments with the same buoyancy frequency but with increased mixed layer depth the wave energy density describes the same trend but is shifted down. Therefore, as the thickness of the mixed layer increases, the energy density decreases.

Finally, figure 4.14 suggests that the order of experiments is significant because the mixed layer deepens at different rates depending on the belt speed. However, this does not seem to impact the general trend of increasing wave energy density with increased belt speed U.

The energy density scales with the square of the buoyancy frequency. Therefore an overestimation of the background buoyancy frequency will lead to a gross overestimation of the wave energy density. For the experimental series e080729 it is possible that the initial buoyancy frequency was incorrectly overestimated leading to the considerably larger energy observed. Stratifications for all experiments were created using the same procedure, the same mass of salt and the same volume of water in the double-bucket apparatus. The variation in stratification between experimental series was due to experimental error. The buoyancy frequency measured for e080729 was $N = 1.50$ which was the highest initial N for all series of

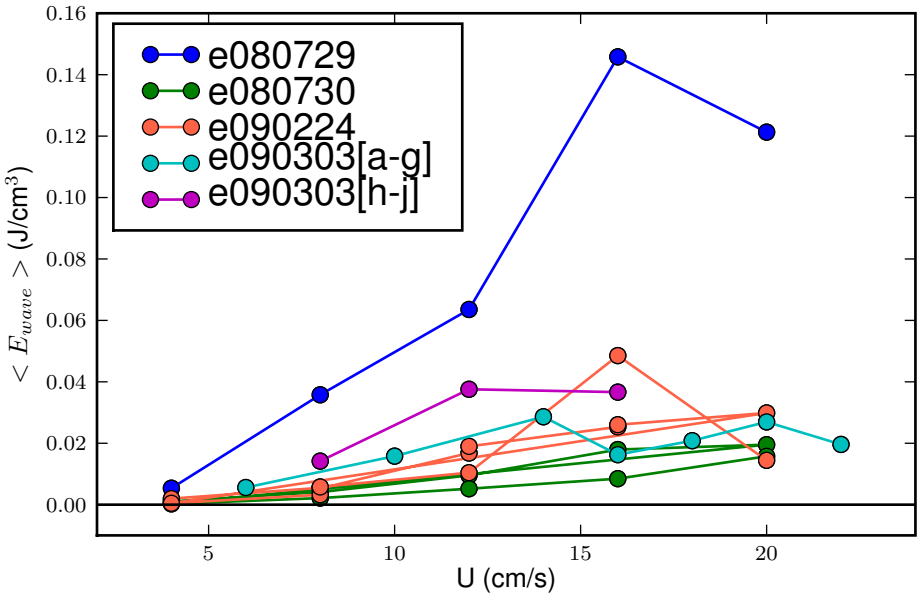

Figure 4.14: Wave energy density as a function of belt speed. The colours indicate experiments that were done in succession with the same starting stratification. The lines indicate the order the experiments were performed starting from the slowest belt speed.

experiments.

It had initially been assumed that the buoyancy frequency in the lower stratified region remained constant between one run and the next. However, upon examination of density profiles taken part way through and at the end of a sequence of experiments, the stratification in the lower region increased over the course of the series, thereby increasing the buoyancy frequency. This in turn caused an underestimation of the wave energy density. Therefore, it was not possible to determine the quantitative effect of the deepening mixed region alone on the wave energy density.

4.4 Turbulence measurements

The upper mixed region is turbulently forced and exhibits motion on a range of scales. Since the fluid is not density stratified and the flow varies across the tank, synthetic schlieren could not be used to visualize the flow field. We required a quantitative technique that could make whole field measurements of the velocity

field. In our lab we had access to a line laser that produced a laser light sheet and a digital video camera so it was natural to attempt a simple form of particle image velocimetry (PIV) to measure the turbulence. There are other techniques that might have been used given different resources as well as more complex versions of PIV that were available commercially. The advantage of this technique is that it was available, relatively inexpensive, and sufficient for our purposes.

Nearly neutrally buoyant Pliolite particles were injected in a salt water mixture at about 2 cm below the surface prior the start of the experiment. Pliolite has a specific density of 1.03 (Eliokem Material & Concepts product data sheet). The particles tracked the motions of the fluid and also marked the depth of the mixed region when the red dye was not used. A laser light sheet illuminated a plane of the particles the upper mixed layer of the tank. The laser light passed through a lens to create a light sheet that is uniform in intensity along the line and had a uniform distribution across the line. (SNF Straight Line, 600 nm, < 1 mW, manufactured by Lasiris, Inc.). The particle seeding was relatively sparse compared to a conventional PIV setup. However, the laser light intensity is also typically much higher. A JAI digital video camera with a higher resolution of 1372×1024 recording at 24 frames per second was used to capture the motion of the particles.

Figure 4.15 shows an example of a raw image obtained. The images are naturally very dark due to the low light conditions used (the laser is fairly weak and the lab lights are turned off during a PIV experiment). This can also be seen by looking at the histogram of the image as shown in figure 4.16. The histogram is doubly-peaked with the first peak being the 'black' background and the second being the light from the laser sheet. However, the image as recorded is much darker that what was observed by eye during the experiment. Since the laser was red, the experiment observed by eye in the lab were also red. The JAI camera was a gray-scale camera and only captured the light intensity.

Although the PIV processing software (see below) was able to use these images to infer the velocity field, the particles were barely obvious by eye. For the reader's benefit, we enhance the image by performing a gamma correction which spreads out the 'dark' values over a larger range of numerical intensities as demonstrated

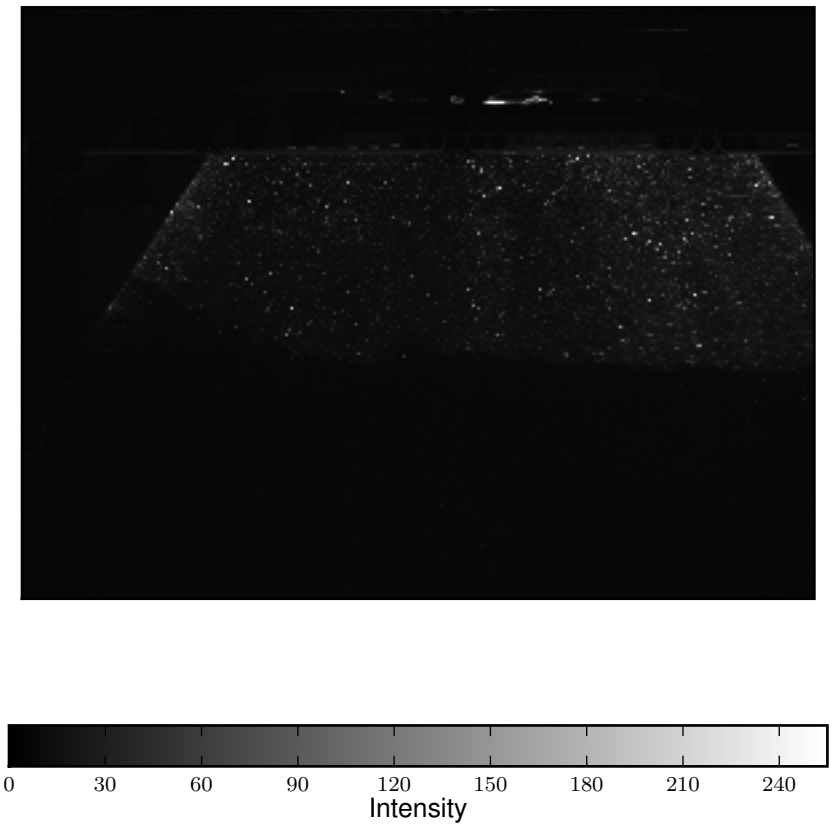

Figure 4.15: Example of a raw image as recorded by DigiFlow from a PIV experiment.

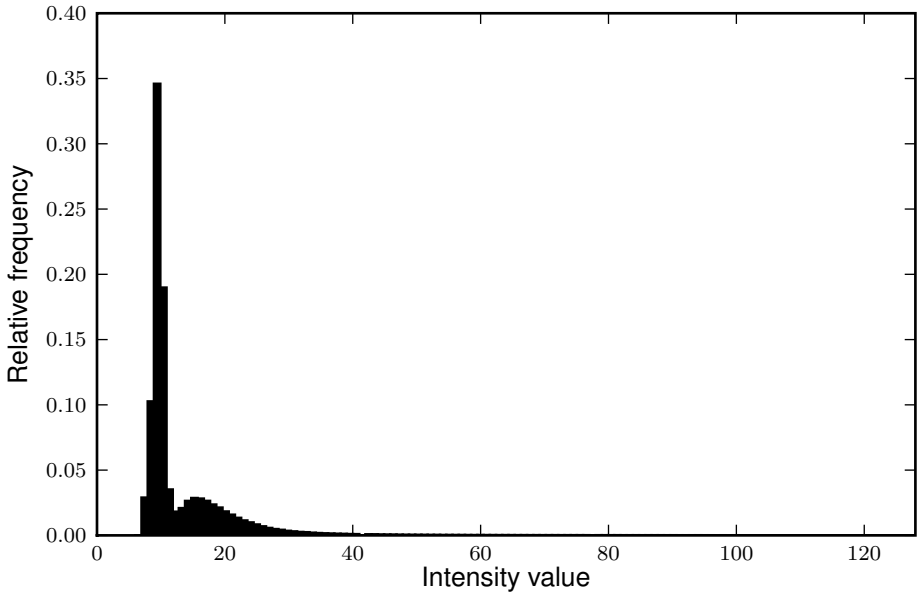

Figure 4.16: Histogram of intensities of raw image as recorded by DigiFlow.

by the histogram in figure 4.17. We also change bounds of the colour map to focus on the region where there is the most information as in figure 4.18.

We processed the images from the camera using open source software CIVx (version 20051012). We chose an interrogation-window size of 32 pixels and a search-window size of 64 pixels. The search grid was set so that we had 100% overlap between adjacent grid boxes. A smoothing parameter of $\rho = 1$ was used. CIVx is a hierarchical PIV analysis program which uses two iterations to analyze the flow field. The first cross-correlation estimates the velocity field and the second uses this as an estimate to make a more accurate analysis of the velocity field in a second pass. See Fincham and Delerce (2000); Fincham and Spedding (1997) and the user manual of CIVx for more details. The same parameters were used for both the first and second iteration of CIVx.

There were 36 conveyor belt experiments for which turbulence measurements using PIV were obtained. The output of CIVx is a velocity field $\vec{u} = (u, w)$ with horizontal and vertical components on a two dimensional grid at each time interval. We were only concerned with a region of interest below the conveyor belt, away

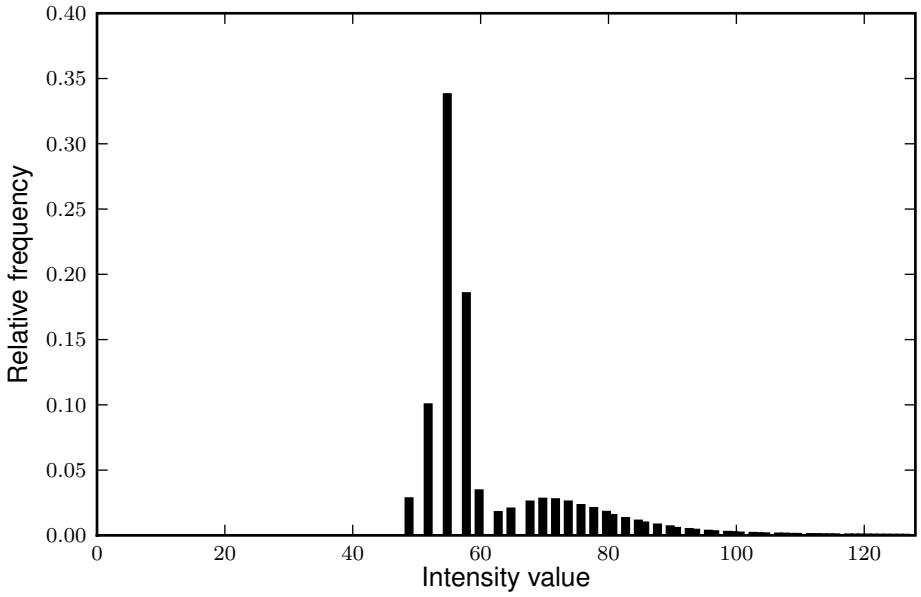

Figure 4.17: Histogram of intensities of gamma corrected image. The 'dark' colours have been spread out over a large range of numeric intensity values as compared to figure 4.16.

from the side walls, and above the stratified region. An example of the vector field $\vec{u}$ is given in figure 4.19a. This vector field was averaged over two minutes of the experiment to give the mean flow, $< \vec{u} >$, that developed in the mixed layer. A perturbation velocity, $\vec{u}' = \vec{u} - < \vec{u} >$, was computed for each frame captured by PIV. The mean circulation is shown in figure 4.19b and an example of the perturbation velocity is shown in figure 4.19c.

The average turbulent kinetic energy density was computed by

$$E_{TKE} = \frac{1}{A} \int \frac{1}{2} \rho_0 \left(u'^2 + w'^2 \right) dA \tag{4.6}$$

where A is the area of the region of interest for the turbulence. This quantity is plotted against time in figure 4.20 where $t = 0$ corresponds to when the conveyor belt was first turned on. In this example, as in all other experiments performed, there was no observed trend showing either increasing or decreasing E_{TKE} over the duration of each experiment.

The frequency spectrum of E_{TKE} was red with an example shown in figure 4.21.

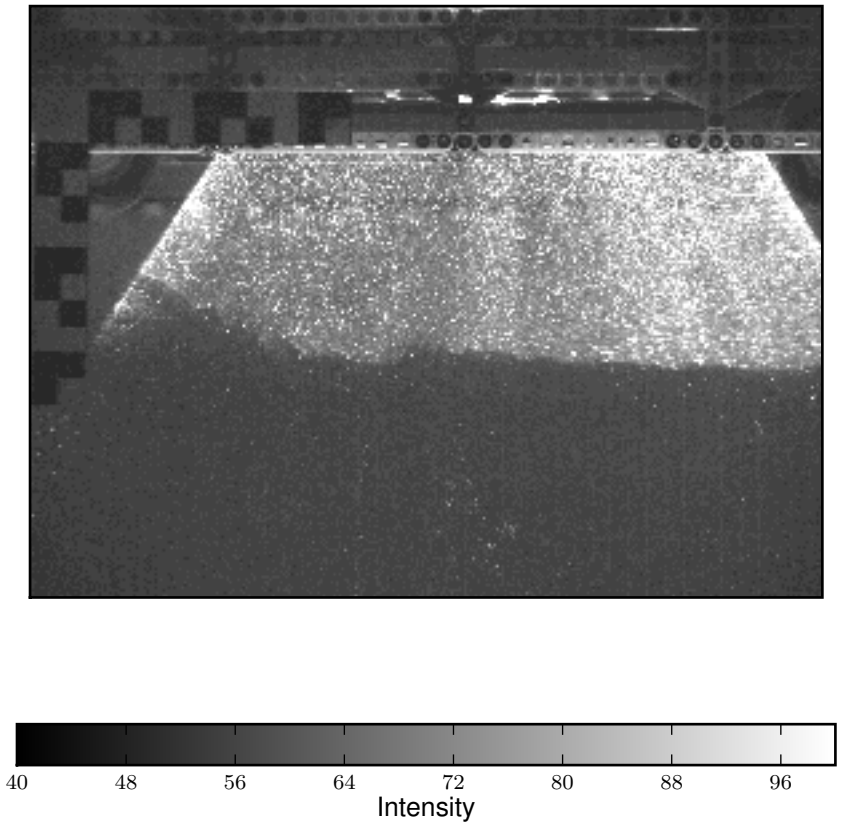

Figure 4.18: Example of a PIV image for processing, enhanced with a gamma correction and using a narrower colormap to show details.

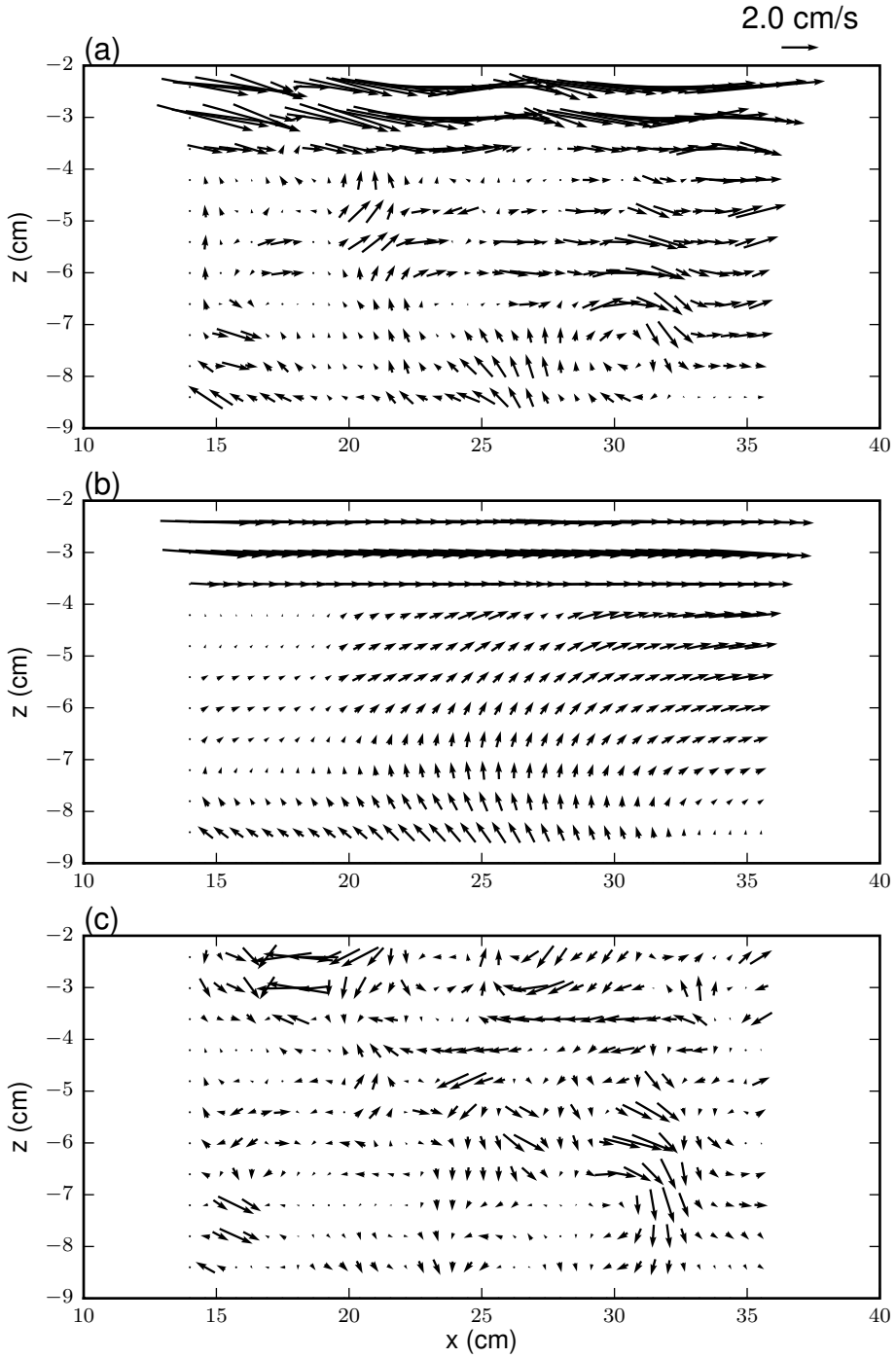

Figure 4.19: Sample velocity field measurements from PIV taken from experiment e090224h show using a quiver plot where the length of the arrows are proportional to the speed and the direction of the arrows indicated the direction of the flow. a) Total velocity field b) Mean circulation c) Perturbation velocity field

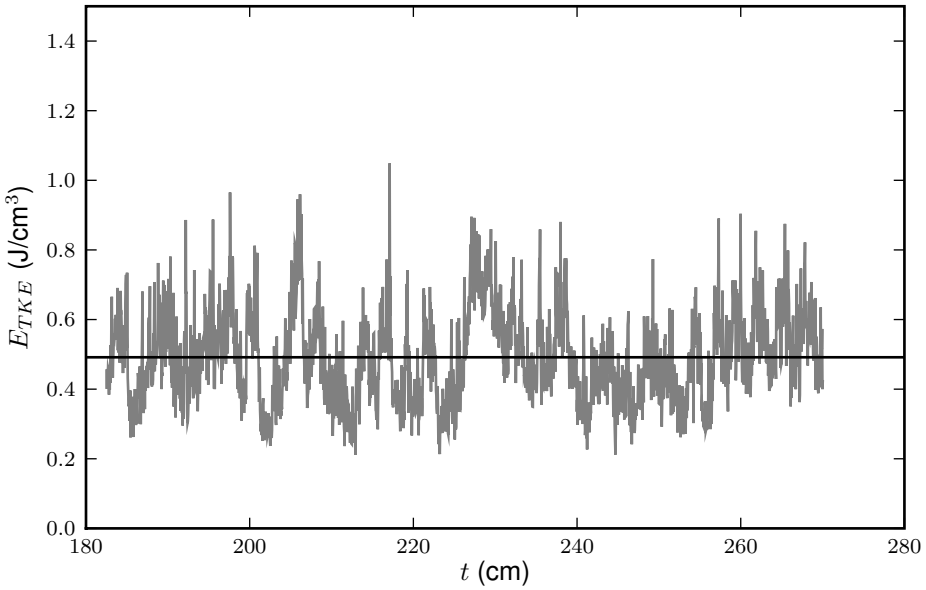

Figure 4.20: Turbulent kinetic energy density of the mixed layer as a function of time for experiment e090224h. The black line indicated the average in time.

For that experiment, the power law was $E_{TKE} \propto \omega^{-0.43}$. There was no dominant frequency observed in the frequency spectrum.

We computed the time average of the E_{TKE} to get an estimate of the turbulent energy for each experiment with its corresponding conveyor belt speed. The average turbulence kinetic energy is plotted against the belt speed U as shown in figure 4.22. The values are given in table 4.3.

4.5 Results

The lighting conditions in our laboratory required for particle image velocimetry (PIV) and for synthetic schlieren (SS) were in conflict. PIV requires the lab lights to be turned off while SS needs bright back lighting. Although it is possible for these two techniques to be done concurrently (Dalziel et al. (2007)), this was not done in these experiments. An experimental sequence (different values of U between tank refills) is either configured for PIV or SS and the data is compared by matching the belt speed, and the stratification including initial mixed layer depth. The effect is

Table 4.3: The turbulent kinetic energy density, E_{TKE}, for each PIV experiment.

Expt:DatasetId	U (cm/s)	N (1/s)	D (cm)	E_{TKE} (J/cm^3)
e080728a:13	4	1.38	6.0	0.0826
e090224a:101	4	1.47	6.1	0.6573
e080728k:85	4	1.38	10.2	0.1166
e080728f:80	4	1.38	13.3	0.1093
e090224f:106	4	1.47	18.9	0.1115
e090303a:111	6	1.41	6.1	0.6768
e080728b:14	8	1.38	6.6	0.4087
e090303h:117	8	1.41	7.0	0.5936
e090224b:102	8	1.47	8.0	0.5778
e080728l:86	8	1.38	10.2	0.3507
e080728g:81	8	1.38	10.5	0.4309
e090224g:107	8	1.47	19.2	0.2885
e090303b:112	10	1.41	9.2	0.9191
e080728c:12	12	1.38	7.7	0.8897
e090224c:103	12	1.47	10.8	0.9760
e090303i:118	12	1.41	11.0	1.1675
e080728h:82	12	1.38	11.3	0.6149
e080728m:87	12	1.38	13.3	0.6472
e090224h:108	12	1.47	19.8	0.4916
e090303c:71	14	1.41	12.9	1.2009
e080728d:15	16	1.38	10.2	1.3378
e080728i:83	16	1.38	14.0	0.9503
e090224d:104	16	1.47	14.5	1.3536
e090303j:119	16	1.41	14.9	1.2685
e090303d:113	16	1.41	15.9	1.6098
e080728n:88	16	1.38	16.3	0.8762
e090224i:109	16	1.47	20.4	0.7587
e090303e:114	18	1.41	18.9	1.4959
e080728e:16	20	1.38	11.9	1.5768
e080728j:84	20	1.38	16.4	1.4547
e080728o:89	20	1.38	16.5	1.2655
e090224e:105	20	1.47	17.4	1.7284
e090303f:115	20	1.41	21.7	1.1847
e090224j:110	20	1.47	21.9	0.9748
e090303g:116	22	1.41	23.6	1.0326

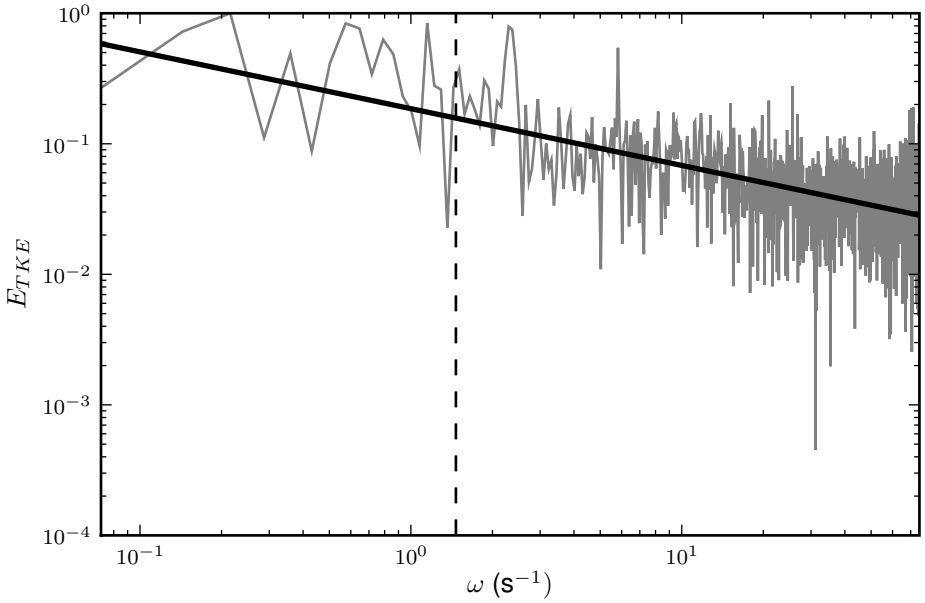

Figure 4.21: Normalized power spectrum of E_{TKE} for e090224h. The solid black line is the least squares fit to the power law $\sim \omega^{-0.43}$. The vertical dashed line is the buoyancy frequency, $N = 1.40$ s^{-1}

to create a composite experiment as shown in figure 4.23. For some experiments, both PIV and SS were set up so that one method could 'take over' from the other to provide as close to simultaneous measurements as possible.

Experiments were performed by varying the belt speed, U, which set the amount of energy that was imparted to the system. Figure 4.24a shows the energy density of the turbulence and the waves as a function of U. Both energy densities increase with U. When wave energy density is plotted as a fraction of turbulent kinetic energy, as in figure 4.24b, it is found that the wave energy density is a rough fraction of the turbulent energy density, namely, $E_{wave}/E_{TKE} = 2.4 \pm 1.4\%$.

4.6 Discussion and conclusions

Internal waves generated by turbulence have been observed in a variety of experimental configurations. This project used a new experimental setup that had a continually forced turbulent shear mixed layer above a stably stratified region. Internal

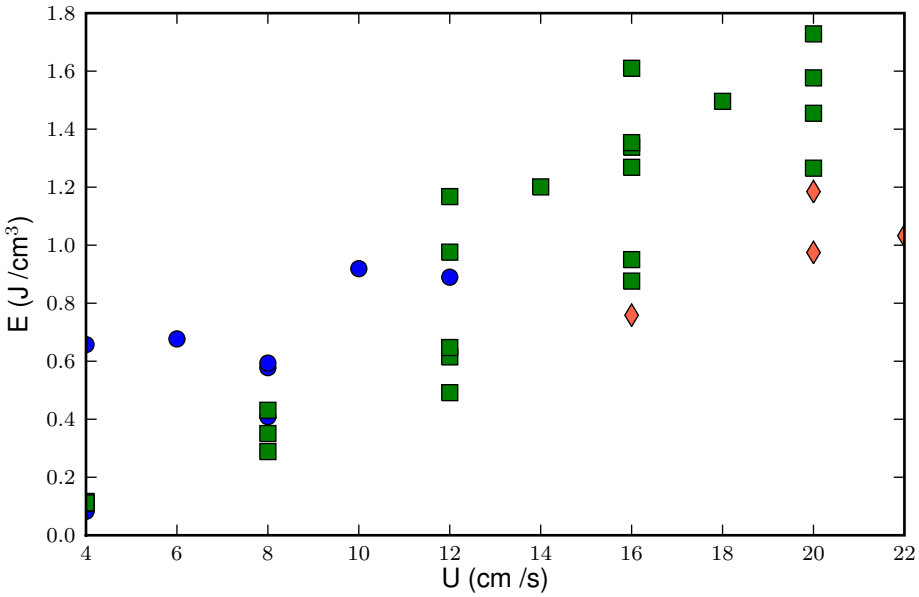

Figure 4.22: Turbulent kinetic energy as a function of belt speed. The blue circles are experiments where the depth of the mixed region is between 0 cm and 10 cm, the green squares between 10 cm and 20 cm, and the red diamonds between 20 cm and 30 cm.

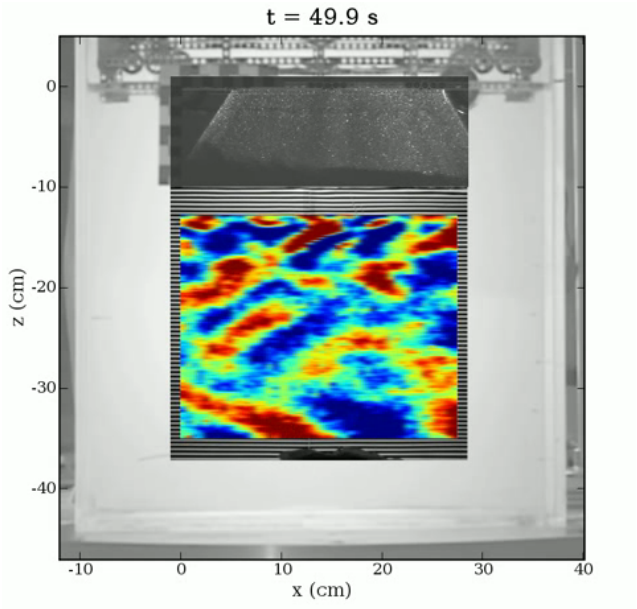

Figure 4.23: Composite image of turbulence and wave visualization methods

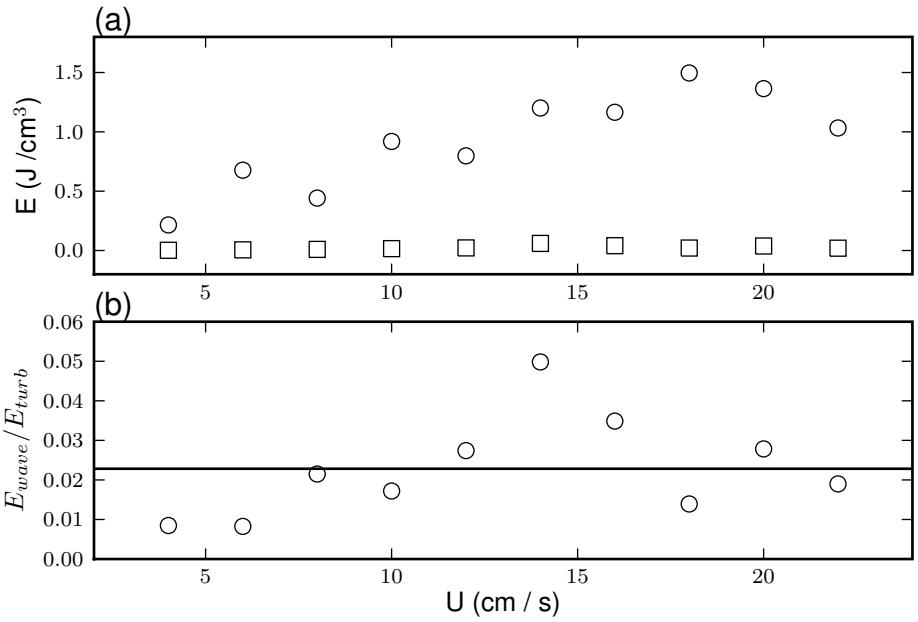

Figure 4.24: Comparison between energy density of mixed layer and stratified layer. The upper panel shows the average energy density grouped by belt speed as a function of belt speed. The lower panel shows the ratio of wave energy to turbulent kinetic energy. The solid black line is the average at 0.024 ± 0.014.

waves were measured in the stratified region. The energetics of both the turbulence and waves have been measured and it was found that wave energy density is a constant fraction of the turbulent energy density. Non-transient waves are generated that are suitable for both spectral analysis and statistical averaging.

Wave energy density is on the order of 1% of the turbulent kinetic energy density. With reference to the motivation given in chapter 1, this suggests that internal wave generation is significant.

There are still several possible concerns with this experimental setup and the subsequent analysis which will need to be resolved before the results can be generalized. First, the experiment is limited to a finite sized tank which sets up a mean circulation in the mixed region and allows for wave reflection off both the side walls and the bottom of the tank. Second, the turbulence measurements are only able to capture two of the three components of the velocity field in the mixed region. Third, it is not known if it will be possible to scale this result up to either an oceanic or atmospheric context. The next chapter describes numerical simulations that address whether the existence of the walls of the tank significantly changes the relationship between the turbulence and the waves.

Chapter 5

Numerical Modelling

5.1 Introduction

The results of chapter 4 suggested that is is possible to characterize the energy of internal waves produced by sheared turbulence as a fixed fraction of the turbulent kinetic energy of the mixed layer. However, the laboratory experiments were limited in a fairly short tank that caused a recirculating flow in the mixed region and wave reflections off the sides and bottom of the tank. In order eventually to apply those results to a geophysical context, it is useful to know limitations of the tank geometry. To address this, direct numerical simulations were performed.

During lab experiments, the turbulence measurements performed using PIV were limited to two dimensions (2-D). In the numerical simulations, the model is run in 2-D mode. Although this will prevent turbulence from fully developing, it will help identify whether the lab experiments are essentially 2-D, as has been assumed, or require a 3-D model. If the 2-D simulations capture the essential observations made in the lab experiments, we can conclude that the wave generation process is essentially 2-D.

The data gathered in the lab was of limited resolution, especially in the turbulent mixed region. Numerical simulations will allow for more detailed information. This is especially useful for analyzing the spectra of both the turbulence and the waves. Also, an energy budget partitioning the energy input in the system into kinetic and potential of both the turbulence and the waves can be performed.

In this chapter the numerical model, Diablo, is described in the remainder of

this section. The setup of the numeric model is given in section 5.2. The turbulence in an upper mixed region is examined in section 5.3. The waves in a lower stratified region are investigated in section 5.4. Results and comparisons between the waves and turbulence are discussed as well as an energy budget in section 5.5. Conclusions and future work are in section 5.7.

5.1.1 Diablo

The software used for numerical modelling is called Diablo. Its name comes from the phrase "Direct numerical simulation In A Box, Laptop Optimized". It has two particular useful features for our research problem. The first is that it can solve the Boussinesq Navier-Stokes equations numerically in two or three dimensions by resolving the smallest turbulent scales. The code also supports a large-eddy simulation (LES) scheme, though this feature was not used in this thesis. The second is that the code is written primarily for the pedagogical purpose of teaching graduate students about computational fluid dynamics (CFD) so it is easier to understand and to modify as compared to other research level CFD codes. In particular, compared to more full-featured software such as global ocean circulation models, there are no physical parametrizations that need to be disabled for a process study such as this. For example, there are no parametrizations of turbulence used, there is no topography to configure, and there are no parametrizations of surface fluxes such as precipitation or solar heating. The code was developed at the University of California, San Diego, by Tom Bewley and John Taylor and has been released under the GNU General Public License. See Taylor (2008) and Bewley (2009) for full details of the software.

The following description is given on its web page:

> Diablo is an open-source, MPI-based, portably efficient, easy-to-read/modify DNS/LES code in Fortran90 syntax for computing turbulence in 3D or 2D rectangular geometries with periodic boundary conditions in 3, 2, 1, or 0 directions and simple Dirichlet, Neumann, or stress-free boundary conditions in the others. It allows for a wide variety of triply periodic, channel, duct, and cavity flows to be studied. Pas-

sive and active scalars may be incorporated to study the effects of density/temperature/salinity/concentration gradients. [1]

5.1.2 Model equations

Diablo solves the incompressible Navier-Stokes equations

$$\frac{\partial \vec{u}}{\partial t} + \vec{u} \cdot \nabla \vec{u} = -\frac{1}{\rho_0} \nabla p' - \frac{g}{\rho_0} \rho' \hat{k} + \nu \nabla^2 \vec{u} \tag{5.1}$$

$$\frac{\partial \rho'}{\partial t} + \vec{u} \cdot \nabla \rho' = \kappa \nabla^2 \rho' \tag{5.2}$$

$$\nabla \cdot \vec{u} = 0 \tag{5.3}$$

where $\vec{u}$ is the velocity vector, ρ_0 is a reference density, p' is the perturbation pressure, rho' is the perturbation density, g is the acceleration due to gravity, ν is the kinematic viscosity, and κ is the mass diffusivity. For our simulations, we have a Schmidt number of Sc $= 1$ meaning that $\kappa = \nu$. The model is developed for either 0, 1, 2, or 3 periodic directions. Here, we used the configuration with 1 periodic direction, which is described in the documentation as the 'duct flow' case. The model is finite difference in the vertical direction and spectral in the horizontal directions.

In the model, the developers refer to the vertical direction as `Y` (e.g. the number of vertical levels is given by `NY`) and the vertical velocity is represented by `V`. However, we will adopt the convention that z is the vertical direction and w is the vertical velocity to be consistent with the laboratory experiments. This renaming has no effect on the results of this chapter but is significant for re-examining the raw output from the model in the future.

5.1.3 Previous work

Diablo was identified as a suitable model to use because of the work done by Taylor and Sarkar (2007). Those authors used Diablo to model a turbulent bottom boundary Ekman layer in a stratified fluid and observed internal waves propagating upwards. Because this was qualitatively similar to the type of simulation we wanted to perform, it suggested that Diablo would be applicable to our particular research problem.

[1] `http://numerical-renaissance.com/Diablo.html`

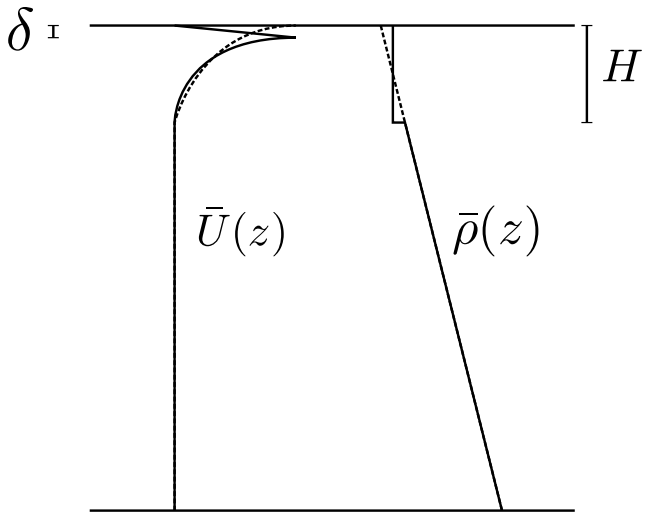

Figure 5.1: The numerical simulation setup. In preliminary designs, the horizontal velocity profile, $\bar{U}(z)$, was originally intended to be like the dashed curve. However, to ensure instability and development of turbulent eddies, a curve similar to the solid line is instead used with a thin frictional layer of thickness δ. See text for further details. The background density profile, $\bar{\rho}(z)$, is a mixed layer of density ρ_{T} and thickness H overlaying a linearly stratified region with density gradient Γ. There is a density jump of $\Delta\rho$ between the mixed and stratified regions.

5.2 Setup

The goal of this thesis is to describe the generation of internal waves by sheared turbulence with application to geophysical flows. The laboratory experiments described in the previous chapter suffer from two major limitations that can be addressed with numerical simulations. The first is the existence of side and bottom walls of the tank. The second is the limited information about the turbulent field that can be obtained using our PIV setup.

In these simulations the goal was to create a horizontally periodic, vertically bounded domain with a rigid upper moving boundary. This is a variation of a classic problem in computational fluid dynamics known as a lid-driven cavity flow (see Shankar and Deshpande (2000) for a review). The laboratory experiments are essentially a lid-driven cavity flow of a stratified fluid.

The numeric setup is detailed in the schematic in figure 5.1. The impulsively started plate, also known as Stokes' first problem (Kundu (1990)), was initially

investigated as a reasonable set of initial conditions. Instability theory, however, can be used to show that this parallel flow is stable to small perturbations (see the next section for further details). A initial flow like a Blasius profile was also considered, which has $U'(0) = U''(0)$ to ensure an inflection point at the boundary. It is possible for this profile go unstable and lead to turbulence. However, in our simulations, only weak instabilities were formed which were quickly damped out by numerical viscosity before turbulence could develop. Furthermore, since there was no energy input into the domain, viscosity would reduce the strength of the flow over time. Blasius flow is usually achieved with a pressure gradient and is used to model the growth of a boundary layer. Instability occurs due to an adverse pressure gradient. The concept of using a pressure gradient in the forcing of the problem led to the eventual initial and boundary conditions chosen.

The initial conditions chosen were

$$u = \varepsilon N(0,1) \tag{5.4}$$

$$w = \varepsilon N(0,1) \tag{5.5}$$

$$\rho = \begin{cases} \rho_T & \text{if } z > -H \\ \rho_T + \Delta\rho + \Gamma(z+H) & \text{if } z < -H \end{cases} \tag{5.6}$$

where the velocity field was initially seeded with noise of amplitude ε from a Gaussian distribution, $N(0,1)$. This velocity field was filtered by the code to ensure that it was divergence-free before the simulation began. The initial stratification was a mixed layer of thickness H overlaying linearly stratified fluid. The density profile was defined by a density in the upper mixed layer, ρ_T, a density jump, $\Delta\rho$, and the linearly stratified layer with constant density gradient, Γ. This profile was chosen to model the stratification observed in the lab experiments.

A pressure gradient given by

$$\frac{dp}{dx}(z) = \begin{cases} \frac{dp}{dx}0 & \text{if } z > -\delta \\ 0 & \text{if } z < -\delta \end{cases} \tag{5.7}$$

forced the system throughout the simulation. A thin horizontal layer of thickness δ at the top of the domain acted as a frictional layer dragging the unforced fluid beneath it. The pressure gradient ensured energy was continually being added to the system. This combination of initial and boundary conditions led to results such

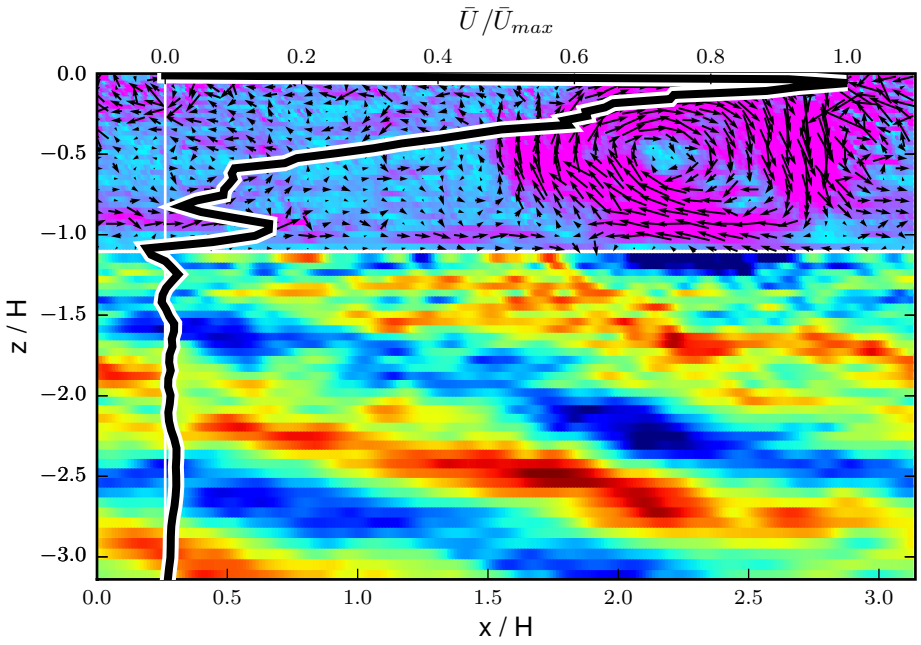

Figure 5.2: An example snapshot of the output of a simulation run. The upper region shows the perturbation velocity field of the mixed layer overlaid on a colour map of the turbulent kinetic energy of the flow. The lower regions shows the vertical displacement field. The solid line is the mean horizontal velocity.

as figure 5.2. Since this was qualitatively similar to what was observed in the lab experiments, with a shear turbulent mixed layer and downward propagating waves in a stratified lower layer, it was deemed sufficiently promising to proceed with further analysis.

5.2.1 Grid

The numerical grid was stretched in the vertical, as depicted in figure 5.3, to allow more points to the turbulent upper region and less to the stratified wave region for a given grid size. It was assumed that the length scales of the turbulence are shorter than that of the waves and thus require higher resolutions to be resolved. Also, we wanted to place the bottom of the domain sufficiently far away that waves reflected off the solid boundary would not come back into the measurement region during the simulation run.

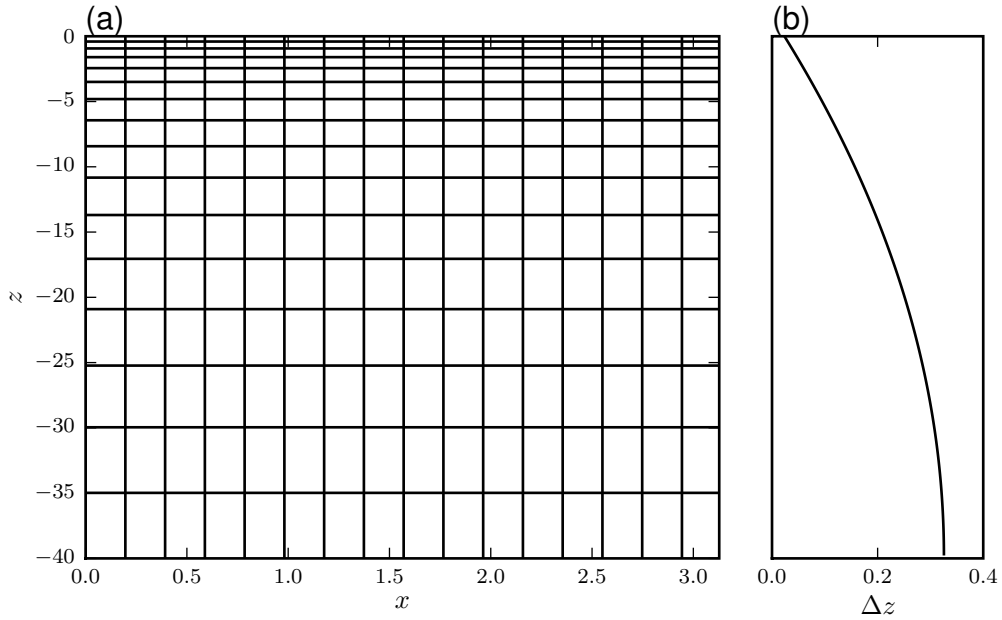

Figure 5.3: Typical (a) grid used for numeric simulation (showing only every 16th grid line) and (b) grid spacing Δz as a function of depth. The vertical grid is stretched according to equation 5.8 so that there are more grid points in the upper turbulent region and less points in the stratified wave region. The grid parameters used are $L_z = 40$, $n_z = 256$, and $CS = 1.0$.

The stretching function used is

$$z[j+1] = L_z(\tanh(CS((2(j-1))/(n_z))) - 1)/\tanh(CS) \tag{5.8}$$

where CS is the grid stretching parameter, L_z is the total height of the domain, and n_z is the number of grid points in the vertical. In the limit as CS goes to 0, the grid becomes uniform in the vertical. For example, a value of $CS = 1.0$ means the grid stretches from $\Delta z = 0.023$ at the top of $\Delta z = 0.326$ at the bottom with $L_z = 40$ and $n_z = 256$.

The coordinate system was defined so that $z = 0$ is the top of the domain and z increasing upwards. A resolution of 256×256 was used with a fixed time step of $\Delta t = 0.0001$. This combination allowed the simulation to converge numerically over the simulation. The domain size was $LX \times LZ = 3.14 \times 40$.

The model output included snapshots of the U, W and ρ fields every $n = 250$ time steps. The model was low-pass filtered after every time step for numeric sta-

Table 5.1: Partial list of parameters for numeric simulations. The full list of parameters is found in the appendix. These are the values used for the base case simulations. Comparisons of the results when these parameters were changed are made in the text.

Parameter	Value or Range
$\frac{dp}{dx}_0$	$-1.0 \ldots -6.0$
δ	0.1
H	1.0
ρ_t	0.5
$\Delta\rho$	0.5
ν	0.0001

bility. Some of the important parameters used are given in table 5.1. A full list of parameters and further information how the model was run is found in the appendix. The simulations were run on the University of Alberta Linux cluster.

5.3 Turbulence

In this section we present some of the observations about the sheared turbulent flow created in the mixed layer.

5.3.1 Laminar flow

In order to model a turbulent flow, a hydrodynamically unstable basic flow was used. As mentioned above, although profiles such as Blasius flow and Couette-Poisson flow were investigated, it was determined that it was difficult to ensure these profiles were unstable and evolved into turbulence. From hydrodynamic instability theory, the velocity profile of a inviscid parallel flow is unstable only if $U''(z) = 0$ somewhere in the flow (Drazin and Reid (1981)). Also, a source of energy was necessary to drive the system and to force continually the turbulence.

Before tackling the turbulent flow, it is useful to understand the nature of the flow under low Reynolds numbers, where viscosity dominates, and the flow is laminar. This laminar flow can be modelled as a Poisson flow in the frictional layer and a start-up Couette flow in the rest of the flow. In particular, using the boundary

conditions

$$u(0) = 0 \tag{5.9}$$

$$\frac{du}{dz}(-\delta) = 0 \tag{5.10}$$

leads to the flow in the frictional layer of

$$u = \frac{1}{2\nu\rho_0}\frac{dp}{dx}(z^2 + 2z\delta) \tag{5.11}$$

assuming steady state.

This simulation is designed to produce strong inflection point in the mean horizontal velocity profile that is hydrodynamically unstable and likely to develop into turbulent flow. The laminar profile also suggests a horizontal velocity scale of

$$U = -\frac{1}{2\nu\rho_0}\frac{dp}{dx}\delta^2. \tag{5.12}$$

A Reynolds number can then be formed as $\mathrm{Re} = \frac{U\delta}{\nu}$. This non-dimensional number, in the absence of buoyancy, determines whether the flow is dominated by viscosity and remains laminar or dominated by inertia and becomes turbulent. Since we desire a turbulent flow, we need to decrease the viscosity, ν, and hence increase Re sufficiently such that the flow becomes turbulent.

Laminar Solution

We can derive a solution to the time dependent mean horizontal velocity if we assume the flow remains laminar. The problem to be solved is

$$\frac{\partial \bar{U}}{\partial t} = -\frac{1}{\rho_0}\frac{dp}{dx} + \nu\frac{d^2\bar{U}}{dz^2} \tag{5.13}$$

$$\bar{U}(z,0) = 0 \tag{5.14}$$

$$\bar{U}(0,t) = 0 \tag{5.15}$$

Note that $\frac{dp}{dx}$ is a piecewise constant function of z. This is an inhomogeneous heat equation with time independent forcing on a semi-infinite domain. The solution is given by

$$\bar{U}(z,t) = \int_0^t \int_0^\delta \frac{1}{\sqrt{4\pi\nu(t-s)}} \times \left(\exp\left(-\frac{(z+\eta)^2}{4\nu(t-s)}\right) - \exp\left(-\frac{(z-\eta)^2}{4\nu(t-s)}\right)\right)\left(-\frac{1}{\rho_0}\frac{dp}{dx}_0\right) d\eta ds \tag{5.16}$$

Although the inner integral can be expressed in terms of error functions, the outer internal needs to be evaluated numerically.

Plots of the theoretical laminar velocity profile are shown in figure 5.4. When compared with the results of a purely laminar flow (figure 5.5a), qualitatively the mean flow develops similarly.

5.3.2 Instability

When viscosity is reduced, the flow developed instabilities and became turbulent. As shown in figure 5.5b, for this run the instability occurred at $t = 3$. Rather than momentum diffusing slowly downwards, it was turbulently mixed quickly to the bottom of the mixed layer. The density jump at the base of the mixed layer prevented the mixed region from continuing to grow significantly over the duration of the simulation.

5.3.3 Analysis

The horizontal mean of the horizontal velocity was computed as $\bar{U}(z,t)$. The perturbation horizontal velocity was defined as $u = U - \bar{U}$. The perturbation vertical velocity was the same as the total vertical velocity, $w = W$.

The energy content of the turbulence was quantified by computing the turbulent kinetic energy density using

$$E = \int_{-H+0.1}^{-\delta-0.1} \int_{0}^{L_x} \frac{1}{2}\rho_0 \frac{H-0.2}{L_x}(u^2+w^2)dxdz \tag{5.17}$$

This density was computed over the vertical region $-H+0.1 < z < -\delta-0.1$. This region was away from both the interface and the upper frictional layer. The energy was averaged over that area to compute a turbulent kinetic energy density. The density was computed each of $5 < t < 20$ and then averaged to get a representative value for E_{TKE}. The starting time of $t = 5$ was chosen to let the instability develop and turbulent eddies fill the mixed region. The same procedure was used in the conveyor belt laboratory experiment to quantify the turbulent kinetic energy.

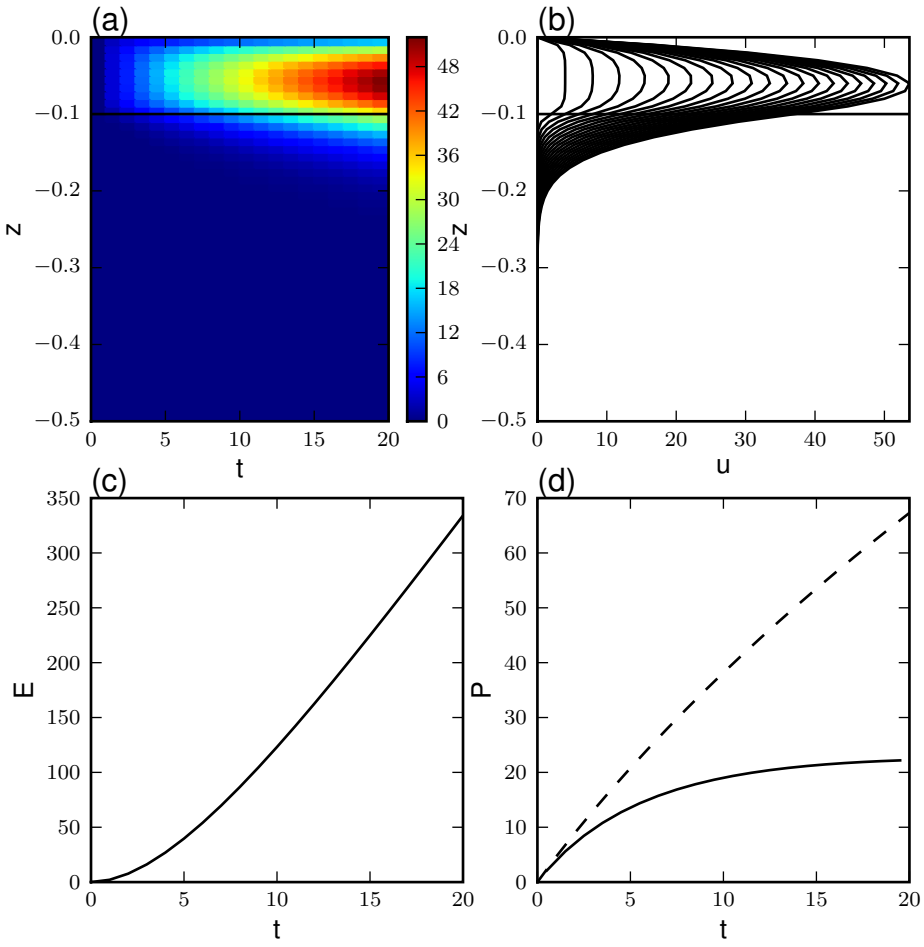

Figure 5.4: Evolution of horizontal velocity based on laminar flow and molecular diffusion of momentum. a) Time series for horizontal velocity, b) velocity profiles at $\Delta t = 1$ intervals, c) Total energy as function of time d) Power input due to pressure field based on $-udp/dx$ term shown as a dashed line while the actual rate of change of energy is shown as a solid line.

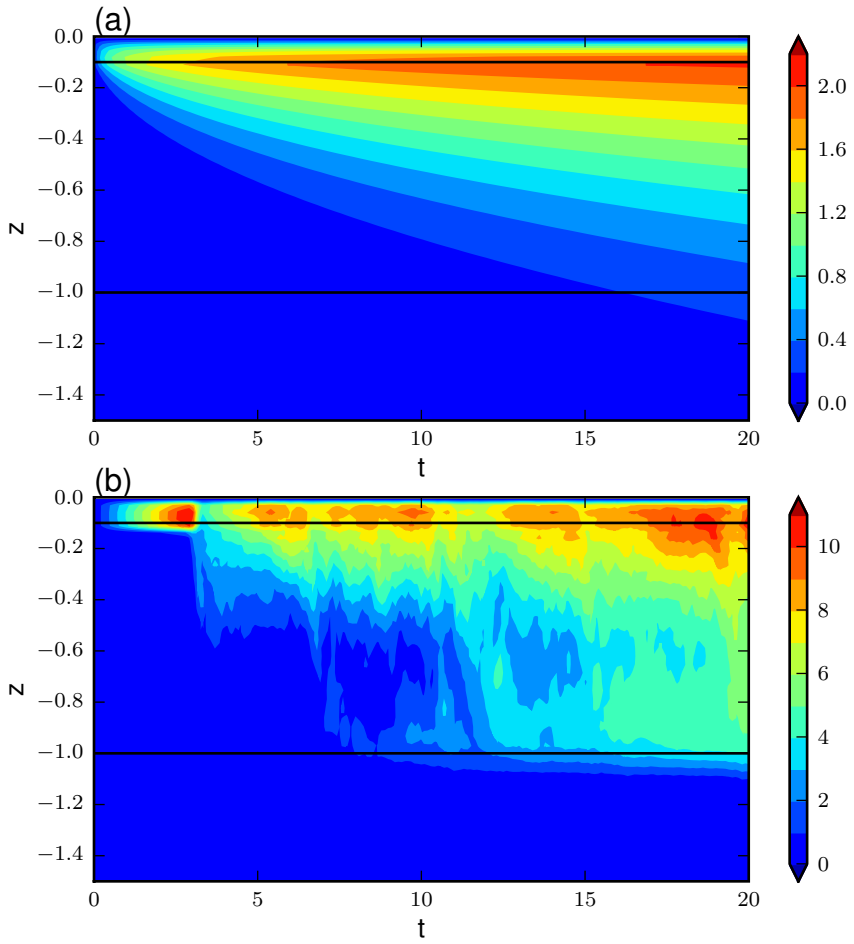

Figure 5.5: Horizontally averaged velocity as a function of depth, z, and time, t. The upper horizontal line marks the thickness δ of the frictional layer and the lower horizontal line marks the position bottom of the mixed region. (a) The viscosity is $\nu = 0.01$ and the flow remains laminar but when (b) $\nu = 0.0001$, the flow goes turbulent at $t = 3$. In both cases, $PX0 = -4.0$.

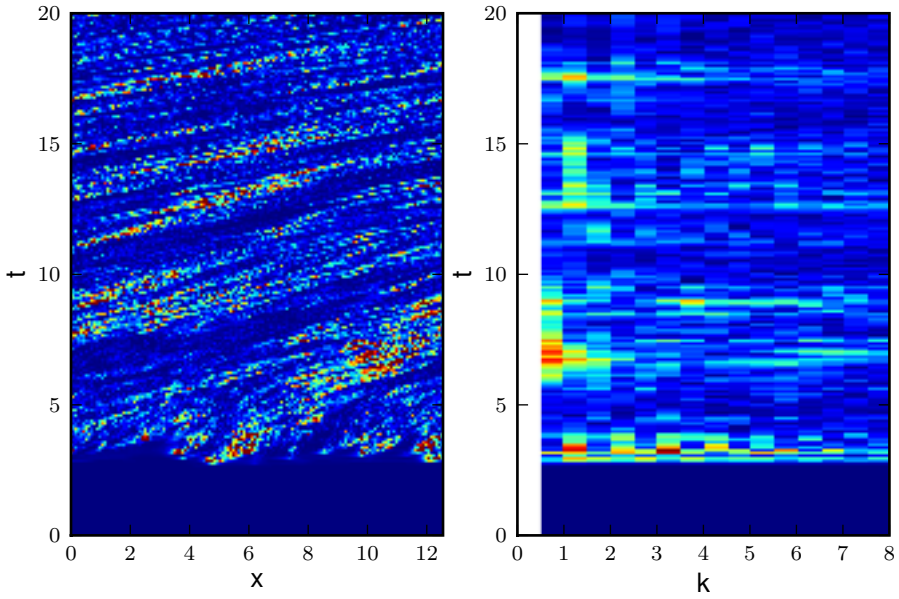

Figure 5.6: (a) Horizontal time series of the turbulent kinetic energy at $z = 0.5$. (b) Fourier transform of (a) in the x-direction.

5.3.4 Spectrum

Turbulence distributes energy over a range of scales. Since this was a 2-D simulation, we expected the energy to cascade up from smaller wave numbers to larger wave numbers. Figure 5.6 shows a horizontal time series of the mixed layer along with its Fourier transform in x. In order to resolve the horizontal wave number a horizontal domain size of $LX = 4\pi$ was used for this one run while keeping the horizontal resolution the same. The eddies can be seen to move from left to right in the direction of the background mean flow. The flow accelerates over time which is why the slope of the eddies in the horizontal time series decreases with time. The spectrum shows that at early times the eddies are distributed over a range of horizontal scales. Soon, however, most of the energy was distributed primarily at fairly small wave numbers.

5.4 Waves

Although the vertical displacement field, ξ, is not an explicit variable in the numerical model, it can be determined from the density field, ρ. The horizontal mean of the density field is denoted as $\bar{\rho}(z,t)$. The background density field was a function of time since the mixed layer was slowly deepening during the simulation. We define ξ implicitly according to

$$\rho(x,z,t) = \bar{\rho}(z + \xi(x,z,t), t) \tag{5.18}$$

A Taylor series expansion gives

$$\rho(x,z,t) = \bar{\rho}(z,t) + \xi(x,z,t) d\bar{\rho}/dz \tag{5.19}$$

Well below the mixed layer where we measure the waves, we assumed the density gradient remains the same as in the initial conditions, $d\bar{\rho}/dz = \Gamma$. Therefore,

$$\xi(x,z,t) = (\rho(x,z,t) - d\bar{\rho}(z,t))/\Gamma \tag{5.20}$$

The wave field was analyzed by constructing horizontal time series at a fixed vertical position as in figure 5.7. The energy density was computed, using the method described for the conveyor belt laboratory experiments, by integrating over all frequencies and wave numbers. The process was repeated at several vertical positions, $-H - 8 < z < -H - 1$ and the average taken to give a representative value for the energy density of the wave field. The wave spectrum based on the horizontal time series can also give the dominant frequency and wave number of the wave field. This is determined by the position of the largest peak in the spectrum.

5.5 Results

5.5.1 Wave properties

By plotting the dominant frequency as a function of $|PX0|$, the dependence of the waves on the forcing is observed. Figure 5.8 shows that as $|PX0|$ increases, the frequency of the waves increases. Doubling the thickness of the mixed layer decreases the frequency of the waves. With the default resolution of $LX = 3.14$,

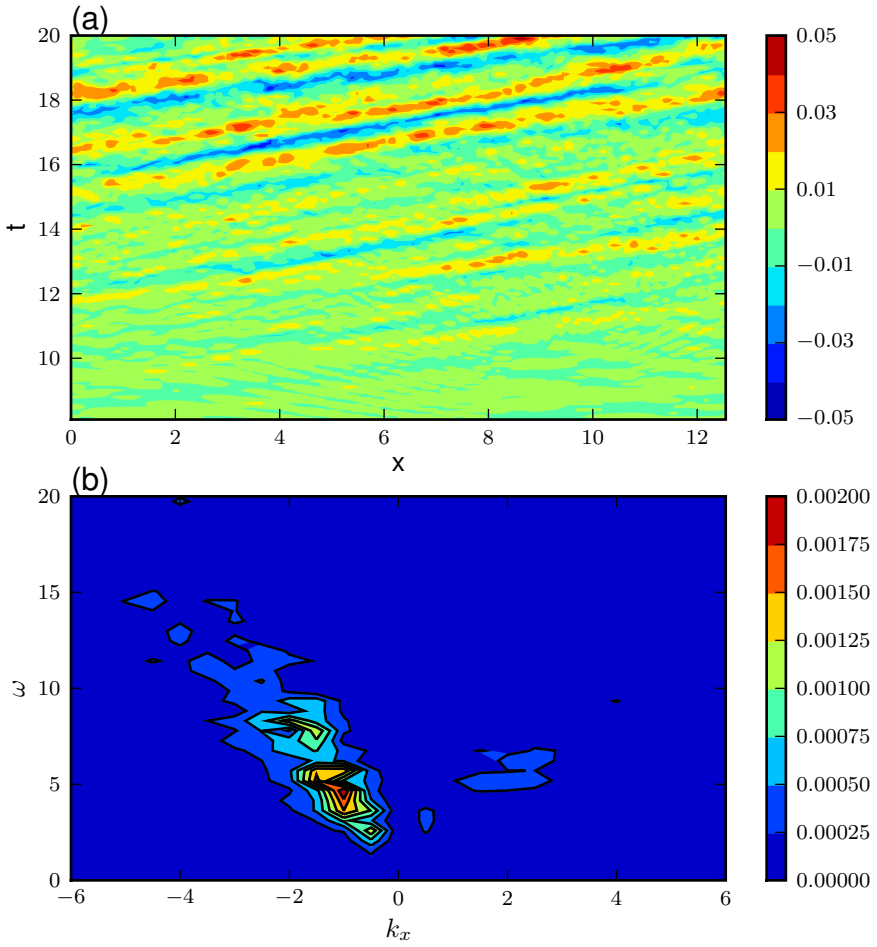

Figure 5.7: Example of (a) horizontal time series at $z = -6.0$ of the vertical displacement field, ξ and (b) the power spectrum of the same field. Note the strong peak in the spectrum indicating that the wave field is dominated by a particular frequency and wave number.

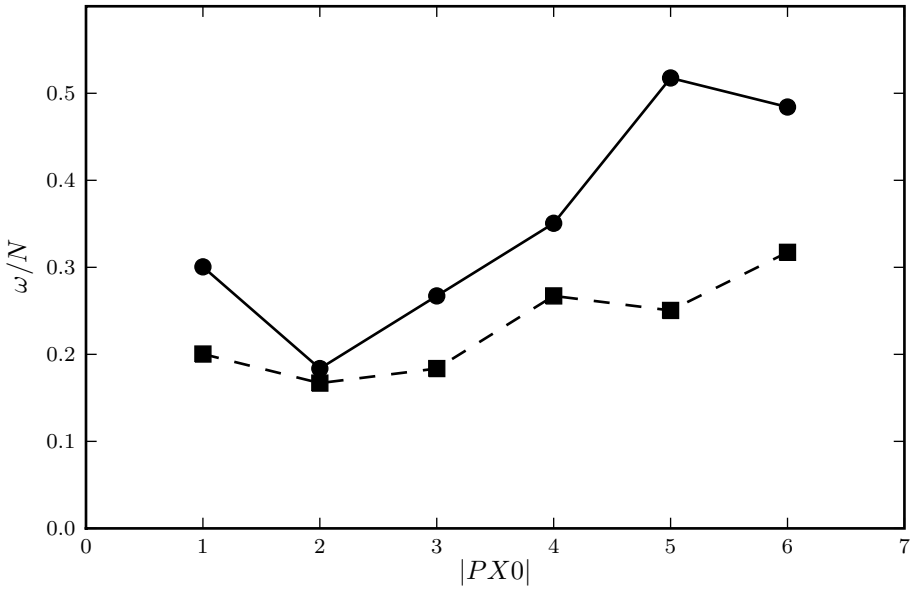

Figure 5.8: Dominant frequency ω of the internal waves based on the spectrum of the horizontal time series at $z = -H - 5$. The forcing $|PX0|$ is varied between simulations. The solid line shows the control case with $H = 1$ while the dashed line is with $H = 2$.

the dominant value of the wave number cannot be determined with a resolution better than $\Delta k_x = 2$. For all values of $|PX0|$ and H simulated, the dominant value of wave number found was $k_x = -2$. To investigate the horizontal number dependence in more detail, two additional simulations were performed with $L_x = 12.56$ and $n_x = 1024$ which maintained the same horizontal resolution. This allows the wave number to be resolved to a resolution of $\Delta k_x = 0.5$. For this pair of simulations, $PX0 = -4$ and the mixed layer thickness was set to $H = 1$ and $H = 2$. For the first experiment, the dominant wave number was at $k_x = -1.5$ and for the second at $k_x = -1.0$. This suggests that as the thickness of the mixed layer is increased, the horizontal wave length of the waves increased.

5.5.2 Energy comparison

In the previous two sections we explored the properties of the turbulence and of the waves in the numerical simulations. Here we combine these two types of analysis

to determine if we can represent the energy of the waves as a constant fraction of the turbulent kinetic energy as was done with the lab experiments in chapter 4.

The energy density of both the turbulent field and the wave field are plotted against the forcing parameter $|PX0|$ as shown in figure 5.9a. As a ratio, they are plotted in figure 5.9b. On average, this ratio is 3%. However, the ratio of E_{wave}/E_{TKE} is increasing with $|PX0|$ (figure 5.9b).

5.5.3 Energy partition

Because we have information about the entire domain we are also able to construct an energy budget. This is more complicated than simply characterizing the energy in terms of kinetic and potential energy. As described in Winters et al. (1995), it is important to distinguish between reversible perturbations of the density field to waves and non-reversible changes due to mixing. For our purposes, we also need to distinguish between the energy in the turbulent mixed layer and the wave dominated stratified layer.

We divide the domain into a 'mixed layer' from $z > z*$ where turbulence and mixing dominate and a 'stratified layer' ($z* > z > z_{bottom}$) where waves dominate. A value of $z* = -H - 1$, one unit below the mixed region was chosen. Using $z* = -H$ is a poor choice because the turbulent kinetic energy dominates the wave field near $z = -H$ and it was difficult to separate the two. Also the mixed layer will deepen over time and not remain at a thickness of H.

Since the system was being continually forced, the total amount of energy in the system was always increasing over time. Unlike the experiments presented in chapter 4, the mean flow does not reach a balance between energy input and viscous dissipation. We computed the energy input by integrating the energy equation in time.

$$E(t) = -\rho_0 \int_{\delta}^{0} U(z,t) \frac{dp}{dx} dz \tag{5.21}$$

The pressure gradient was a known parameter in the frictional layer of thickness δ and the mean horizontal velocity, $U(z,t)$, was taken from the output of the simulation.

The energy that entered the system was partitioned into the kinetic energy of

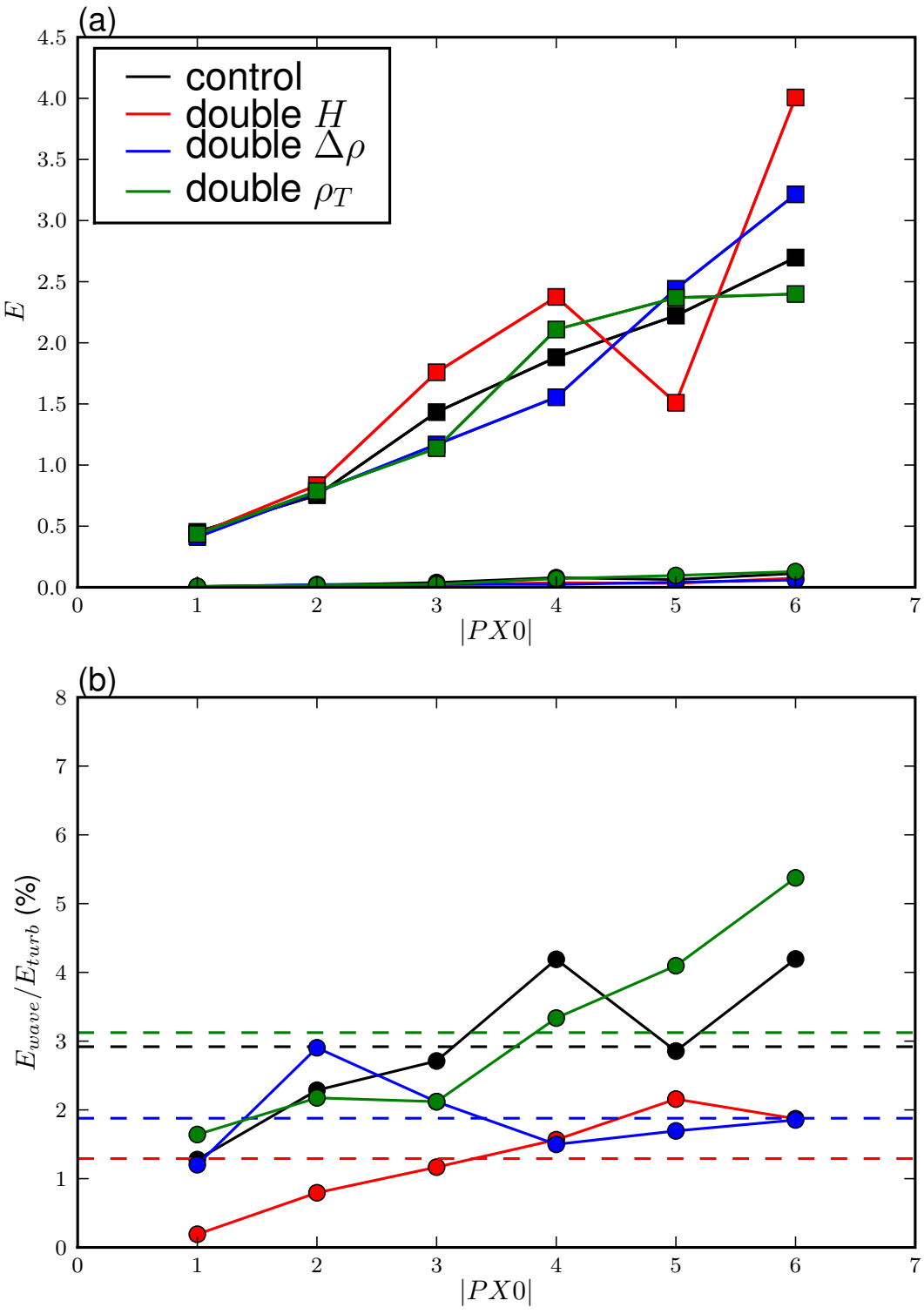

Figure 5.9: Summary of energy measurements over several experiments. The black line represents the 'control' simulation and the coloured lines are simulations where one of the parameters, as indicated by the inset legend, have been changed. (a) Energy of the turbulence (squares) and the waves (circles) plotted against PX0 (b) Ratio E_{wave}/E_{turb} plotted against PX0. The dashed horizontal line shows the average.

the mean flow, the turbulent kinetic energy, the change in potential energy due to diabatic processes (mixing), changes in potential energy due to adiabatic processes (stirring) and interfacial waves, the kinetic and potential energy of the internal waves, and the increase of the internal energy due to dissipation by viscosity.

The mean kinetic energy was given by

$$Ek_{mean}(t) = \frac{1}{2}\rho_0 \int \int_{z_{bottom}}^{0} \bar{U}(z,t)^2 dzdx \tag{5.22}$$

This term captures the background horizontal flow which was continually being accelerated throughout the simulation.

As the mean flow went unstable, eddies developed which were measured in terms of the perturbation velocity components. We measured the turbulent kinetic energy by

$$Ek_{mixed}(t) = \frac{1}{2}\rho_0 \int \int_{z*}^{0} u'(x,z,t)^2 + w'(x,z,t)^2 dzdx \tag{5.23}$$

This term includes both the energy of the turbulence plus the kinetic energy of the interfacial wave between the mixed region and the stratified region. It also includes a small amount of the internal wave energy which we assume is negligible.

We note from movies of the simulation that the flow was dominated only by internal waves below $z = z*$. Therefore, we can use

$$Ek_{wave}(t) = \frac{1}{2}\rho_0 \int \int_{z_{bottom}}^{z*} u'(x,z,t)^2 + w'(x,z,t)^2 dzdx \tag{5.24}$$

as a measure of the kinetic energy associated with internal waves.

The measurement of the potential energy was slightly more complicated. We needed to be careful about the difference between reversible changes in the density field due to either waves or stirring and non-reversible changes due to mixing of the fluid. Here, we consider mixing to be the effect of molecular diffusivity. A change due to the mixing is given by a change in the available potential energy.

$$\Delta APE(t) = \int \int_{z*}^{0} \left(\bar{\rho}(z,t) - \bar{\rho}(z,0)\right) gz \; dzdx \tag{5.25}$$

The change in potential energy due to stirring of the fluid at the base of the mixed region was calculated as

$$Ep_{mixed}(t) = \int \int_{z*}^{0} \left(\rho(x,z,t) - \bar{\rho}(z,t)\right) gz \; dzdx \tag{5.26}$$

This also includes the potential energy due to the displacement of the interface at the base of the mixed layer.

The potential energy of the internal waves was given by

$$Ep_{wave}(t) = \frac{1}{2}\rho_0 N_0^2 \int \int_{z_{base}}^{z*} \xi(x,z,t)^2 dz dx \tag{5.27}$$

Equipartition of energy into kinetic and potential for waves provides a test to ensure the numerics are valid and the wave energy is being properly computed. We note that in our analysis (figure 5.10) this condition is satisfied. The total internal wave energy is

$$E_{wave}(t) = Ek_{wave}(t) + Ep_{wave}(t) \tag{5.28}$$

The dissipation term was estimated by the difference between the energy input and the terms already accounted for in the energy budget.

Figure 5.10 presents the energy terms as a function of time for a simulation with $PX0 = -4$. Figure 5.10a shows the energy input in absolute units partitioned into each of the energy terms described above while figure 5.10b shows the relative distribution of energy as a percentage of the total at any one time. The total energy increased quadratically up until about $t = 3$ when instabilities set in and then grew approximately linearly. In the initial acceleration phase, the energy was partitioned into approximately 80% going to the mean flow and 20% going to dissipation. When the instabilities kicked in, energy quickly transferred from the mean flow, Ek_{mean}, to the eddies in the mixed layer, Ek_{mixed}. Soon afterwards, the kinetic energy of the eddies began to be converted into two types of potential energy changes. The first was non-reversible changes in potential energy (labelled as 'mixing') by deepening of the mixed layer into the stratified layer. The second was into reversible changes in potential energy (labelled 'stirring') by the lifting up of denser fluid parcels into the mixed layer and the forcing of interfacial waves on the density jump between the mixed layer and stratified region. Concurrently, internal waves were being generated and propagating down into the stratified region. Past $t = 13$, the rates of change of each energy category are in equilibrium with each other according to figure 5.10b where the relative proportion were approximately constant.

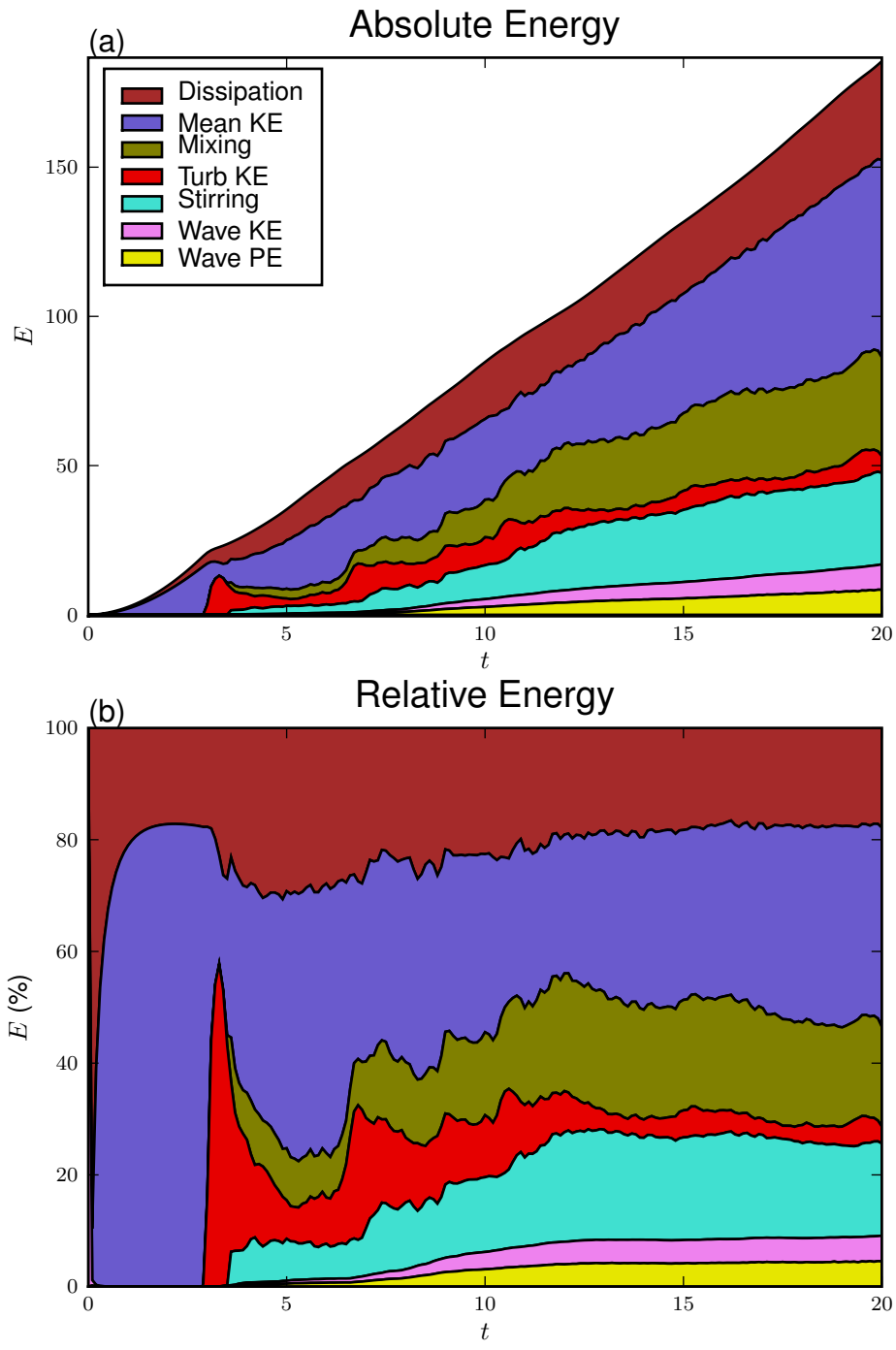

Figure 5.10: Energy versus time. In (a) the energy of each partition is plotted in absolute units as a stacked plot where the thickness of each region shows the amount of energy while in (b) the energy of each partition is shown as a relative fraction of the total energy input.

From figure 5.10, we can estimate the rate of growth and relative distribution of each energy category as fraction of the total energy input. We can use the differences in rates between the energy terms to compute an energy budget as shown in figure 5.11. The inspiration for this type of budget was drawn from figure 5 of Wunsch and Ferrari (2004) showing a 'strawman' energy budget for the ocean. The arrows show the power going into and out of each energy category and the percentages indicate the average relative proportion over the interval $13 < t < 20$. The power input into the system was 10.5 (here, power represents units of energy per unit time per unit width). Of that, a power of 5.8 or roughly half is transferred into turbulent motions. The mean flow continues to accelerate which is why the arrows into and out of this box do not balance. The mean flow accounts for 33% of the total energy input. Our assumption is that the connection between the mean background flow and the other energy categories is only through the turbulent motions of the mixed layer. We infer from figure 5.10a that a constant rate of change occurs in the dissipation, mixing, stirring, turbulent kinetic, and internal wave energy terms. In particular, a power of 1.0 is estimated coming from the turbulent motions to the internal wave field. Thus, after the system has established equilibrium, we conclude that 1.0/10.5 or on the order of 10% of the energy input is being converted into internal waves and radiated away.

5.6 Discussion

The results described above establish a control set of experiments with $PX0 = -1, -2, -3, -4, -5, -6$ to which comparisons can be made by changing some of the parameters.

First, we tested whether the doubling the mixed layer thickness changes the dominant horizontal wave number of the waves. The width of the domain sets the limit of resolution of the horizontal wave number. The control case domain width of π is insufficient to test the change. Therefore, simulations were ran with a horizontal domain size of 4π and the same horizontal resolution to increase the resolvable wave number. This was done for both a mixed depth of 1 and a mixed

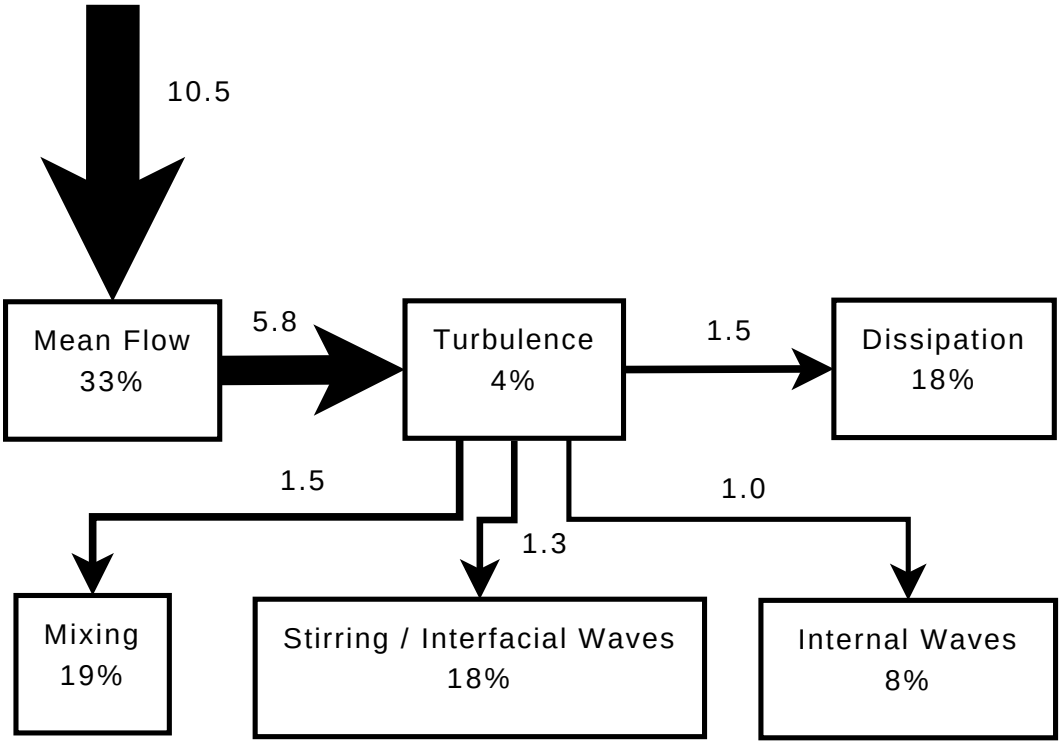

Figure 5.11: Energy budget for the entire system. The width of the arrows and the numbers beside them indicate the power (energy per unit time per unit width) transferred between energy states. The boxes indicate how the energy has been partitioned and the percentages indicated the fraction of total input energy allocated to each partition.

depth of 2. It was determined that doubling the mixed depth significantly shifted the dominant horizontal wave number of the waves closer to zero.

Quadrupling the domain size, as in the previous paragraph, may have impacted the energy density of either the turbulence or the waves. However, by comparing the results with a graph like figure 5.9 (not shown), changes to the horizontal domain size had no substantial affect on the energy density.

Doubling both the vertical and horizontal resolution to a grid of 512×512 produced essentially the same results as given in figure 5.9 (not shown). This indicates that the chosen grid resolution of 256×256 is likely sufficient for resolving the energy containing scales of motion. With regards to computational efficiency, the standard resolution case took approximately 4 hours to complete a single run while the high resolution case took 28 hours for the same set of parameters.

Movies of the evolution of the wave field and the turbulent field show that the wave packets are launched when an eddy hits the interface. If the vortex hits the interface straight down, waves are launched to both the left and right. If the eddy hits the interface while being carried along in the direction of the mean flow, only the waves propagating in the same direction are observed.

The density of the mixed layer is used to establish, via equation 5.6, the density of the entire fluid. When the density ρ_{T} was doubled while keeping the density jump and density gradient the same, the energy of both the turbulence and waves did not substantially change. However, doubling the thickness of the mixed layer increased the size of the eddies. The energy ratio between the waves and the turbulence is decreased by increasing the size of the mixed layer. Doubling the density jump also decreased the energy ratio but to a lesser extent than doubling the mixed layer thickness. The turbulent energy density does not depend on the thickness of the mixed layer nor the density jump. These results are shown in figure 5.9.

5.7 Conclusions

The numerical simulations examined a turbulent mean flow above a stably stratified region in a horizontal periodic domain. We observed the ratio of the wave energy

density to the turbulent kinetic energy density is typically in the range of 1% to 3% which is comparable to results obtained in the laboratory experiments of chapter 4. Furthermore, the power input into the internal wave field is on the order of 10% of the energy input into the system.

5.7.1 Laboratory versus numerical models

The numerical simulations presented in this chapter were designed to interpret the results of the conveyor belt experiments in chapter 4. Qualitatively, as shown by comparing figures 4.23 and 5.2, both show a turbulent eddy field in a mixed region and internal waves propagating downwards.

All of the variables in the numerical simulation were collected and analyzed to describe the state of the system at any time. Also, direct tests of the effect of changing different parameters on the system were made. In these ways, numerical simulations were beneficial for supplementing the results of laboratory studies.

In each of these two studies, the wave energy density was shown to be roughly a fixed fraction of the turbulent kinetic energy density. Since the numerical simulations were only 2-D, this suggests our laboratory experiment was dominated by 2-D processes. Also, since our numerical simulations were in a horizontally periodic and vertically semi-unbounded domain, it suggests that the presence of the tank walls in the laboratory setup were not critical to the results.

5.7.2 Future work

Although the model supports three dimensions, they were too computationally expensive for the purposes of this study, so only the much cheaper two dimensional simulation were performed; since turbulence is inherently three dimensional, we did not simulate a fully developed turbulent flow. Future work includes running the model with three dimensions. We expect that there will be a cascade of energy down to smaller scales as opposed to the instability forming large scale 2-D eddies. This might change the wave numbers of the internal waves generated.

Chapter 6

Conclusion

6.1 Summary of thesis

Wave generation by intrusions, rough topography, and shear turbulence was examined in this thesis. In this section, we summarize the major results.

In chapter 2, we examined the impact of internal waves on the long-term evolution of intrusions using full-depth lock-release experiments. By varying the density of an intrusion we were able to control the vertical position at which the intrusion propagated. After an initial adjustment, the intrusions and the internal waves they generated travelled at a constant speed. For small departures from symmetry, the intrusion speed depended weakly upon intrusion density relative to the ambient fluid density. However, the internal wave speed approximately doubled as the waves changed from having a mode-2 structure when generated by a symmetric intrusion to having a mode-1 structure when generated by an intrusion propagating near the bottom. In the latter circumstance, the interactions between the intrusion and internal waves reflected from the lock-end of the tank were sufficiently strong that the intrusion stopped propagating before reaching the end of the tank. This revealed a significant transfer of available potential energy to the ambient in asymmetric circumstances.

Flow over rough topography, when the speed of the flow is sufficiently fast, generates waves in a relatively narrow frequency band either with or without a mixed layer near the topography. This generation mechanism was explored in chapter 3 with a series of experiments which consisted of a shallow mixed upper layer and

a deep continuously stratified lower layer. A source of turbulence was dragged through the upper layer. Internal waves can freely propagate in the lower layer. The internal waves were measured using synthetic schlieren to determine the frequencies of the generated waves. For sub-critical flow, the frequency was proportional to the flow speed. For super-critical flow, and consistent with previous studies, it was found that the characteristic frequencies of internal waves generated by turbulence are an approximate constant fraction of ≈ 0.7 of the buoyancy frequency.

In chapters 4 and 5 we considered a shear turbulent flow which formed a surface mixed layer above a linear stratified ambient. We used synthetic schlieren for wave measurements and particle image velocimetry for turbulence measurement in the laboratory experiments. The computational experiments were based on 2-D direct numerical simulations. In both laboratory and numerical studies, we found that non-hydrostatic waves were generated with a wave energy density approximately 1% to 3% of the turbulent kinetic energy density of the turbulent mixed layer. If the turbulence was very energetic, say, due to the passage of a storm, the amount of wave energy generated could be relatively significant to the energy budget for internal waves. Our numerical simulations suggested that the internal waves were forced by eddies impacting on the density interface. The horizontal scale of the waves was set by the size of the eddies, which in turn were related to the thickness of the mixed layer, and the time scale was set by the velocity at which the mean flow advects the eddies since the frequency of the waves increased with the speed of the mean flow. Furthermore, in the numerical study, we found that on the order of 10% of the energy input into the system by a surface stress was radiated away by downward propagating internal waves. This suggests that turbulent mean flows are fairly efficient at generating internal waves.

6.2 Significance of results

One of the goals of this research was to motivate the development of a parametrization for general circulation models to capture the net effect of turbulently generated internal waves on mixing.

We know from previous estimates (Wunsch and Ferrari (2004)) that approximately 20 TW of wind power are imparted by surface wind stresses to the upper ocean. The vast majority of this energy ($\approx$ 19TW) is estimated to go into surface waves and turbulence and only 0.6 TW into inertial frequency internal waves. Our laboratory and numerical experiments suggest that on the order of 2% to 10% of energy input by surface stresses on a turbulent mixed layer above a stratified ambient fluid is radiated away by non-hydrostatic internal waves. This implies that on the order of 0.2 TW to 2 TW is transferred to the internal wave field. Since these are high frequency waves, it is expected that most of this wave energy will remain in the thermocline and contribute to upper ocean mixing. Even if this estimate is off by an order of magnitude, it still suggests that the generation of internal waves by turbulence is an important mechanism for energy transport. When analyzing the energy pathways in the ocean, especially for the meridional overturning circulation, the uncertainties are often described in units on the order of 100 GW and so this generation mechanism should be included.

A parametrization of this internal wave generation mechanism still requires much work. In terms of scales, we suspect that the belt speed in the laboratory experiment can be related to the square root of the surface wind stress, the buoyancy in the lab to the stratification in the thermocline, and the depth of the mixed layer to the depth of the ocean mixed layer. The internal waves energy density is a ratio of approximately 2% of the turbulent kinetic energy density. A full parametrization requires more information about the internal waves that were not addressed in this thesis, namely their evolution and where they are likely to break. Also, the stratifications used in both the laboratory and numerical studies were idealized as compared to those found in the ocean. The conclusion of this thesis is that further development of such a parametrization should be pursued.

6.3 Future work

The theory described in Dohan and Sutherland (2005) hypothesized that internal waves generated due to turbulence are narrow banded in frequency because of a

feedback loop of the waves with the largest wave momentum or largest energy momentum on the source. For our sheared turbulent flow experiments and simulations, we did not observe that the dominant frequency was a fixed fraction of the buoyancy frequency. Comparing the numerical and laboratory experiments of the turbulent shear flows, we conjecture that the process of wave generation we observed was dominantly 2-D. The numerical models need to be extended to three dimensions to examine what effect 3-D turbulent structures and a broad frequency spectrum forcing has on the wave field and whether this produces waves of the characteristic frequency that are typically associated with turbulently generated waves.

Further investigation is needed to compare our experiments to the model of Taylor and Sarkar (2007) who suggested that viscosity is responsible for the narrow frequency band of turbulently-generated internal waves They conjecture that since both low and high frequency waves have relatively low vertical group velocities, viscosity has more time to act so only waves close to the maximum vertical group velocity, namely those with $\omega \approx 0.7N$, are observed to propagate away from the turbulent region. This could be experimentally tested by increasing the viscosity of the fluid by adding a high viscosity fluid such as glycerol. However, in our experiments we do not observe a fan of waves indicating a broad range of frequencies near the generation site and more narrowly banded waves further away. Rather, we observe that the wave frequency is set immediately at the turbulent source.

The conveyor belt laboratory experiment would benefit from higher resolution particle image velocimetry or another measurement technique to describe better the turbulence in the mixed layer. We were unable to resolve the small-scale motions of the flow and analyze the turbulence spectrum. Also, since the internal waves are coupled to the turbulent mixed layer, more information about the turbulent eddies immediately at the interface would be useful in explaining the specific mechanism of the wave generation.

Bibliography

D. A. Aguilar. Internal wave generation from stratified flow over finite-amplitude periodic topography. Master's thesis, University of Alberta, 2005.

D. A. Aguilar and B. R. Sutherland. Internal wave generation from rough topography. *Phys. Fluids*, 18, 2006.

R. Amen and T. Maxworthy. The gravitational collapse of a mixed region into a linearly stratified solution. *J. Fluid Mech.*, 96:65–80, 1980.

P. G. Baines. On internal tide generation models. *Deep-Sea Res.*, 29:307–338, 1982.

N. J. Balmforth, G. R. Ierley, and W. R. Young. Tidal conversion by subcritical topography. *J. Phys. Oceanogr.*, 32(10):2900–2914, 2002.

T. H. Bell. Topographically generated internal waves in the open ocean. *Journal of Geophysical Research*, 80(3):320–327, 1975.

T. B. Benjamin. Gravity currents and related phenomena. *J. Fluid Mech.*, 31:209–248, 1968.

T. Bewley. *Numerical Renaissance*. Renaissance Press, 2009.

V. K. Birman, E. Meiburg, and M. Ungarish. On gravity currents in stratified ambients. *Physics of Fluids*, 19(8):086602+, 2007.

D. Bolster, H. A. N. G. Alice, and P. F. Linden. The front speed of intrusions into a continuously stratified medium. *Journal of Fluid Mechanics*, 594(-1):369–377, 2008.

P. Bonneton, J. M. Chomaz, and E. J. Hopfinger. Internal waves produced by the turbulent wake of a sphere moving horizontally in a stratified fluid. *Journal of Fluid Mechanics Digital Archive*, 254(-1):23–40, 2006.

R. E. Britter and J. E. Simpson. Experiments on the dynamics of a gravity current head. *J. Fluid Mech.*, 88:223–240, 1978.

R. E. Britter and J. E. Simpson. A note on the structure of the head of an intrusive gravity current. *J. Fluid Mech.*, 112:459–466, 1981.

H. B. Cheong, J. J. P. Kuenen, and P. F. Linden. The front speed of intrusive gravity currents. *J. Fluid Mech.*, 552:1–11, 2006.

S. B. Dalziel. Decay of rotating turbulence: Some particle tracking experiments. *Appl. Sci. Res.*, 49:217–244, 1992.

S. B. Dalziel, M. Carr, J. K. Sveen, and P. A. Davies. Simultaneous synthetic schlieren and piv measurements for internal solitary waves. *Measurement Science and Technology*, 18(3):533–547, March 2007.

P. J. Diamessis, J. A. Domaradzki, and J. S. Hesthaven. A spectral multidomain penalty method model for the simulation of high reynolds number localized incompressible stratified turbulence. *Journal of Computational Physics*, 202(1): 298–322, January 2005.

K. Dohan. *Internal Wave Generation from a Turbulent Mixed Region*. PhD thesis, University of Alberta, 2004.

K. Dohan and B. R. Sutherland. Turbulence time-scales in mixing box experiments. *Expt. Fluids*, 33:709–719, 2002.

K. Dohan and B. R. Sutherland. Internal waves generated from a turbulent mixed region. *Phys. Fluids*, 15:488–498, 2003.

K. Dohan and B. R. Sutherland. Numerical and laboratory generation of internal waves from turbulence. *Dyn. Atmos. Oceans*, 40:43–56, 2005.

P. G. Drazin and W. H. Reid. *Hydrodynamic Stability*. Cambridge University Press, Cambridge, England, 1981.

V. W. Ekman. On dead water. In F. Nansen, editor, *Norwegian North Polar Expedition, 1893-1896, Scientific Results*, volume 5. Longmans, London, 1904.

T. H. Ellison and J. S. Turner. Turbulent entrainment in stratified flows. *Journal of Fluid Mechanics Digital Archive*, 6(03):423–448, 1959.

H. J. S. Fernando. Turbulent mixing in stratified fluids. *Annual Review of Fluid Mechanics*, 23(1):455–493, 1991.

A. Fincham and G. Delerce. Advanced optimization of correlation imaging velocimetry algorithms. *Experiments in Fluids*, 29(7):S013–S022, December 2000.

A. M. Fincham and G. R. Spedding. Low cost, high resolution dpiv for measurement of turbulent fluid flow. *Experiments in Fluids*, 23(6):449–462, December 1997.

M. R. Flynn and P. F. Linden. Intrusive gravity currents. *Journal of Fluid Mechanics*, 568(-1):193–202, 2006.

M. R. Flynn and B. R. Sutherland. Intrusive gravity currents and internal wave generation in stratified fluid. *J. Fluid Mech.*, 514:355–383, 2004.

C. Garrett and E. Kunze. Internal tide generation in the deep ocean. *Annual Review of Fluid Mechanics*, 39(1):57–87, 2007.

C. J. R. Garrett and W. H. Munk. Internal waves in the ocean. *Annu. Rev. Fluid Mech.*, 11:339–369, 1979.

A. E. Gill. *Atmosphere-Ocean Dynamics*, volume 30 of *International Geophysics Series*. Academic Press, New York, 1982.

C. Härtel, E. Meiburg, and F. Necker. Analysis and direct numerical simulation of the flow at a gravity-current head. part 1. flow topology and front speed for slip and no-slip boundaries. *J. Fluid Mech.*, 418:189–212, 2000.

P. Holloway and M. Merrifield. Internal tide generation by seamounts, ridges, and islands. *Journal of Geophysical Research*, 104:25937–25951, 1999.

J. Y. Holyer and H. E. Huppert. Gravity currents entering a two-layer fluid. *J. Fluid. Mech.*, 100:739–767, 1980.

H. E. Huppert and J. E. Simpson. The slumping of gravity currents. *J. Fluid Mech.*, 99:785–799, 1980.

L. Kantha and C. Clayson. On leakage of energy from turbulence to internal waves in the oceanic mixed layer. *Ocean Dynamics*, 57(2):151–156, April 2007.

L. H. Kantha, O. M. Phillips, and R. S. Azad. On turbulent entrainment at a stable density interface. *Journal of Fluid Mechanics*, 79:753+, 1977.

H. Kato and O. M. Phillips. On the penetration of a turbulent layer into stratified fluid. *Journal of Fluid Mechanics Digital Archive*, 37(04):643–655, 1969.

G. H. Keulegan. An experimental study of the motion of saline water from locks into fresh water channels. Technical Report 5168, Nat. Bur. Stand. Rept., 1957.

S. Khatiwala. Generation of internal tides in an ocean of finite depth: Analytical and numerical calculations. *Deep Sea Research I*, 50:3–21, 2003.

J. B. Klemp, R. Rotunno, and W. C. Skamarock. On the dynamics of gravity currents in a channel. *J. Fluid Mech.*, 269:169–198, 1994.

P. K. Kundu. *Fluid Mechanics*. Academic Press, Inc., San Diego, 1990.

J. R. Ledwell, E. Montgomery, K. Polzin, L. C. St. Laurent, R. Schmitt, and J. Toole. Evidence for enhanced mixing over rough topography in the abyssal ocean. *Nature*, 403:179–182, 2000.

P. F. Linden. The deepening of a mixed layer in a stratified fluid. *J. Fluid Mech.*, 71:385–405, 1975.

S. G. Llewellyn Smith and W. R. Young. Tidal conversion at a very steep ridge. *Journal of Fluid Mechanics*, 495(-1):175–191, 2003.

R. R. Long. Some aspects of the flow of stratified fluids. a theoretical investigation. *Tellus*, 5:42–58, 1953.

R. R. Long. Some aspects of the flow of stratified fluids. III Continuous density gradients. *Tellus*, 7:341–357, 1955.

R. J. Lowe, P. F. Linden, and J. W. Rottman. A laboratory study of the velocity structure in an intrusive gravity current. *J. Fluid Mech.*, 456:33–48, 2002.

P. C. Manins. Intrusion into a stratified media. *J. Fluid Mech.*, 74:547–560, 1976.

J. Marshall and F. Schott. Open-ocean convection: Observations, theory, and models. *Reviews of Geophysics*, 37(1):null+, 1999.

T. Maxworthy, J. Leilich, J. Simpson, and E. H. Meiburg. The propagation of a gravity current in a linearly stratified fluid. *J. Fluid Mech.*, 453:371–394, 2002.

M. E. Michaelian, T. Maxworthy, and L. G. Redekopp. The coupling between turbulent, penetrative convection and internal waves. *Eur. J. Mech. B*, 21:1–28, 2002.

J. J. Monaghan. Gravity current interaction with interfaces. *Annual Review of Fluid Mechanics*, 39(1):245–261, 2007.

D. E. Mowbray and B. S. H. Rarity. A theoretical and experimental investigation of the phase configuration of internal waves of small amplitude in a density stratified liquid. *J. Fluid Mech.*, 28:1–16, 1967a.

W. H. Munk and C. Wunsch. Abyssal recipes II: Energetics of tidal and wind mixing. *Deep-Sea Res.*, 45:1977–2010, 1998.

J. R. Munroe and K. G. Lamb. Topographic amplitude dependence of internal wave generation by tidal forcing over idealized three-dimensional topography. *Journal of Geophysical Research*, 110:C02001+, February 2005.

J. R. Munroe and B. R. Sutherland. Generation of internal waves by sheared turbulence: experiments. *Environmental Fluid Mechanics*, 8(5-6):527–534, September 2008.

J. R. Munroe, B. R. Sutherland, C. Voegeli, V. Birman, and E. H. Meiburg. Gravity currents intruding into a uniformly stratified ambient. *Journal of Fluid Mechanics*, 635:245–273, 2009.

S. Narimousa and H. J. S. Fernando. On the sheared density interface of an entraining stratified fluid. *Journal of Fluid Mechanics Digital Archive*, 174(-1):1–22, 1987.

G. Oster. Density gradients. *Sci. Am.*, 213, 1965.

K. L. Polzin, J. M. Toole, J. R. Ledwell, and R. W. Schmitt. Spatial variability of turbulent mixing in the Abyssal Ocean. *Science*, 276:93–96, 1997.

J. W. Rottman and J. E. Simpson. Gravity currents produced by instantaneous releases of a heavy fluid in a rectangular channel. *J. Fluid Mech.*, 135:95–110, 1983.

H. Rouse and J. Dodu. Turbulent diffusion across a density discontinuity. *La Houille Blanche*, 10:530–532, 1955.

A. H. Schooley and B. A. Hughes. An experimental and theoretical study of internal waves generated by the collapse of a two-dimensional mixed region in a density gradient. *J. Fluid Mech.*, 51:159–175, 1972.

P. N. Shankar and M. D. Deshpande. Fluid mechanics in the driven cavity. *Annual Review of Fluid Mechanics*, 32(1):93–136, 2000.

J. O. Shin, S. B. Dalziel, and P. F. Linden. Gravity currents produced by lock exchange. *J. Fluid Mech.*, 521:1–34, 2004.

I. P. D. D. Silva and H. J. S. Fernando. Experiments on collapsing turbulent regions in stratified fluids. *Journal of Fluid Mechanics*, 358(-1):29–60, 1998.

J. E. Simpson. Effects of lower boundary on the head of a gravity current. *J. Fluid Mech.*, 53:759–768, 1972.

J. E. Simpson. Gravity currents in the laboratory, atmosphere, and ocean. *Ann. Rev. Fluid Mech.*, 14:213–234, 1982.

J. E. Simpson. *Gravity Currents*. Cambridge University Press, Cambridge, England, 2nd edition, 1997.

J. E. Simpson and R. E. Britter. The dynamics of the head of a gravity current advancing over a horizontal surface. *J. Fluid Mech.*, 94:477–495, 1979.

L. S. G. Smith and W. R. Young. Conversion of the barotropic tide. *J. Phys. Oceanogr.*, 32:1554–1566, 2002.

I.-S. Song, H.-Y. Chun, and T. P. Lane. Generation mechanisms of convectively forced internal gravity waves and their propagation to the stratosphere. *Journal of the Atmospheric Sciences*, 60(16):1960–1980, August 2003.

L. St. Laurent, S. Stringer, C. Garrett, and P. D. Joncas. The generation of internal tides at abrupt topography. *Deep Sea Res. I*, 50(8):987–1003, 2003.

C. Staquet and J. Sommeria. Internal gravity waves: From instabilities to turbulence. *Ann. Rev. Fluid Mech.*, 34:559–593, 2002.

B. R. Sutherland and P. F. Linden. Internal wave generation by flow over a thin barrier. *J. Fluid Mech.*, 377:223–252, 1998.

B. R. Sutherland and J. T. Nault. Intrusive gravity currents propagating along thin and thick interfaces. *Journal of Fluid Mechanics*, 586(-1):109–118, 2007.

B. R. Sutherland, S. B. Dalziel, G. O. Hughes, and P. F. Linden. Visualisation and measurement of internal waves by "synthetic schlieren". Part 1: Vertically oscillating cylinder. *J. Fluid Mech.*, 390:93–126, 1999.

B. R. Sutherland, P. J. Kyba, and M. R. Flynn. Interfacial gravity currents in two-layer fluids. *J. Fluid Mech.*, 514:327–353, 2004.

B. R. Sutherland, A. N. F. Chow, and T. P. Pittman. The collapse of a mixed patch in stratified fluid. *Physics of Fluids*, 19(11):116602+, 2007.

J. R. Taylor. *Numerical Simulations of the Stratified Oceanic Bottom Boundary Layer*. PhD thesis, University of California, San Diego, 2008.

J. R. Taylor and S. Sarkar. Internal gravity waves generated by a turbulent bottom ekman layer. *Journal of Fluid Mechanics*, 590:331–354, 2007.

S. A. Thorpe. The excitation, dissipation, and interaction of internal waves in the deep ocean. *J. Geophys. Res.*, 80(3):328–338, 1975.

S. A. Thorpe. Recent developments in the study of ocean turbulence. *Annual Review of Earth and Planetary Sciences*, 32(1):91–109, 2004.

J. S. Turner. The influence of molecular diffusivity on turbulent entrainment across a density interface. *Journal of Fluid Mechanics*, 33(04):639–656, 1968.

M. Ungarish. Intrusive gravity currents in a stratified ambient: shallow-water theory and numerical results. *Journal of Fluid Mechanics*, 535(-1):287–323, 2005.

M. Ungarish. On gravity currents in a linearly stratified ambient: A generalization of Benjamin's steady-state propagation results. *J. Fluid Mech.*, 548:49–68, 2006.

M. Ungarish and H. E. Huppert. On gravity currents propagating at the base of a stratified fluid. *J. Fluid Mech.*, 458:283–301, 2002.

M. Ungarish and H. E. Huppert. On gravity currents propagating at the base of a stratified ambient: effects of geometrical constraints and rotation. *Journal of Fluid Mechanics*, 521(-1):69–104, 2004.

M. Ungarish and H. E. Huppert. Energy balances for propagating gravity currents: homogeneous and stratified ambients. *Journal of Fluid Mechanics*, 565(-1):363–380, 2006.

G. K. Vallis. *Atmospheric and Ocean Fluid Dynamics*. Cambridge University Press, 2006.

J.-S. von Storch, H. Sasaki, and J. Marotzke. Wind-generated power input to the deep ocean: An estimate using a 1/10° general circulation model. *Journal of Physical Oceanography*, 37(3):657–672, March 2007.

M. Watanabe and T. Hibiya. Energetics of wind-induced turbulent mixing in the ocean. *Journal of Oceanography*, 64(1):131–140, February 2008.

K. B. Winters, P. N. Lombard, J. J. Riley, and E. A. D'Asaro. Available potential energy and mixing in density-stratified fluids. *Journal of Fluid Mechanics Digital Archive*, 289(-1):115–128, 1995.

J. Wu. Mixed region collapse with internal wave generation in a density stratified medium. *J. Fluid Mech.*, 35:531–544, 1969.

A. Wüest and A. Lorke. Small-scale hydrodynamics in lakes. *Annual Review of Fluid Mechanics*, 35(1):373–412, 2003.

C. Wunsch and R. Ferrari. Vertical mixing, energy, and general circulation of the oceans. *Annual Review of Fluid Mechanics*, 36:281–314, 2004.

E. Xuequan and E. J. Hopfinger. On mixing across an interface in stably stratified fluid. *Journal of Fluid Mechanics Digital Archive*, 166(-1):227–244, 1986.

Appendix A

Data

A.1 Laboratory experiments

A.1.1 Database

The experimental data is stored in a sqlite3 database called 'igwturbgen.db'. A relational database was chosen to allow the data to be well organized. When this section refers to the 'SQL Database' this is the file that is implied. The table structure is given in Figure A.1 and will be referred to throughout this section.

A useful tool browse the contents of this database is public domain SQLite Database Browser (`http://sqlitebrowser.sourceforge.net`)

A.1.2 Digital video

The central table in this organizational structure is 'dv' which lists all of the digital video clips obtained from experiments. The table specifies the filename, camera type, resolution, frame, and length of clip. Each dv is assigned a 'grid' from the 'grids' table that provides information about the world grid. Also, each dv is assigned to a particular experiment in the 'experiments' table. A particular experiment may be comprised of several pieces of dv if several cameras were used or a single camera was turned on and off repeatedly during an experiment. If the dv_id is in the 'schlieren_dv' table that mean that the clip can be processed using synthetic schlieren and if the dv_id is in the 'piv_dv' table that means that the clip can be processed using particle image velocimetry.

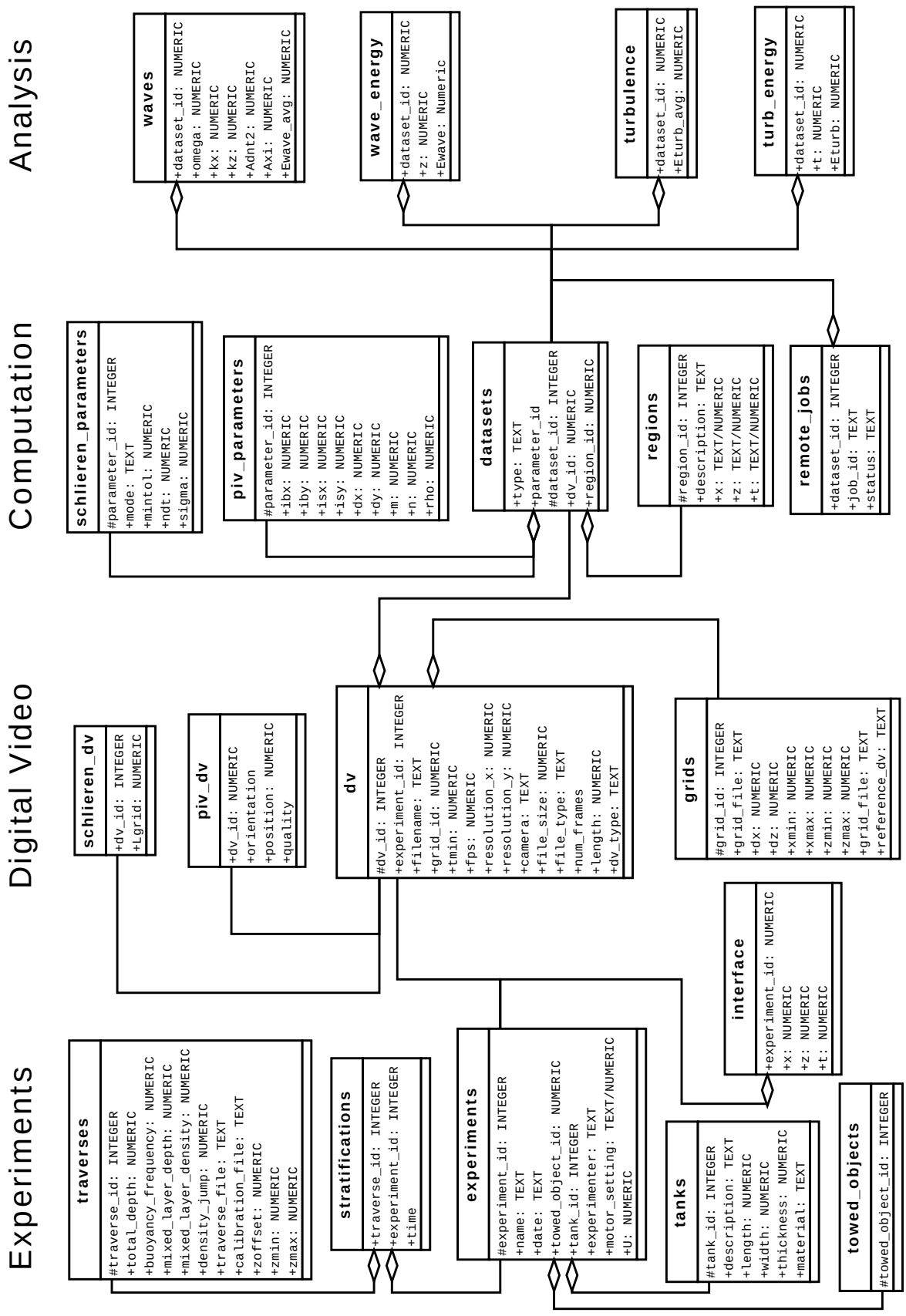

Figure A.1: Database schema for igwturbgen.db

A.1.3 Experiment names

Experiments are identified by the date the data was collected under the naming scheme eYYMMDD[a-z]. For example, the third experiment of the day performed on August 13, 2007 would be called e070813c. Names of the form eYYMMDD are meta-experiments and are used for days where multiple experiments will share some data (such as camera configuration or traverse data). There is a one-to-one correspondence of the experiment name used in the lab book and the experiment_id used in the SQL database.

This system explicitly assumes that there will be no more than 26 experiments on a given day.

A.1.4 World coordinate system

Every experiment has an associated world coordinate system mapping pixel coordinates to a lab reference frame. The vertical coordinate is z (pointing upwards), the along tank coordinate is x (pointing to the right), and the traverse tank coordinate is y (pointing from the front of the tank to the back).

To determine a world coordinate grid, the command line tool *igwgrid* was used which takes an image or digital video clip and presents to the user a graphical editor that allows reference points to be chosen.

For some experiments, a 10 cm by 10 cm L-shaped scale was used as a reference shape in the scene of the experiment.

This information is organized with the the 'grids' table the SQL database.

A.1.5 Stratification measurements

The density stratification for all experiments consists of a uniformly mixed region of density ρ_{mixed} of thickness h_{upper} which is above a linearly stratified region with buoyancy frequency N of thickness h_{lower}. The density jump between the upper and lower layer is denoted by $\Delta\rho$. The total depth of the fluid is given by $H = h_{upper} + h_{lower}$. Any stratification can be described by the parameters $(H, h_{upper}, \rho_{mixed}, \Delta\rho, N)$. Depending on the stratification, it is possible for ρ_{mixed},

$\Delta\rho$, or N to be zero.

The table 'stratifications' stores the values of the stratification parameters along with the traverse that was used to determine these values.

Traverse files are either produced by a *LabView* visual instrument or by hand using spot samples measured by the density meter. These files are saved with the filename `trav[0-9].dat` in a directory of the same name as the corresponding experiment or the name of a group of experiments (e.g. all experiments from the same day). Often, but not always, traverses were taken before and after an experiment. The numerical index of the traverse indicates the order it was taken on that day and/or for that experiment.

The structure of the traverse files is text files with tab separated columns. The first column contains the vertical position, the second contains the calculated density and the third (optional) contains the voltage of the conductivity probe. For traverses based on the conductivity probe there is often a corresponding file called `calibration.dat` listing reference densities and reference voltages.

If calibration data is available, the computed density is recomputed from the voltage data (occasionally, the calibration data entered into *LabView* software was incorrect). If not, the value stored in the traverse is used. Manual traverses determined using the density meter do not have calibration data or voltage data so the density values they contain are used directly.

In development of these experiments, the origin of the vertical position did not always correspond to the origin of the lab reference frame (that is, $z = 0$ for the surface; see section A.1.4 for details on the world coordinate system). There is a value in the 'stratification' table called zoffset which is used for adjusting the vertical position to match the lab reference frame.

The stratification parameters, are computed using a least squares estimation routine. The script performing the estimation is called `traverses.py`. Sometimes it was necessary to restrict the region where the buoyancy frequency was calculated to a subset of the entire traverse. This subinterval is defined by ($zmin$, $zmax$) which is also recorded in the 'stratifications' table if they were used.

The table 'traverses' lists every traverse taken. Traverses are associated with

individual experiments via the 'stratifications' table. It is possible that a single traverse is used for several experiments and likewise that multiple traverses were taken during a single experiment.

A.1.6 Parameters

Different analysis parameters are used for both synthetic schlieren and for particle image velocimetry. See the database tables 'schlieren_parameters' and 'piv_parameters', respectively.

A.1.7 Regions

Often, the entire spatial and temporal domain and resolution captured by a particular digital video clip is not needed to perform analysis. For analysis across multiple experiments, it is preferred that the same domain and resolution is used. Also, there may be dependence on domain size and resolution in the different types of analysis. A region of interest is defined as a rectangular domain in vertical and horizontal space and time interval at a fixed resolution. This region is tagged with a 'region_id' and the information is stored in the 'regions' table of the SQL database.

A.1.8 Datasets

Given a particular digital video clip, a region of interest, and an analysis method with specific parameters a computation is performed. The result of this computation is called a dataset and is tracked with a dataset_id in the table 'datasets' of the SQL database. It is used for the internal accounting of batch computation jobs and identifying the exact computation used to make a particular analysis result.

A.2 Numerical experiments

As described in chapter 5, the numerical code Diablo was used to perform DNS simulations of turbulence and waves.

This section provides some specific details on how the code was modified and how it was run.

A.2.1 Running the model

Diablo takes two parameter files *input.dat* and *input_chat.dat* to control the simulation. And example of each of these are shown in listings A.1 and A.2, respectively.

Listing A.1 input.dat

```
C A data file for Diablo.  This is a generic, easy method of data
C input, as long as you don't change the number of comment lines.
C Note that the grid size is defined in the file grid_def.

C   FLAVOR        VERSION
   'Basic'          1.2
C Parameters:     NU,       LX,    LY,    LZ
                1.0D-5    2.0    2.0    3.14
C Method:     NUM_PER_DIR, CREATE_NEW_FLOW
                  2             .TRUE.
C Time March: N_TIME_STEPS, DELTA_T, RESET_TIME, VARIABLE_DT, CFL, UPDATE_DT
       50000        0.005    .FALSE.      .TRUE.     0.5  1
C I/O:        VERBOSITY, SAVE_FLOW_INT, SAVE_STATS_INT,  MOVIE
                  2          250           250        .FALSE.
C Here include 6*N_TH lines, see below for format
C         CREATE_NEW_TH(1)  Create new field or Read from DIABLO_TH.START
               .TRUE.
C         FILTER_TH(1)         FILTER_INT(1)  (If and how often to filter)
               .TRUE.               1
C         RI_TAU(1)      PR(1)      REACTION(1)     NON_NEG_SCALAR(N)
             -2.0         1.0         0.0          .FALSE.

C When including scalar advection, include 6 lines like the following
C for each scalar

C         CREATE_NEW_TH(1)  Create new field or Read from DIABLO_TH.START
               .TRUE.
C         FILTER_TH(1)         FILTER_INT(1)  (If and how often to filter)
               .TRUE.               10
C         RI_TAU(1)      PR(1)          REACTION(N)     NON_NEG_SCALAR(N)
             0.0             1.0          0.0       .FALSE.
```

A.2.2 Code modifications

A copy of the Diablo source code was obtained in October 2008 from `http://numerical-renaissance.com/Diablo.html` and few a modifications were made as explained here.

Listing A.3 shows the code snippet added that controls the external forcing that drives the simulation. This code was added as part of the time stepping subroutine `RK2` along the a new forcing type `F_TYPE = 3`.

The density profile is initialized the subroutine `CREATE_TH` with a mixed layer overlaying a linear stratified region. The specific function used is given in listing A.4. The velocity profile is initialized in the subroutine `CREATE_FLOW` with

Listing A.2 input_chan.dat

```
C A data file for diablo.  This is a generic, easy method of data
C input, as long as you don't change the number of comment lines.
C Note that the grid size is defined in the file grid_def.
C VERSION
   1.2
C TIME_AD_METH
      2
C LES:   LES_MODEL_TYPE (IF USING LES IN SIMULATION.....)
               2
C ICs:    IC_TYPE,    KICK
             5       0.001
C Forcing:      F_TYPE,    UBULK0,   PX0,    OMEGA0,   AMP_OMEGA0
                  3         0.0      -0.04    6.28       0.1
C BCs: U_BC_YMIN, U_BC_YMIN_C1, U_BC_YMIN_C2, U_BC_YMIN_C3
           0          0.0             0.0           0.0
C BCs: V_BC_YMIN, V_BC_YMIN_C1, V_BC_YMIN_C2, V_BC_YMIN_C3
           0          0.0             0.0           0.0
C BCs: W_BC_YMIN, W_BC_YMIN_C1, W_BC_YMIN_C2, W_BC_YMIN_C3
           0          0.0             0.0           0.0
C BCs: U_BC_YMAX, U_BC_YMAX_C1, U_BC_YMAX_C2, U_BC_YMAX_C3
           1          0.0             0.0           0.1
C BCs: V_BC_YMAX, V_BC_YMAX_C1, V_BC_YMAX_C2, V_BC_YMAX_C3
           0          0.0             0.0           0.0
C BCs: W_BC_YMAX, W_BC_YMAX_C1, W_BC_YMAX_C2, W_BC_YMAX_C3
           0          0.0             0.0           0.0
C Here include 4*N_TH lines, see below for format
C BCs: TH_BC_YMIN(1), TH_BC_YMIN_C1(1), TH_BC_YMIN_C2(1), TH_BC_YMIN_C3(1)
           1                 0.0             -1.00           0.50
C BCs: TH_BC_YMAX(1), TH_BC_YMAX_C1(1), TH_BC_YMAX_C2(1), TH_BC_YMAX_C3(1)
           1                 0.0              0.50           1.00

C Description
C For channel flows (NUM_PER_DIR=2):
C IC_TYPE specifies the functional form for the initial velocity
C KICK is a scale factor on the noise added when creating a new flow.
C F_TYPE=0 gives constant mass flux flow (maintaining UBULK0).
C F_TYPE=1 gives constant pressure gradient flow (PX0 constant).
C F_TYPE=2 is for an oscillatory pressure gradient of the form:
C            PX0+AMP_OMEGA0*cos(OMEGA0*TIME)
C U_BC_YMIN is the BC TYPE on the U velocity component at the lower wall
C    (0 for Dirichlet, 1 for Neumann)
C U_BC_YMIN_C1 is the value of the velocity (if Dirichlet) or it's
C   gradient (if Neumann)

C When including scalar advection, include 4 lines like the following for
C each scalar

C BCs: TH_BC_YMIN(1), TH_BC_YMIN_C1(1), TH_BC_YMIN_C2(1), TH_BC_YMIN_C3(1)
           1           0.0             0.0           0.0
C BCs: TH_BC_YMAX(1), TH_BC_YMAX_C1(1), TH_BC_YMAX_C2(1), TH_BC_YMAX_C3(1)
           1           0.0             0.0           0.0
```

Listing A.3 Pressure forcing

```
     ELSE IF (F_TYPE.EQ.3) THEN
         ! Adverse pressure gradient in boundary layer
         DO J=JSTART,JEND
             IF(GYF(J).GT.(LY/2.0-U_BC_YMAX_C3)) THEN
                 CR1(0,0,J)=CR1(0,0,J)-TEMP4*PX0
             END IF
         END DO
```

Gaussian white noise of an amplitude given by `KICK`. These were both associated with initial condition `IC_TYPE = 5`.

Listing A.4 Density Profile Initial Condition

```
     ELSE IF (IC_TYPE.EQ.5) THEN
        DO J=0,NY
         DO K=0,NZM
           DO I=0,NXM
! Mixed layer of thickness TH_BC_YMAX_C3
! of density TH_BC_YMAX_C2
! overlaying stratified region with drhodz = TH_BC_YMIN_C2
! with a density jump of TH_BC_YMIN_C3
                IF (GYF(J) .GT. (GYF(NY) - TH_BC_YMAX_C3(N))) THEN
                    TH(I,K,J,N)=TH_BC_YMAX_C2(N)
                ELSE
                    TH(I,K,J,N)=TH_BC_YMIN_C2(N)*(GYF(J)-GYF(NY)
     &                   + TH_BC_YMAX_C3(N) ) + TH_BC_YMAX_C2(N)
     &                   + TH_BC_YMIN_C3(N)
                END IF
           END DO
         END DO
        END DO
```

Finally, some bugs were solved relating to how NetCDF files were saved for the channel case. In future work with this code base, it is strong recommended that the developers be contacted for the most recent version and these (few) changes by made to extend this work.

Running `make` should create and executable called `diablo`. Thus controlling simulation is done by creating the three files `input.dat`, `input_chan.dat`, and `grid_def` and compiling the executable. These steps are all automated in the script `model_run.py`. This script creates these control files, generates a vertical grid, compiles the executable, and submits the simulation to the batch system. Each run is identified by an unique positive integer, called a `run_id`, and the results are store in a directory with that name. The particular parameters used are stored in the Python pickled file `parameters.pkl`. The table A.1 lists the parameters that can be changed in the model.

A.2.3 Output

A snapshot of the U, W, ρ, and P fields are saved every so many timesteps, (given by `SaveInterval`, into a NetCDF file called `vis.nc`. Python code (e.g. listing A.5) or any other NetCDF library may be used to read this data file.

Table A.1: List of all parameters for model. Here are all the parameters that have been setup to be easily changed between numeric simulations.

Parameter in code	Symbol in thesis	Value or range	Description
PX0	dp/dx_0	-1.0 to -6.0	pressure gradient
H	H	1.0, 2.0	thickness of mixed layer
delta	δ	0.1	thickness of frictional layer
rho_mixed	ρ_T	0.50, 1.0	density of mixed layer
delta_rho	$\delta\rho$	0.50, 1.0	density jump at base of mixed layer
DRHODZ	$\Gamma = d\rho/dz$	-1.0	density gradient
RITAU	g/ρ_0	1000	acceleration due to gravity
PR	Pr	1.0	Prandtl number
NU	ν	0.0001	viscosity
KICK	ϵ	0.001	size of initial velocity perturbation
NX	n_x	256	number of horizontal grid points
NY	n_z	256	number of vertical grid points
NZ	n_y	1	number of spanwise grid points
LX	L_x	3.14	width of domain
LY	L_z	40	height of domain
LZ	L_y	3.14	span of domain
CS	C_S	1.00	stretched grid parameter
NTimeSteps	n_t	50000	total number of timesteps
DeltaT	δt	0.0004	time step
VarDT		False	variable time step flag
SaveInterval		250	time steps to dump state variables
FilterInterval		1	time steps to filter variables

Listing A.5 Example of retrieving numerical simulation output data from a NetCDF file. Notice that Diablo calls the vertical direction y but we call it z to be consistent with the lab coordinate system.

```
import netCDF4
# Open NetCDF file
vis = netCDF4.Dataset('vis.nc')

# Load data - [t-index slice, 0, z-index slice, x-index slice]
U = vis.variables['U'][:,0,:,:]
W = vis.variables['V'][:,0,:,:]
rho = vis.variables['TH'][:,0,:,:,:]

# Load grid
x = vis.variables['x'][:]
z = vis.variables['y'][:]
t = vis.variables['t'][:]

# Close NetCDF file
vis.close()
```

A.2.4 Simulation parameters

Table A.2: List of numerical simulations

Run Id	PX0	H	$\delta\rho$	ρ_T	ν	LX	NX	LZ	NZ	Δt
563	-1.0	1.0	0.5	0.5	1.0e-04	3.14	64	40.00	256	4.0e-04
564	-2.0	1.0	0.5	0.5	1.0e-04	3.14	64	40.00	256	4.0e-04
565	-3.0	1.0	0.5	0.5	1.0e-04	3.14	64	40.00	256	4.0e-04
566	-4.0	1.0	0.5	0.5	1.0e-04	3.14	64	40.00	256	4.0e-04
567	-5.0	1.0	0.5	0.5	1.0e-04	3.14	64	40.00	256	4.0e-04
568	-6.0	1.0	0.5	0.5	1.0e-04	3.14	64	40.00	256	4.0e-04
557	-1.0	1.0	0.5	0.5	1.0e-04	3.14	128	40.00	256	4.0e-04
558	-2.0	1.0	0.5	0.5	1.0e-04	3.14	128	40.00	256	4.0e-04
559	-3.0	1.0	0.5	0.5	1.0e-04	3.14	128	40.00	256	4.0e-04
514	-4.0	1.0	0.5	0.5	1.0e-04	3.14	128	40.00	256	4.0e-04
560	-4.0	1.0	0.5	0.5	1.0e-04	3.14	128	40.00	256	4.0e-04
561	-5.0	1.0	0.5	0.5	1.0e-04	3.14	128	40.00	256	4.0e-04
562	-6.0	1.0	0.5	0.5	1.0e-04	3.14	128	40.00	256	4.0e-04
550	-1.0	1.0	0.5	0.5	1.0e-04	3.14	256	40.00	256	4.0e-04
551	-2.0	1.0	0.5	0.5	1.0e-04	3.14	256	40.00	256	4.0e-04
552	-3.0	1.0	0.5	0.5	1.0e-04	3.14	256	40.00	256	4.0e-04
553	-4.0	1.0	0.5	0.5	1.0e-04	3.14	256	40.00	256	4.0e-04
554	-5.0	1.0	0.5	0.5	1.0e-04	3.14	256	40.00	256	4.0e-04
555	-6.0	1.0	0.5	0.5	1.0e-04	3.14	256	40.00	256	4.0e-04
593	-1.0	1.0	0.5	1.0	1.0e-04	3.14	256	40.00	256	4.0e-04
594	-2.0	1.0	0.5	1.0	1.0e-04	3.14	256	40.00	256	4.0e-04
595	-3.0	1.0	0.5	1.0	1.0e-04	3.14	256	40.00	256	4.0e-04
596	-4.0	1.0	0.5	1.0	1.0e-04	3.14	256	40.00	256	4.0e-04
597	-5.0	1.0	0.5	1.0	1.0e-04	3.14	256	40.00	256	4.0e-04
598	-6.0	1.0	0.5	1.0	1.0e-04	3.14	256	40.00	256	4.0e-04
544	-1.0	1.0	1.0	0.5	1.0e-04	3.14	256	40.00	256	4.0e-04
545	-2.0	1.0	1.0	0.5	1.0e-04	3.14	256	40.00	256	4.0e-04
546	-3.0	1.0	1.0	0.5	1.0e-04	3.14	256	40.00	256	4.0e-04
547	-4.0	1.0	1.0	0.5	1.0e-04	3.14	256	40.00	256	4.0e-04
548	-5.0	1.0	1.0	0.5	1.0e-04	3.14	256	40.00	256	4.0e-04
549	-6.0	1.0	1.0	0.5	1.0e-04	3.14	256	40.00	256	4.0e-04
520	-1.0	2.0	0.5	0.5	1.0e-04	3.14	256	40.00	256	4.0e-04
521	-2.0	2.0	0.5	0.5	1.0e-04	3.14	256	40.00	256	4.0e-04
522	-3.0	2.0	0.5	0.5	1.0e-04	3.14	256	40.00	256	4.0e-04
523	-4.0	2.0	0.5	0.5	1.0e-04	3.14	256	40.00	256	4.0e-04
524	-5.0	2.0	0.5	0.5	1.0e-04	3.14	256	40.00	256	4.0e-04
525	-6.0	2.0	0.5	0.5	1.0e-04	3.14	256	40.00	256	4.0e-04
526	-1.0	2.0	1.0	1.0	1.0e-04	3.14	256	40.00	256	4.0e-04
527	-2.0	2.0	1.0	1.0	1.0e-04	3.14	256	40.00	256	4.0e-04
528	-3.0	2.0	1.0	1.0	1.0e-04	3.14	256	40.00	256	4.0e-04

Table A.2: List of numerical simulations (continued)

Run Id	PX0	H	$\delta\rho$	ρ_T	ν	LX	NX	LZ	NZ	Δt
517	-4.0	2.0	1.0	1.0	1.0e-04	3.14	256	40.00	256	4.0e-04
529	-4.0	2.0	1.0	1.0	1.0e-04	3.14	256	40.00	256	4.0e-04
530	-5.0	2.0	1.0	1.0	1.0e-04	3.14	256	40.00	256	4.0e-04
531	-6.0	2.0	1.0	1.0	1.0e-04	3.14	256	40.00	256	4.0e-04
538	-1.0	1.0	0.5	0.5	1.0e-04	3.14	512	40.00	512	2.0e-04
539	-2.0	1.0	0.5	0.5	1.0e-04	3.14	512	40.00	512	2.0e-04
540	-3.0	1.0	0.5	0.5	1.0e-04	3.14	512	40.00	512	2.0e-04
541	-4.0	1.0	0.5	0.5	1.0e-04	3.14	512	40.00	512	2.0e-04
542	-5.0	1.0	0.5	0.5	1.0e-04	3.14	512	40.00	512	2.0e-04
543	-6.0	1.0	0.5	0.5	1.0e-04	3.14	512	40.00	512	2.0e-04
569	-1.0	1.0	0.5	0.5	1.0e-04	6.28	256	40.00	256	4.0e-04
570	-2.0	1.0	0.5	0.5	1.0e-04	6.28	256	40.00	256	4.0e-04
571	-3.0	1.0	0.5	0.5	1.0e-04	6.28	256	40.00	256	4.0e-04
572	-4.0	1.0	0.5	0.5	1.0e-04	6.28	256	40.00	256	4.0e-04
573	-5.0	1.0	0.5	0.5	1.0e-04	6.28	256	40.00	256	4.0e-04
574	-6.0	1.0	0.5	0.5	1.0e-04	6.28	256	40.00	256	4.0e-04
575	-1.0	2.0	0.5	0.5	1.0e-04	6.28	256	40.00	256	4.0e-04
576	-2.0	2.0	0.5	0.5	1.0e-04	6.28	256	40.00	256	4.0e-04
577	-3.0	2.0	0.5	0.5	1.0e-04	6.28	256	40.00	256	4.0e-04
578	-4.0	2.0	0.5	0.5	1.0e-04	6.28	256	40.00	256	4.0e-04
579	-5.0	2.0	0.5	0.5	1.0e-04	6.28	256	40.00	256	4.0e-04
580	-6.0	2.0	0.5	0.5	1.0e-04	6.28	256	40.00	256	4.0e-04
511	-4.0	1.0	0.5	0.5	1.0e-04	6.28	512	40.00	256	4.0e-04
581	-1.0	1.0	0.5	0.5	1.0e-04	12.56	256	40.00	256	4.0e-04
582	-2.0	1.0	0.5	0.5	1.0e-04	12.56	256	40.00	256	4.0e-04
583	-3.0	1.0	0.5	0.5	1.0e-04	12.56	256	40.00	256	4.0e-04
584	-4.0	1.0	0.5	0.5	1.0e-04	12.56	256	40.00	256	4.0e-04
585	-5.0	1.0	0.5	0.5	1.0e-04	12.56	256	40.00	256	4.0e-04
586	-6.0	1.0	0.5	0.5	1.0e-04	12.56	256	40.00	256	4.0e-04
587	-1.0	2.0	0.5	0.5	1.0e-04	12.56	256	40.00	256	4.0e-04
588	-2.0	2.0	0.5	0.5	1.0e-04	12.56	256	40.00	256	4.0e-04
589	-3.0	2.0	0.5	0.5	1.0e-04	12.56	256	40.00	256	4.0e-04
590	-4.0	2.0	0.5	0.5	1.0e-04	12.56	256	40.00	256	4.0e-04
591	-5.0	2.0	0.5	0.5	1.0e-04	12.56	256	40.00	256	4.0e-04
592	-6.0	2.0	0.5	0.5	1.0e-04	12.56	256	40.00	256	4.0e-04
513	-4.0	1.0	0.5	0.5	1.0e-04	12.56	1024	40.00	256	4.0e-04
556	-4.0	2.0	0.5	0.5	1.0e-04	12.56	1024	40.00	256	4.0e-04
516	-4.0	1.0	0.5	0.5	1.0e-03	3.14	256	40.00	256	4.0e-04
515	-4.0	1.0	0.5	0.5	1.0e-02	3.14	256	40.00	256	4.0e-04